

UC Berkeley

UC Berkeley Electronic Theses and Dissertations

Title

Printed Zinc Batteries for Wireless Electronic Networks

Permalink

<https://escholarship.org/uc/item/5836p64t>

Author

Kumar, Rajan

Publication Date

2019

Peer reviewed|Thesis/dissertation

Printed Zinc Batteries for Wireless Electronic Networks

By

Rajan Kumar

A dissertation submitted in partial satisfaction of the

Requirements for the degree of

Doctor of Philosophy

in

Engineering – Materials Science and Engineering

in the

Graduate Division

of the

University of California, Berkeley

Committee in charge:

Professor Oscar Dubón, Co-Chair
Professor Vivek Subramanian, Co-Chair
Professor Ana Claudia Arias
Associate Professor Kristin Persson

Fall 2019

Copyright © 2019, by the author(s).

All rights reserved.

Permission to make digital or hard copies of all or part of this work for personal or classroom use is granted without fee provided that copies are not made or distributed for profit or commercial advantage and that copies bear this notice and full citation on the first page. To copy otherwise, to republish, to post on servers or to redistribute to lists, requires prior specific permission.

Abstract

Printed Zinc Batteries for Wireless Electronic Networks

by

Rajan Kumar

Doctor of Philosophy in Materials Science and Engineering

University of California, Berkeley

Professor Oscar Dubón, Co-Chair
Professor Vivek Subramanian, Co-Chair

The prevalence of wireless device networks for the Internet of Things (IoT) depends on the development of integrated energy storage. Today, IoT devices are powered either through a wired connection, which greatly inhibits their broad distribution, or by coin cell batteries, which constrain device size, weight, cost, and form factor. New approaches to energy storage design such as printing-based fabrication techniques are well suited to simplify device integration. Using additive, high-throughput processing methods, batteries can be printed to accommodate millimeter-scale nodes and seamlessly integrated into semiconductor packaging flows. While previous studies have focused on developing printable electrode, separator, and current collector inks, none have emphasized scaling printed battery size and power to accommodate IoT system requirements. This dissertation addresses several challenges associated with designing millimeter-scale energy storage for IoT technologies, utilizing printing techniques to create batteries that could enable scalable wireless electronic networks. A comprehensive approach is taken to achieve battery scaling and integration, highlighting the interconnected impact of processing, structure, properties, and performance of printed battery materials.

Printed Zn-based batteries are explored given their compatibility with IoT performance requirements, offering high energy densities, high discharge rate capabilities, and steady discharge potentials. Zn battery chemistries are also inherently air-stable, require modest packaging, and use low-cost, earth-abundant materials, making them excellent candidates for additive integration with wireless electronics. Printed Zn-Ag₂O and Zn-air batteries are presented in this work, implementing vertical cell architectures to minimize battery footprints and thick electrode films to maximize cell capacity. In both chemistries, printed battery performance is evaluated as a function of materials processing and design, with a focus on minimizing battery sizes and processing temperatures. By co-optimizing each cell component, new performance benchmarks are established for printed batteries, achieving areal capacities above 10 mAh cm⁻² and power densities well above 10 mW cm⁻² with millimeter-scale areas and processing temperatures below 200 °C.

Additionally, this dissertation utilizes *operando* characterization techniques to further study the impact of materials processing and design on printed battery performance. *Operando* techniques offer an emerging set of tools to investigate transient, non-equilibrium materials such as

electrochemical interfaces. In this work, *operando* methods enable the direct observation of electrochemical reactions in printed Zn batteries, which guides battery development to improve performance and mitigate degradation. First, oxygen reduction is measured in Zn-air batteries to determine the influence of electrode composition and processing temperatures on cathodic efficiency. Second, hydrogen evolution and oxide formation are examined in Zn-air batteries to identify design and operation parameters that affect anodic corrosion. Overall, these techniques aim to complement ex-situ analysis of printed batteries and elucidate relationships between physical or chemical changes and improvements in battery performance.

Finally, this work discusses system level integration strategies for printed Zn batteries and IoT devices. Proof of concept packaging and interconnect designs are demonstrated using printing techniques for millimeter-scale and commercially available sensor nodes. Printed Zn-Ag₂O batteries are also simulated under IoT operation modes to determine performance benchmarks in an integrated system with energy harvesting. Moreover, printed Zn-Ag₂O battery arrays are explored to support high voltage applications.

Acknowledgments

After my first six months of graduate school, I thought I did not belong in a PhD program. Like many other graduate students, I struggled with independent research, feeling that problems in the lab were my own personal failures. Today, I want to recognize all of the people that made me realize I belong. I would not have completed this dissertation without all of your support. Thank you for making my endeavors in research, teaching, and mentorship so much more rewarding.

I am honored and privileged to have formed so many great relationships during my PhD. First, I would like to acknowledge my two co-advisors, Professor Oscar Dubón and Professor Vivek Subramanian. Oscar – you have been an amazing role model and mentor for me. Thank you for your constant encouragement and your genuine interest in my personal and professional success. Vivek – you have helped me become so much more comfortable being a researcher. Thank you for always challenging me to think about problems systematically while giving me the freedom to explore my interests. You have both helped me have a truly fulfilling PhD experience.

I would also like to acknowledge Professor Kristin Persson and Professor Ana Arias. Thank you for being a part of my qualifying exam and dissertation committees. Your insight and support is truly appreciated.

To my fellow printed electronics group members – I could not have gotten through the daily grind of grad school without you. From training me in the lab and giving me feedback on my presentations to playing football and enjoying lunch together, you made me feel welcome and respected. Sarah, Swisher, Jake Sadie, Jeremy Smith, Seungjun Chung, Rumi Karim, Gerd Grau, and Andre Zeumault – thank you for demonstrating what great research looks like and being so supportive during my early years in the group. Lance O’Hari P. Go, Yasuhiro Kobayashi, Thomas Rembert, Xiaoer Hu, and Steve Volkman – it was wonderful getting to work with each of you; thank you for all of the great conversations in the lab. Kevin Johnson, Nick Williams, Joubel Boco, Cher Yeoh, and Tony Wang – thank you for helping me get my battery research off the ground. Your enthusiasm and hard work were much appreciated and I could not have accomplished nearly as much without all of your help. And to Will Scheideler, Nishita Deka, Carlos Biaou, Matt McPhail, Jake Sporrer, and Alvin Li – thank you for all of the comedic relief. I will fondly remember the dinners, go-karts, wine trips, artisanal batteries, and wedding hashtags that never made it very fondly.

To my fellow Dubon group members – thank you for welcoming and supporting me, especially as I prepared for my qualifying exam. Jose Fonseca, Chris Francis, Thang Pham, Maribel Jaquez, Edy Cardona, and Petra Specht – I greatly appreciated your thoughtful perspectives on my work and I’m glad I had the chance to learn more about electronic materials from each of you.

I also want to acknowledge all of my research collaborators at UC Berkeley, SLAC, and Argonne who helped me take an interdisciplinary approach to my research that I would not have had otherwise. I am very thankful to have worked with Professor Brian McCloskey and his group, especially Jessica Nichols, Elyse Kedzie, Colin Burke, Sara Renfrew, Joe Papp, and Sarah Berlinger. Jessica and Elyse – thank you for all of your countless hours helping me run some very cool experiments. I had a lot of fun testing batteries with each of you. I’m also very appreciative

to have worked with Dr. Michael Toney through my DOE SCGSR Fellowship. Thank you for giving me the opportunity to come to SSRL and welcoming me into your group. To Donata Passarello, Kipil Lim, Natalie Geise, Chuntian Cao, Robert Kasse, Hans-Georg Steinruck, and Chris Takacs – it was wonderful getting to work with all of you. Thank you for all of your guidance on the beamline and help with my experiments. Additionally, thank you to Professor Kris Pister, Brad Wheeler, Fil Maksimovic, Joey Greenspun, Travis Massey, Osama Khan, Jonathan Ting, Donggeon Han, Dr. Venkat Srinivasan, and Pallab Barai for all of your helpful contributions.

Finally, I would not have survived my PhD without the love and support of my family. To my parents and my sister – I have each of you to thank for indoctrinating me in our family ways. I owe my love for teaching, mentoring, and helping others to each of you. Thank you for always setting the best example of how to be a good person and continuously supporting my ambition.

And to my wife, Christina – thank you for being the Bryant to my Rizzo. Throughout grad school, you have always been in my corner and given me nothing but encouragement. Even when I'm a glass case of emotions (I mean tired, stressed, or frustrated), you drop everything to help me push through. Thank you for always putting our relationship first. I couldn't ask for a better teammate.

Table of Contents

Chapter 1: Introduction	1
1.1 Powering the Internet of Things	1
1.2 Energy Storage	4
1.2.1 Battery Fundamentals	5
1.2.2 Battery Classifications and Metrics	6
1.2.3 Battery Chemistries	7
1.2.4 Battery Packaging	9
1.3 Printing as a Fabrication Technology for Batteries	11
1.4 Developing Materials for Printed Batteries	14
1.5 Remaining Challenges for Printed Batteries	16
1.6 Dissertation Organization.....	17
1.7 References	19
Chapter 2: Scaling Printed Zn-Ag₂O Batteries for Integrated Electronics	22
2.1 Introduction	22
2.2 Printed Battery Architecture and Processing.....	23
2.2.1 Current Collectors	24
2.2.2 Sol-Gel Separator and Polymer Encapsulation.....	25
2.2.3 Zinc and Silver-Oxide Electrodes	26
2.3 Battery Characterization and Stability	29
2.4 Battery Performance	33
2.5 Summary	36
2.6 References	38
2.7 Appendix	40
Chapter 3: Printed Cathodes for Aqueous Metal-Air Batteries	41
3.1 Introduction	41
3.2 Air Cathode Design and Printed Battery Architecture	42
3.3 Cathode Materials Characterization.....	45
3.4 <i>Operando</i> Characterization of Printed Cathodes.....	49
3.5 Zn-Air Battery Performance.....	55
3.6 Summary	57
3.7 References	58
Chapter 4: Characterizing Zn Corrosion via <i>Operando</i> Techniques	60
4.1 Introduction	60
4.2 Zn Corrosion in Alkaline Environments	61
4.3 Quantifying Corrosion Rates via DEMS and Pressure Decay Measurements	64
4.4 <i>Operando</i> X-ray Diffraction Analysis of Zn Corrosion	71
4.5 Summary	76
4.6 References	77

Chapter 5: Printed Battery Packaging and Integration for IoT Systems	78
5.1 Introduction	78
5.2 Printed Packaging and Interconnects	78
5.2.1 3D Printed Packaging and Stencil Printed Interconnects.....	79
5.2.2 Inkjet Printed Packaging and Interconnects	81
5.3 Integrating Printed Batteries with Energy Harvesting for IoT Device Operation.....	83
5.4 Screen Printed Zn-Ag ₂ O Arrays	87
5.5 Summary	92
5.6 References	93
Chapter 6: Conclusions and Future Work.....	94
6.1 Summary of Contributions	94
6.2 Recommendations for Future Work	95

Chapter 1: Introduction

1.1 Powering the Internet of Things

Over the next decade, the Internet of Things (IoT) promises to be one of the most disruptive technologies in our society. Through the use of sensors, actuators and antennas to collect and transmit data, IoT systems have the potential to revolutionize how we make decisions to achieve common goals.^[1] Several critical industries including healthcare monitoring, environmental sensing, and energy management will greatly benefit from real-time feedback from ubiquitous electronics, accelerating decision-making efficiency and adaptability. As a result, IoT systems are gaining significant attention, with the overall IoT industry expected to generate a revenue of \$4.3 trillion by 2024, or nearly ten times the global semiconductor industry's revenue from 2018.^[2]

Significant advances have been made to design, manufacture, and connect IoT devices to make wireless sensor networks (WSNs) a reality. Most importantly, research efforts have focused on creating low-power consumption nodes and integrating sensing, computing, and communication functionalities into a single system, as shown in Figure 1.1.^[3,4] These requirements aim to reduce device costs and miniaturize device footprints in order to realize large-scale, densely deployed arrays of IoT devices. For example, the Smart Dust project has explored size and power consumption limits for integrated, autonomous sensor nodes utilizing system on chip architectures.^[5-7]

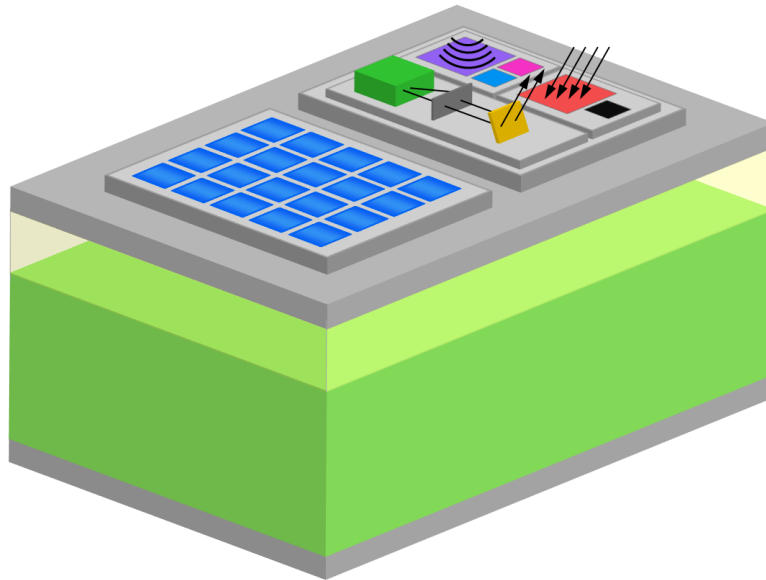


Figure 1.1: Conceptual illustration of a single chip node for a wireless sensor network with integrated sensing, computing, communication, and power

Although device miniaturization and power reduction intend to enable several emerging IoT applications, *the prevalence of WSNs depends on the development of integrated energy storage*. Today, IoT devices are powered either through a wired connection, which greatly inhibits their broad distribution, or by coin cell batteries, which constrain several device parameters including size, weight, cost, and form factor. Thus, new approaches to energy storage design and

process integration must be devised in order to keep up with device scaling and create integrated and autonomous systems.

Ideally, energy storage should be compatible with emerging microelectronics processing techniques and silicon integration strategies such as wafer-level and chip-scale packaging. This demands energy storage architectures with thin overall form-factors ($< 1\text{mm}$) and small areas ($< 1\text{cm}^2$). Furthermore, integrated energy storage must accommodate the capacity, current density, and power density requirements of the supported device. As shown in Figure 1.2, typical low-power IoT device nodes have peak current draws of $1\text{-}10\text{ mA cm}^{-2}$ and peak power densities of $10\text{-}100\text{ mW cm}^{-2}$ while integrated storage must sustain high energy densities in order to provide suitable capacity at form factors approaching 1 mm^2 .^[8]

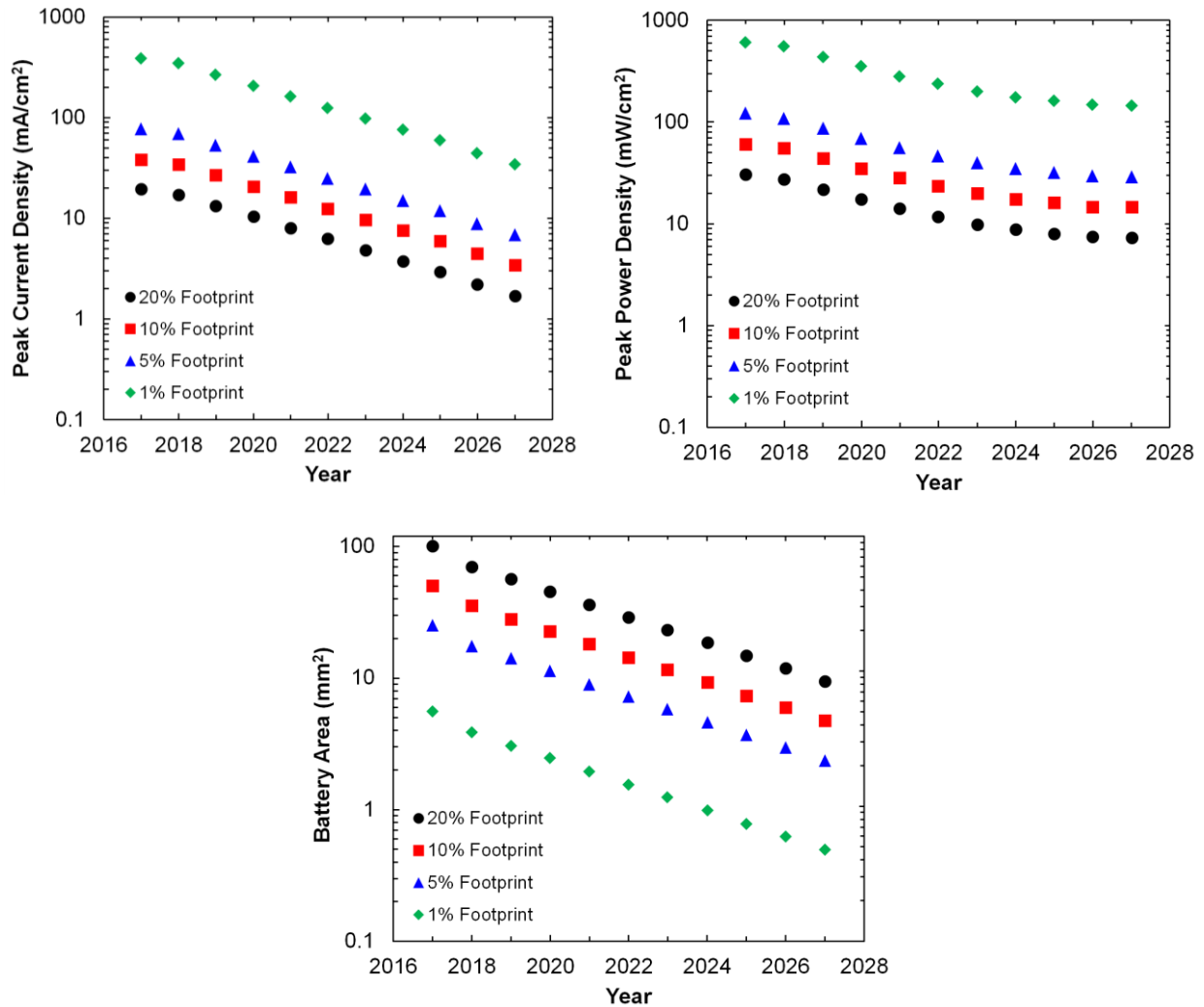


Figure 1.2: Current, power, and battery size requirements for low-power devices for the IoT driver. Data collected from the System Integration chapter in the ITRS 2.0 2015 Edition.^[8] Percentage of footprint corresponds to amount of module space dedicated for a battery assuming a planar architecture layout.

Given the limitations of current energy storage technologies for IoT devices, recent studies have outlined critical challenges that must be overcome to power ubiquitous electronics.^[9–12] For instance, IoT operation modes are quite different from consumer electronics such as laptops or cell phones. Instead of daily charge and discharge cycles, these devices require short pulses of power on the MHz – Hz time scale but have low duty cycles and spend most of the time in a low-power off state. These multiple operation states and power requirements for WSNs are further described in Table 1.1. Additionally, a representative power consumption profile for an individual node is shown in Figure 1.3, highlighting the high-power pulses that need to be accommodated in these systems.^[10] As a result, WSNs have included both energy storage to accommodate high-power pulses and energy harvesting technologies to support low-power off states. While energy storage relies on capturing energy for use at a later time, energy harvesting relies on collecting energy from external sources for immediate use. Various forms of energy can be harvested for use, including mechanical (eg. piezoelectrics for vibrational energy), photonic (eg. photovoltaics for solar energy), and thermal energy (eg. thermoelectrics for heat transfer).^[9,13–16] For most future IoT applications, a combination of energy storage and energy harvesting will likely be required, but energy storage is paramount to sustaining device functionality over long periods of time. Thus, energy storage for IoT systems will be the focus of this dissertation.

Table 1.1: Modes of operation for wireless sensor nodes and their associated power consumption

Function	Duration (s)	Power (mW)	Description
Sleep	$10^{-1} - 10^4$	$10^{-3} - 10^{-1}$	Minimal power required for background functions such as internal clock
Polling	$10^{-5} - 1$	$10^{-3} - 100$	Power needed for data collection, including sensor, actuator, and computing functions
Transmitting	$10^{-6} - 1$	$1 - 100$	Power needed to send a data packet to another node or control station. Power scales with transmission distance and frequency
Receiving	$10^{-3} - 10$	$10^{-1} - 1$	Power needed to listen for an incoming data packet and confirm data acquisition

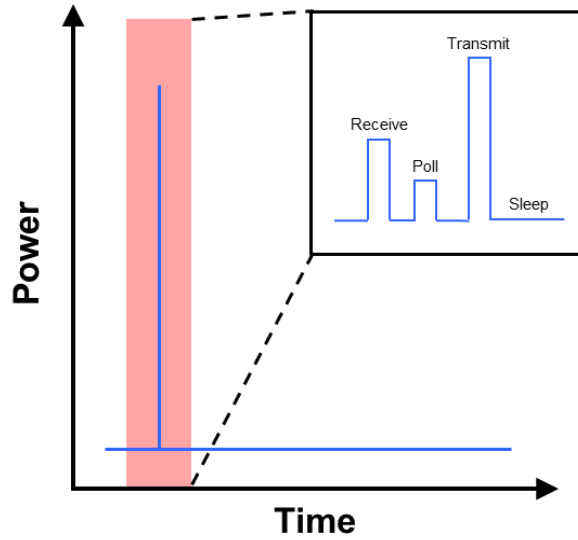


Figure 1.3: Example of a power consumption profile for a wireless sensor node

1.2 Energy Storage

Energy can be stored in a variety of forms, including chemical storage (gasoline, methanol, hydrogen), electrical storage (capacitors), electrochemical storage (batteries, fuel cells, electrochemical capacitors), mechanical storage (flywheels, pumped hydro, compressed air), and thermal storage (molten salts).^[17] Each of these systems store energy at different scales and have tradeoffs between power and energy, as shown in the Ragone plot in Figure 1.4. Among these energy storage technologies, batteries have been predominantly used with IoT systems given their high gravimetric and volumetric energy density, small form factor, and large-scale market penetration within the consumer electronics industry.

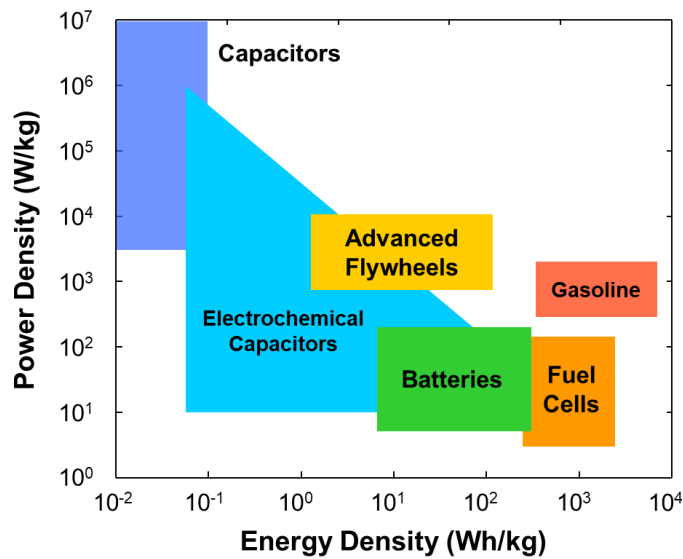


Figure 1.4: Comparison of the power and energy density characteristics for various forms of energy storage

1.2.1 Battery Fundamentals

Today, batteries are found in nearly all electronic devices and are relied upon heavily for portable electronics such as laptops and cell phones. A battery converts chemical energy to electrical energy through electrochemical reactions known as oxidation and reduction. This involves the transfer of both electrons through an electrical circuit and ions across an ionically conductive media. A cell is the individual unit of a battery, which can be connected in series or parallel with other cells to increase the output voltage or capacity of the battery.^[18] The cell consists of five main components:

- 1) Anode – the negative electrode or reducing agent – gives up electrons to the external circuit and is oxidized during the electrochemical reaction
- 2) Cathode – the positive electrode or oxidizing agent – accepts electrons from the external circuit and is reduced during the electrochemical reaction
- 3) Electrolyte – the ionic conductor – provides the medium for ionic charge transfer between the anode and cathode – can be a liquid or solid
- 4) Separator – the physical barrier – maintains electrical separation between the anode and cathode – contains liquid electrolytes typically in a porous structure, while solid electrolytes typically do not require an additional separator
- 5) Current Collectors – the electronic conductors – ensure electron insertion and removal from the anode and cathode

In any cell, two reactions occur at the electrode-electrolyte interfaces: oxidation and reduction. The overall reaction in the cell can be represented as combination of these two reactions:



where a molecules of A take up n electrons to form c molecules of C . The change in the standard free energy ΔG° is expressed as:

$$\Delta G^\circ = -nFE^\circ \quad (1.4)$$

where F is Faraday's constant (96,485 C/mol) and E° is the equilibrium potential, which is also referred to as the open-circuit potential. As the overall reaction in Equation 1.3 proceeds, the potential E of a cell is given by the Nernst equation:

$$E = E^\circ - \frac{RT}{nF} \ln \frac{a_C^c a_D^d}{a_A^a a_B^b} \quad (1.5)$$

where a_i is the activity of each species, R is the gas constant, and T is the temperature. Thus, the cell potential can be determined based on the two half-cell reactions that occur at each electrode. Direct measurement of an absolute cell potential is impossible, so half-cell potentials, also referred to as standard potentials, are always referenced to a benchmark. By convention, the standard potential of the hydrogen evolution reaction (H_2/H^+) is set as zero and all other standard potentials are referenced to this reaction.

Reactions at the electrode-electrolyte interfaces are non-equilibrium in nature, however, so cell potential depends on several factors intrinsic to the cell. Each of these factors contributes to cell resistance, referred to as an overpotential, which lowers the overall potential of the cell compared to the thermodynamically calculated potential.^[19] Types of cell resistance include:

- 1) Surface overpotential – driving force for electrochemical reactions (Butler-Volmer eq.)
- 2) Ohmic overpotential – driving force for the flow of charge carriers – (Ohm’s law)
- 3) Concentration overpotential – driving force for the diffusion of species – (Fick’s laws)

Thus, the potential difference across a cell will depend on both the open-circuit potential and the kinetic, charge transfer, and mass transport limitations. These potential drops are all interrelated and are influenced by operational parameters such as applied current density and state of charge as well as physical parameters such as temperature and concentration. This makes isolating the causes of potential losses difficult, so coupled phenomena must be considered when analyzing electrochemical systems.

1.2.2 Battery Classifications and Metrics

Batteries can be classified as either primary (nonrechargeable), secondary (rechargeable), or reserve (nonrechargeable, one or more components stored separately before activation). Upon discharge, the negative electrode is oxidized and loses electrons while the positive electrode is reduced and gains electrons. Upon charge, the current flow is reversed and oxidation takes place at the positive electrode and reduction at the negative electrode.

Several metrics are used to identify battery standards and classify performance, but we will focus on a few particular metrics in this dissertation. First, the capacity is the amount of electrical energy that is stored in the active components, which are the electrodes for a battery. The theoretical capacity of an electrode is based on the half-cell reactions at each electrode, the number of electrons exchanged in these reactions, and the density and atomic mass of the electrodes, with an example shown for Zn in Equations 1.6–1.7. Capacity is often measured experimentally by multiplying the discharge current by the discharge time (mAh) and is compared to the theoretical capacity. It can also be quantified as a specific capacity (mAh g⁻¹) or an areal capacity (mAh cm⁻²). Typically, the maximum capacity of a battery is reported for a set of operating conditions but may change depending on the operating temperature, discharge rate, or other experimental factors. While volumetric capacity (mAh cm⁻³) is a better metric to determine the intrinsic performance of the battery, areal capacity is often used in the printed battery community and is discussed further in Section 1.4-1.5.

$$1 \text{ gram Zn} \times \frac{1 \text{ mol}}{65.38 \text{ g}} \times \frac{6.022 \times 10^{23} \text{ atoms}}{\text{mol}} \times \frac{2 \text{ e}^-}{\text{atom}} \times \frac{1.6 \times 10^{-19} \text{ C}}{\text{e}^-} = 2947 \text{ C} \quad (1.6)$$

$$2947 \text{ C} \times \frac{1 \text{ mAh}}{3.6 \text{ C}} = 819 \text{ mAh} \quad (1.7)$$

Second, the current density is the rate at which charge is transferred to or from the electrodes. Current density is typically an operating condition set based on the supported device requirements and is often measured in mA cm⁻². This metric is typically more useful for IoT device

integration compared to C rates, which are normalized to battery capacity, since the current requirements for IoT systems are irregular, as mentioned in Section 1.1.

Finally, the power density is the rate of energy consumption per unit volume or weight. The power density is determined based on the cell potential and the applied current density. A battery's maximum power density can be obtained by performing a polarization experiment, where cell potential is measured as a function of the applied current density. Based on the different factors that affect cell overpotential (as discussed in Section 1.2.1) and their responses to the applied current, a battery will typically exhibit a profile similar to Figure 1.5.

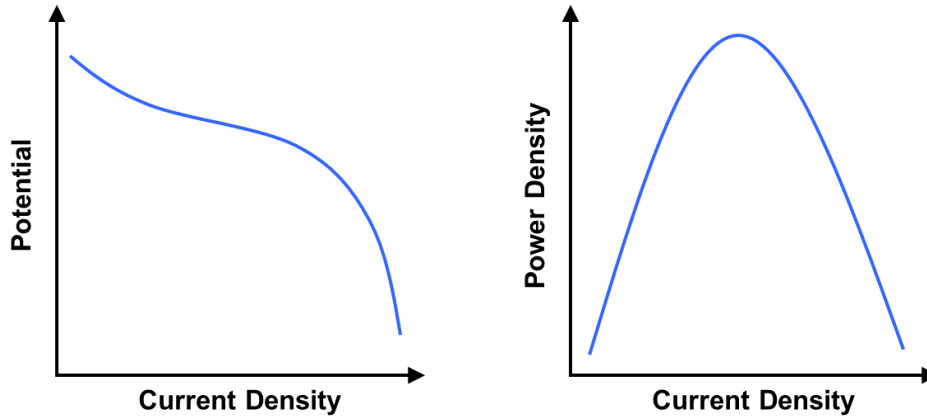


Figure 1.5: Example of a polarization curve for a battery

1.2.3 Battery Chemistries

Anode and cathode materials can be combined in a nearly limitless number of combinations to create a battery, but several practical constraints limit the number of viable electrochemical couples used in batteries today. These factors include energy density (both volumetric and gravimetric), cycle life, charge and discharge rates, temperature range, and cost of materials. Energy storage requirements are solely dependent on the device application, so benchmarks for each of these metrics will change depending on the device requirements. For example, grid scale storage will have different specifications for energy density and discharge rates compared to electric vehicle storage. As a result, several battery chemistries have been commercialized and a few of them are described here and summarized in Table 1.2.

Table 1.2: Characteristics and applications of primary and secondary batteries

Chemistry	Mode	Characteristics	Applications
Zn-MnO ₂	Primary	Good low temperature performance, high discharge rates, moderate costs, high shelf life	Portable and consumer electronics
Zn-Ag ₂ O	Primary	High specific capacity, flat discharge, good shelf life, higher cost	Hearing aids, watches, underwater and space applications

Zn-air	Primary	High energy density, poor shelf life dependent on environmental conditions	Hearing aids, medical devices, portable electronics
Lithium ion	Secondary	High voltage, high energy density, long cycle life	Portable and consumer electronics, electric vehicles
Lead-acid	Secondary	Low cost, moderate energy density, wide temperature range, high discharge rates	Automotive, golf carts, lawn mowers, tractors, trucks, emergency power, utilities, power tools
Nickel-metal hydride	Secondary	High specific capacity, high discharge rates, moderate cycle life	Consumer electronics, hybrid electric vehicles
Nickel-zinc	Secondary	High specific capacity, low cost, moderate cycle life	Scooters, bicycles, trolling motors

Primary batteries are commonly used in communication systems, medical devices, and large format cells for underwater and space applications. Many primary cells utilize Zn anodes due to their low cost, earth abundance, and ease of fabrication in non-inert environments. These chemistries include Zn-MnO₂, Zn-Ag₂O, and Zn-air cells and all typically utilize alkaline electrolytes such as KOH. Alkaline electrolytes are caustic and are often highly concentrated (20-50 wt%) in order to provide high ionic conductivity, so electrolyte-resistant plastics must be utilized during cell packaging to avoid cell corrosion or electrolyte leakage. Zn-MnO₂ is the most popular primary cell chemistry given their moderate cost of materials, suitable high-discharge rate performance, and long shelf life. Comparatively, Zn-Ag₂O and Zn-air batteries have higher materials costs but offer higher energy densities.

Secondary batteries are nearly ubiquitous today in portable electronics such as laptops and cell phones, but are also being utilized in larger format applications including electric vehicles and grid scale storage. Lead-acid batteries are one of the oldest secondary battery chemistries and are popular in automotive applications given their reliable performance over a wide temperature range. Nickel-based batteries such as Ni-metal hydride and Ni-Zn are utilized in high-power consumer electronics and were first implemented in hybrid electric vehicles and electric scooters and bicycles. But among secondary cell chemistries, lithium-ion batteries are the most popular given their high voltage, high energy density, and long cycle life. In commercial cells, carbon is typically used as the anode material and a lithium-metal-oxide alloy such as LiCoO₂ or LiMnO₂ is used as the cathode material. A Li containing organic electrolyte such as LiPF₆ in ethylene carbonate and dimethyl carbonate is commonly used to shuttle Li ions reversibly. Although widely used, lithium-ion batteries require careful attention to processing, packaging, and safety considerations. Lithium is highly reactive with water; so Li-ion batteries must be assembled in inert environments such as glove boxes or dry rooms and hermetically sealed to avoid air exposure. Packaging materials must also be compatible with the electrolyte chosen since most Li-ion electrolytes are flammable and highly reactive. Additionally, Li-ion battery operation must be closely monitored to avoid critical failure mechanisms such as Li plating and dendrite formation on the anode, gas generation and pressure buildup, or temperature spikes during overcharging or fast discharging.

1.2.4 Battery Packaging

In addition to cell chemistry, packaging also greatly influences a battery's utility. Battery safety and materials degradation are crucial factors that hinge on the use of suitable packaging strategies. Other parameters are also heavily dependent on battery packaging, such as lifetime, energy density, power density, and cost.^[20] Overall, packaging conforms the battery to the intended application, determining the sealing, form factor, temperature, and even state of charge of the battery pack.

Among the established cell chemistries discussed in Section 1.2.3, there are a few standard packaging formats. These include cylindrical, coin, prismatic, and pouch cells, as shown in Figure 1.6.^[21] Cylindrical cells are made of flat cells that are layered and rolled into a cylindrical can. These cells have a high packing density and offer high mechanical stability since the cylinder is able to withstand internal pressures without deformation. Cylindrical cells also offer low internal resistance and can deliver high currents, but require specialized insulator materials to separate active components and result in higher manufacturing costs. Coin cells, also called button cells, house the anode and cathode inside two cell cans that are crimped together around a gasket. These cells provide smaller form factors and lower manufacturing costs, but have lower packing density and require slow charging to avoid swelling, so most coin cells are used in primary configurations. Coin cells are also commonly used in research laboratories for proof of concept designs due to their simple assembly.

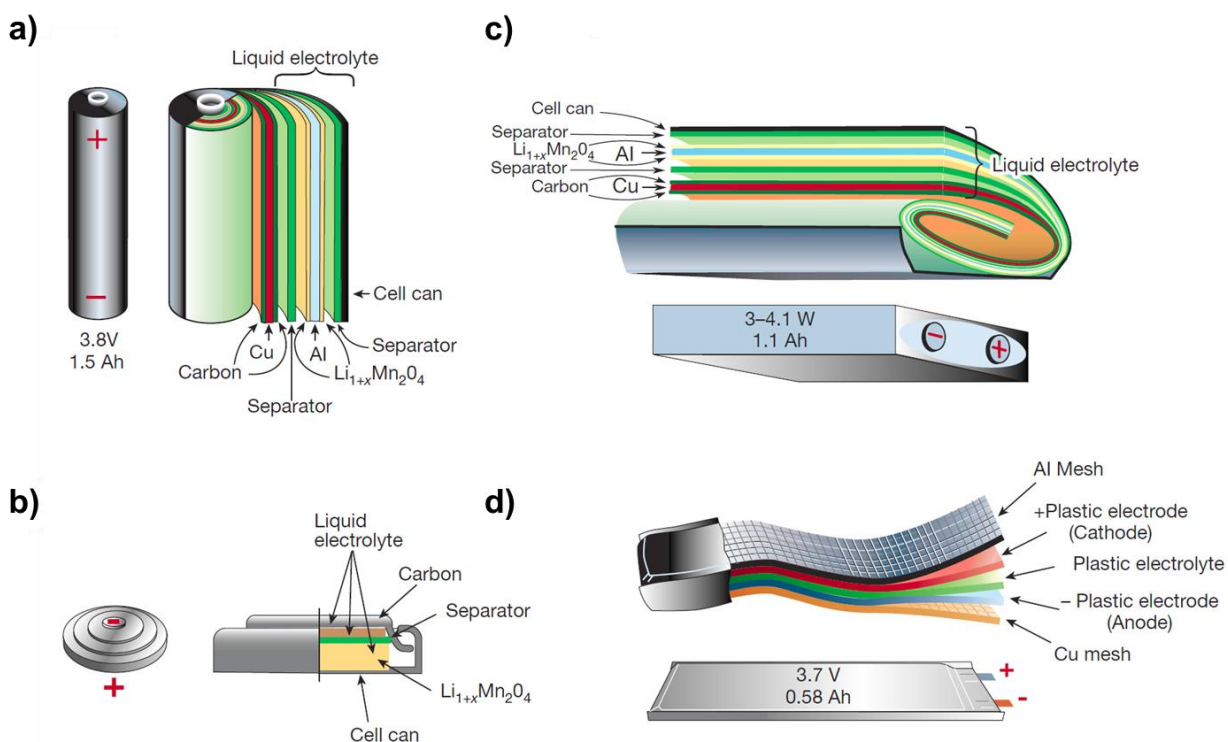


Figure 1.6: Schematic of the shape and components of various battery configurations including a) cylindrical b) coin c) prismatic and d) pouch cells.^[21] Formats are given for Li-ion batteries, but are similar for other battery chemistries.

Prismatic cells are layered and rolled in a similar method to cylindrical cells, but achieve thinner form factors needed for many consumer electronics applications. Prismatic cells have improved space utilization compared to coin cells and have greater design flexibility, but are also more expensive to manufacture and require extra space to accommodate swelling, which lowers the overall volumetric energy density of the battery. Finally, pouch cells offer the thinnest, most flexible form factor available for commercial cells based on the use of soldered foils as current collectors instead of rigid electrical feed-throughs. Pouch cells have high packing efficiency, although some space must be allocated for cell swelling. Housed in lightweight packaging made of Al and polymer films, pouch cells are commonly used in most portable electronic devices such as laptops and cell phones.

Aside from these widely used packaging formats, alternative battery packaging schemes are also being explored within the research community, as shown in Figure 1.7. One such format is the Swagelok type cell, where metal rods are used as current collectors and electrodes are sandwiched in between Swagelok compatible gaskets, spacers, and fittings.^[22] These cells are similar in nature to coin cells, but offer a significant advantage in that they can be easily disassembled after cell testing, making post-mortem analysis and component recycling possible. Another emerging format is the *operando* cell, which is often a commercial format such as a pouch or coin cell that has been modified to include an X-ray transparent window into the cell.^[23] The *operando* cell permits battery characterization during charging and discharging to capture information about the non-equilibrium processes that occur within the cell. *Operando* cells will be discussed in greater detail in Chapter 4.

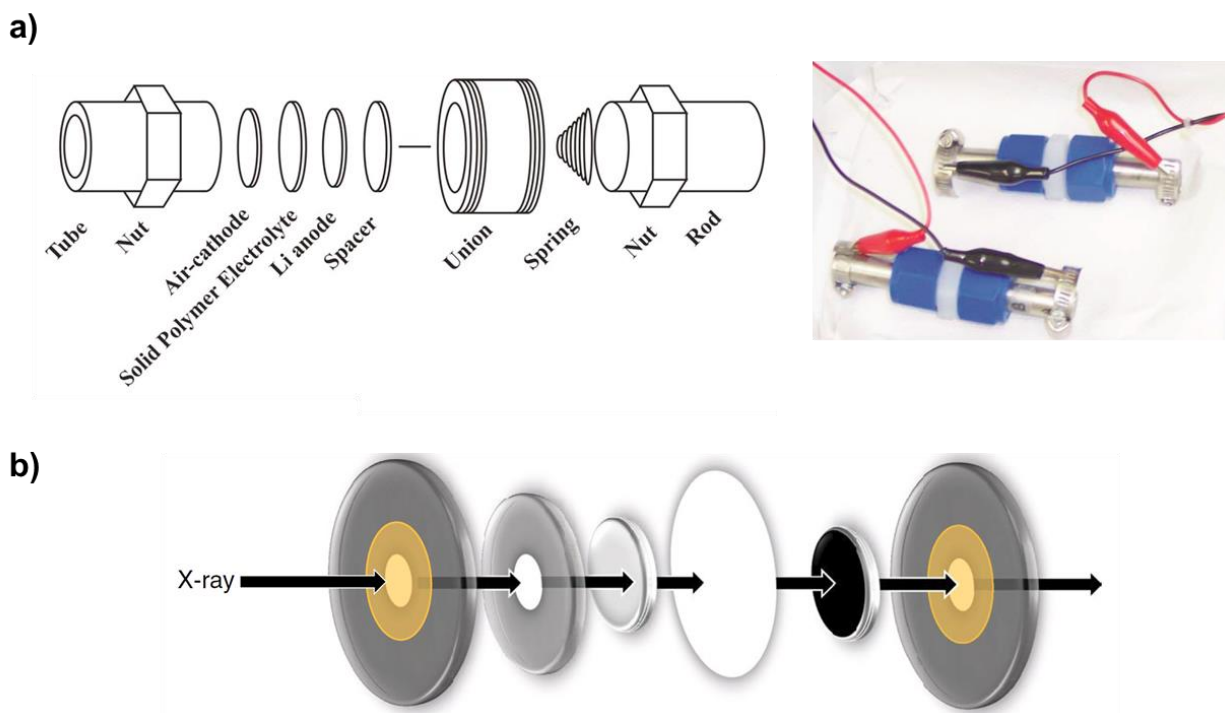


Figure 1.7: a) Schematic and picture of a Swagelok cell used for a Li-O₂ battery.^[22] b) General schematic of an *operando* cell design.^[24]

1.3 Printing as a Fabrication Technology for Batteries

Millimeter-scale single chip nodes are poised to enable several emerging IoT technologies, but several advances in system integration must be made in order to realize autonomous nodes for WSNs. Incorporating sensing, computation, communication, and energy storage demands careful consideration of process integration and assembly. Moving forward, none of the traditional battery packaging strategies discussed in Section 1.2.4 are compatible with a millimeter-scale single chip node, so alternative processing methods are needed to reduce integration complexity and minimize battery size, weight, and cost.

Among several emerging approaches, printing-based fabrication techniques are well-suited to simplify system integration and enable battery form factors that can accommodate millimeter-scale nodes. Printing-based fabrication utilizes high-throughput processing techniques popularized by the graphic arts and display industries that are capable of achieving micron-scale feature resolution while depositing at meter per second print speeds. Furthermore, these approaches use additive processing methods, as opposed to subtractive processes used in conventional manufacturing, to limit material waste and lower overall costs.^[25] As a result, printing techniques allow significant design flexibility and customizable device form factors that can ease system integration and complexity.

Within the printed electronics community, a range of printing methods are used to fabricate devices including batteries, transistors, solar cells, antennas, and sensors.^[26–30] Printing methods are chosen based on both device and materials requirements and have tradeoffs between factors such as throughput, resolution, and cost.^[31–33] Table 1.3 outlines the differences between these printing methods, describing the important factors that control patterning performance and the materials properties that should be considered when designing a printable ink.

Table 1.3: Critical parameters for various printing methods used in printed electronics

Printing Technique	Viscosity Range (cP)	Line Width (μm)	Layer Thickness (μm)	Max Speed (m/s)	Method, Pattern Design Cost
Gravure	10 – 1,000	1	0.01 – 10	15	Contact, High
Screen	500 – 50,000	20	1 – 250	1	Contact, Medium
Flexography	50 – 500	50	0.1 – 10	10	Contact, Low
Inkjet	1 – 50	10	0.01 – 1	1	Non-Contact, Free
3D (FDM, SLA)	> 1,000	50	> 10	0.1	Non-Contact, Free
Spray	1 – 100	10	0.01 – 1	0.1	Non-Contact, Free
Slot-Die	> 1,000	50	> 10	5	Non-Contact, Low

Among the printing techniques described in Table 1.3, screen printing is uniquely capable of depositing the high layer thickness (10s – 100s of μm) required to achieve high capacity electrodes for printed batteries. Thus, screen printing and stencil printing, a proxy for screen printing, are the focus of this dissertation. Screen and stencil printing are both contact based techniques, where a mesh or stencil is placed in contact with the substrate to define the print area, known as the cell, as shown in Figure 1.8. Ink is then deposited in the cell and a blade pushes the ink to completely fill the cell. Finally, the mesh or stencil is released from the substrate, leaving the printed feature remaining on the substrate. Quality of the resulting print is largely tied to ink design, which is dependent on two fundamental rheological properties: surface energy and viscosity. Surface energy and viscosity influence how an ink flows through the stencil and transfers onto the substrate. This impacts both the printing resolution, or the minimum possible feature size, and printing artifacts and defects, or the reliability of ink deposition at desired locations only. Thus, in order to print battery components at small form factors, surface energy and viscosity must be considered.

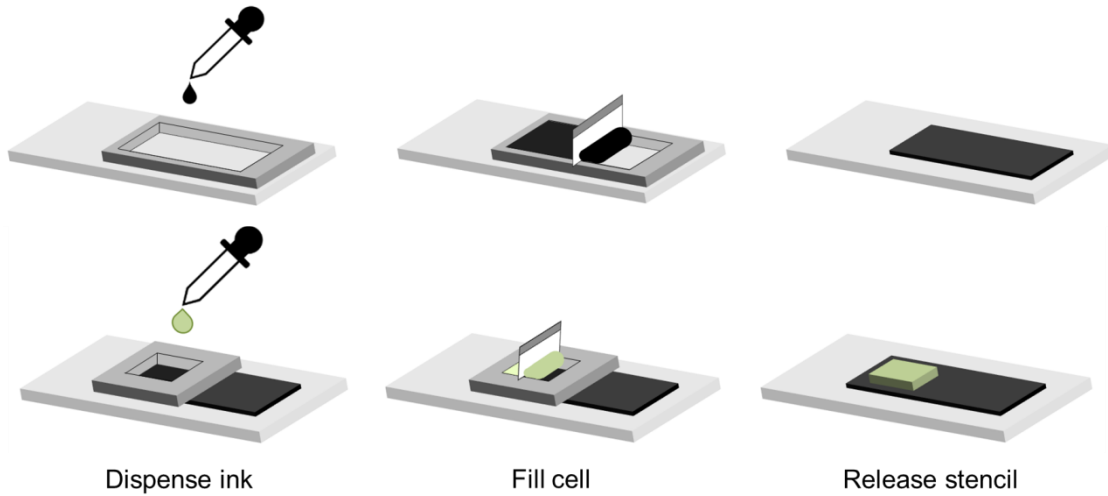


Figure 1.8: Schematic representation of screen and stencil printing, highlighting the fundamental steps involved using a contact based printing method.

When an ink is dispensed onto a surface, a thermodynamic equilibrium is established between the substrate (solid phase), the ink (liquid phase), and the ambient atmosphere above the substrate and printed feature (vapor phase), as illustrated in Figure 1.9. Each interface has a corresponding surface energy (γ_{SL} : solid – liquid, γ_{LV} : liquid – vapor, γ_{SV} : solid – vapor) based on the interaction forces at the interface. Balance of surface energies between each of the phases can be defined by the Young-Dupre equation shown below:

$$\gamma_{SV} = \gamma_{SL} + \gamma_{LV} \cos \theta_C \quad (1.8)$$

where θ_C is the contact angle of liquid drop on the substrate. Thus, the surface properties of both the substrate and the ink can be modified to change the contact angle, which will affect the surface area of the printed feature and overall resolution capabilities of the printing technique. For printed batteries, a large contact angle is typically desired to ensure pinning of the ink to the substrate and avoid spreading of the printed film.

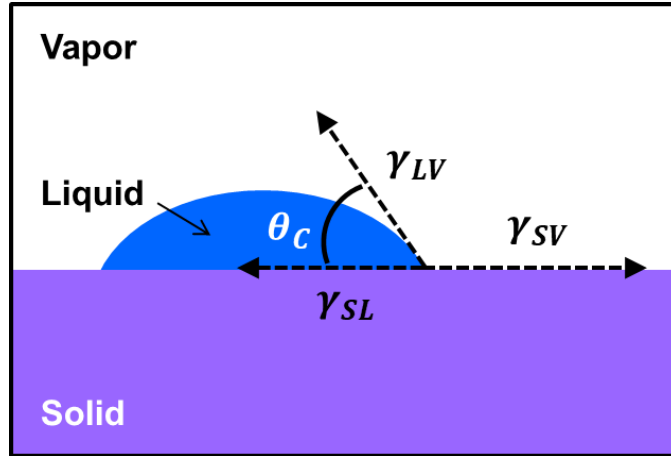


Figure 1.9: Schematic of a printed feature highlighting the surface energy and contact angle of the liquid drop

In addition to surface energy, viscosity also plays a critical role in ink printability. Viscosity is a measure of a fluid's resistance to deformation under an applied shear stress. Increases in fluid viscosity correspond to increasing resistance to shear. In most printing processes, an ink experiences shear forces due to contact with a blade or a nozzle. These shear forces can be generally described by a Couette flow, as depicted in Figure 1.10a. Here, a fluid is contained between two plates, one fixed and one moving at constant velocity u . At steady state, the fluid moves parallel to the plate and the fluid velocity varies linearly based on its proximity to the moving plate. Each layer of fluid closer to the moving plate moves faster than the layer below it, causing friction between each layer and an overall force resisting the relative motion of the fluid. An external force then must be applied to keep the top plate at a constant velocity. The magnitude F of this force is proportional to the velocity u and inversely proportional to the separation of the plates y , as described in the equation below:

$$\tau = \frac{F}{A} = \mu \frac{\partial u}{\partial y} \quad (1.9)$$

where τ is the shear stress and $\partial u/\partial y$ is the shear rate. The proportionality factor μ is the viscosity of the fluid and is commonly measured in centipoise (cP), which is equal to 0.001 Pa-s. Fluids can be classified based on their viscous response and are shown in Figure 1.10b. For example, many inks used in printed electronics exhibit shear thinning behavior due to the breakdown of cohesive forces within the fluid at higher shear rates. Thus, the viscous response of a fluid is used to characterize functional inks and determine their compatibility for a given printing technique.

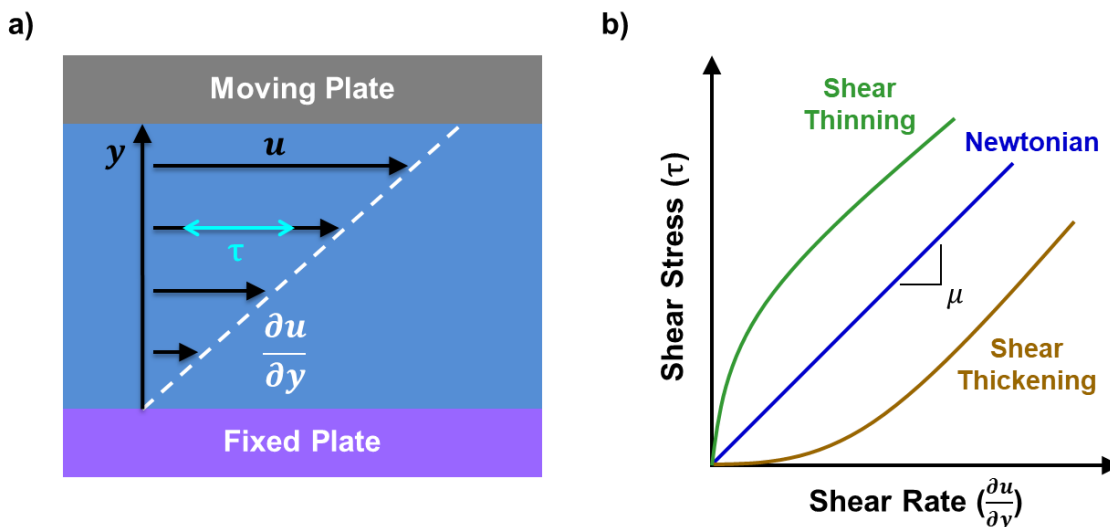


Figure 1.10: a) Illustration of a planar Couette flow showing a gradient in the velocity as a function of distance from the fixed plate. b) Categories of materials based on their viscous response to shear rate (Newtonian versus non-Newtonian).

1.4 Developing Materials for Printed Batteries

Printed batteries are an emerging solution for powering wireless electronic systems, utilizing additive manufacturing techniques to achieve novel form factors and geometries that can be integrated with IoT devices. Printed batteries rely on additive processing techniques to deposit functional inks with high accuracy, high throughput, and low cost onto a variety of substrate materials.^[26,34–36] Development of printed batteries hinges on two key goals: 1) creating functional electrode, separator, and current collector inks and 2) implementing suitable printing techniques to achieve high battery integrity and performance. Current research on printed batteries has focused on each of these goals, demonstrating various printed battery architectures using a few different cell chemistries and printing techniques.

As discussed in Section 1.2.1, a battery is composed of an anode, cathode, electrolyte, separator, and current collectors. To create a printed battery, a printable ink must be designed for each of these components. A typical ink contains an active component and a solvent and may also incorporate binders, conductive fillers, and additives.^[37] The active component provides the characteristic features required for the specific application and can be metallic, ceramic, semiconducting, organic, or a combination thereof. The solvent enables printability of the ink as it controls many of the rheological properties of the ink. The solvent should provide good solubility to each component of the ink as well as suitable viscosity, surface tension, and homogeneity. Solvent selection is also critical in order to print multilayer devices such as batteries since the solvent present in the printed film can potentially dissolve or damage the preceding layer. Binders are often employed in printing inks to help homogenize the active components into the ink. After printing, binders also help maintain particle-particle contact as the solvent evaporates and keep the printed film pinned to the substrate. Finally, conductive fillers are often used in electrodes to increase electrical conductivity and additives can be used to tailor ink properties that may affect their rheology, wetting, or corrosion resistance.

Battery component inks are optimized based on their rheological properties, including surface energy and viscosity, and materials properties that determine battery performance. For example, battery electrodes must be able to deliver high capacity, so thicker films are often desired. This requires higher mass loading of the active component in electrode inks, which results in higher viscosity inks that may not be compatible with all printing methods. Additionally, printed current collectors must maintain high electronic conductivity and good adhesion to the substrate. This requires careful selection of the current collector ink solvent to ensure the ink forms a conformal coating on the substrate. Table 1.4 provides a complete overview of the rheological and materials properties that must be considered for developing printable battery inks. To date, printable inks have been formulated for nearly all of the printing techniques discussed in Section 1.3, including inkjet, screen, stencil, extrusion, spray, and flexography printing.^[38–41]

Table 1.4: Material and rheological property requirements for battery components

Component	Requirements
Electrodes	High capacity (thick films) High surface area (porous films) Moderate electronic conductivity (good particle-particle contact) Materials compatibility and corrosion resistance (solvent, binder, additives)
Electrolyte and Separator	High ionic conductivity (ionic contact between electrodes) No electronic conductivity (good physical barrier, good mechanical integrity) Materials compatibility and chemical stability (solvent, binder, additives)
Current Collectors	High electronic conductivity (thin films) Good substrate adhesion (low surface energy) Materials compatibility and corrosion resistance (solvent, binder, additives)

Given the unique advantages of printed batteries, several demonstrations have been reported in the literature, typically using Zn-MnO₂^[42–48], Zn-Ag₂O^[49–53], and Li-ion^[54–59] chemistries. A few other cell chemistries, including Ni-Zn, Li-S, Na-ion, Fe-air, and Zn-air, have also been recently incorporated as printed batteries although the literature on each is less extensive.^[60–65] Primarily focusing on wearable device applications, these studies have demonstrated flexible and stretchable electrode, separator, and current collector materials that can be incorporated in roll-to-roll based processing. To date, printed batteries have achieved areal capacities between 1 – 5 mAh cm⁻², as shown in Figure 1.11, and have been embedded in a variety of novel form factors, including tattoo, fabric, and wire based cells. While volumetric capacity or power density would be more suitable to compare printed battery performance across several battery architectures and chemistries, sufficient data is not provided from all sources listed in Figure 1.11 to compare volumetric capacity or power density.

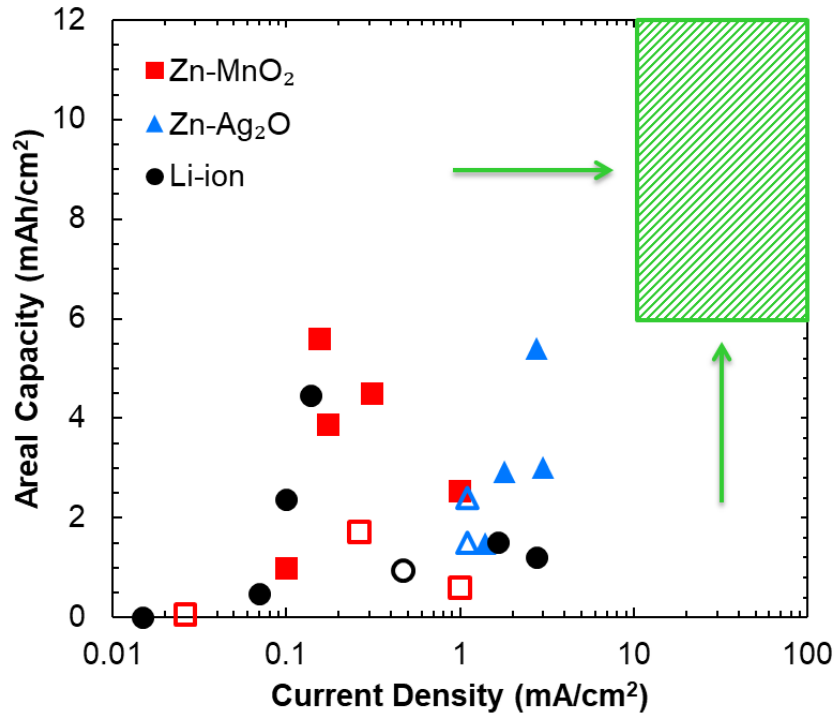


Figure 1.11: Ragone plot comparing performance of printed batteries from the literature. Open symbols represent batteries using non-printed separators, while filled symbols represent fully-printed cells. The green highlighted section represents the performance benchmarks required to support the IoT driver shown in Figure 1.2.

1.5 Remaining Challenges for Printed Batteries

Despite the advancements made within the printed battery community, further work is needed to incorporate printed batteries with integrated electronics. While previous studies have primarily focused on developing inks for various printing techniques, none have emphasized scaling printed battery size and power to accommodate typical IoT system requirements. For example, many of the printed battery demonstrations have used planar geometries, which can reduce power density and electrode utilization and increase internal resistance and device footprint. In addition, thin printed electrodes are commonly implemented to minimize strain in the battery under flexion or tension, thus reducing battery capacity. Moreover, several printed battery configurations have included non-printed components, such as evaporated current collectors and mesh supports in the electrodes or electrolyte, that are difficult to incorporate into high throughput assemblies and add to the overall size and cost of the battery. Given all of these constraints, printed battery architectures have typically been larger than 1 cm^2 , operated at current densities below 3 mA cm^{-2} , and exhibited power densities well below 10 mW cm^{-2} , thus impeding the incorporation of printed batteries for wireless electronic systems via on-chip integration.

In order to utilize printed batteries for WSNs, several limitations in printed battery processing, architecture, and performance must be addressed. Most importantly, battery footprints must scale to device relevant geometries in order to integrate battery fabrication with wafer-level and chip-scale packaging. This will require vertical cell designs to minimize battery footprints,

which presents new processing challenges and considerations for printed batteries. For example, materials compatibility will become paramount to device functionality, so printing schemes must take solvent selection, surface adhesion, and processing temperatures into account to ensure successful multilayer battery assembly.

In addition, non-printed components often used in printed batteries must be replaced with additively manufactured components to lower processing costs and accommodate a wide range of IoT device architectures. Typically, current collectors, separators, and cell packaging are non-printed, limiting design flexibility and often preventing integration with single chip nodes. This will require lower thermal budgets for printed battery components to ensure compatibility with an assortment of substrate materials, including low-cost flexible substrates and semiconductor packaging flows.

Finally, studies on printed batteries must provide greater detail on performance metrics and justify their applicability for device integration. This must either include battery lifetime data to justify implementation with IoT devices or further information on battery degradation mechanisms to motivate further studies addressing cell instabilities. Furthermore, printed battery research must push towards higher capacities, higher operating current densities, and higher power densities to enable battery technologies that meet the IoT performance benchmarks outlined in Figure 1.2 and highlighted in green in Figure 1.10. Correspondingly, further information must be provided in future works to permit detailed comparison to performance benchmarks, including information on electrode thickness and area, operating currents, and cell potentials.

1.6 Dissertation Organization

This dissertation addresses several challenges associated with designing millimeter-scale energy storage for IoT technologies, utilizing printing techniques to create batteries that could enable scalable wireless sensor networks. Among several possible chemistries, Zn-based batteries are explored as printable energy storage devices for integrated electronics given their high energy densities, high discharge rate capabilities, and good charge retention.^[18] Furthermore, Zn battery chemistries are well suited for integrated electronics since they do not require inert environments for fabrication, have modest packaging and material handling requirements, and use low-cost, earth-abundant materials.

The approach taken in this work goes beyond previous printed battery research by not only creating battery materials and incorporating additive manufacturing techniques, but also characterizing important battery materials properties, addressing battery failure mechanisms, and establishing performance benchmarks that are compatible with IoT device requirements. This work also aims to serve as a roadmap for future research on printed batteries across any battery chemistry or device architecture. With an application driven emphasis, this dissertation provides guidelines across the five main pillars of materials science (processing, structure, properties, performance, and characterization) for energy storage scalability and integration for WSNs.

Chapter 2 investigates the scaling limits of a fully-printed, primary Zn-Ag₂O battery with a vertical cell geometry. Design requirements for printing a multilayer, vertical cell architecture are considered, focusing on electrode and separator layer optimization and maintaining a thermal budget compatible with low-cost flexible substrates and semiconductor packaging flows. Printed battery stability metrics are established, identifying Zn corrosion as the limiting failure

mechanism. Tradeoffs between electrode geometry and battery performance metrics including capacity, internal resistance, and cell lifetime are also determined.

Chapter 3 establishes a printed air cathode for metal-air batteries that can be fabricated below 100 °C, broadening the potential for metal-air batteries to power integrated electronics. Utilizing additive manufacturing and low processing temperatures, printed cathodes compatible with wafer-level and chip-scale packaging are presented. The importance of binder, solvent, and catalyst interactions and their influence on air cathode performance as a function of processing temperature are examined. Furthermore, this work leverages the printing and ink development from Chapter 2 to create one of the first demonstrations of a printed Zn-air battery, displaying higher power density capabilities than the Zn-Ag₂O batteries shown in Chapter 2.

Chapter 4 addresses Zn corrosion, the limiting failure mechanism for printed Zn-based batteries. *Operando* characterization techniques are implemented to couple electrochemical measurements with chemical and structural information to directly observe the non-equilibrium reactions occurring at the Zn-electrolyte interface. Battery materials and processing conditions are rapidly screened using *operando* pressure decay measurements in printed Zn-air batteries to determine trends in corrosion rates. Additionally, *operando* diffraction experiments using a synchrotron X-ray source are conducted to illustrate the effect of salient processing and materials parameters on Zn corrosion.

Chapter 5 provides integration strategies for printed batteries and tests proof of concept cells under typical WSN operation modes. Printable packaging and interconnects are explored using extrusion, inkjet, and stencil printing approaches. Zn-Ag₂O batteries are tested under pulsed discharge conditions to mimic single chip node operation in a WSN. Screen printed arrays are also investigated for high-voltage and high-power applications. Ink design and cell performance for screen printed arrays are compared to stencil printed cells shown in Chapter 2.

Finally, Chapter 6 summarizes the work presented in this dissertation and offers future research directions to address the critical remaining challenges for integrated energy storage. Alternative battery chemistries and geometries are suggested given the limitations of Zn batteries.

1.7 References

- [1] L. Atzori, A. Iera, G. Morabito, *Comput. Networks* **2010**, *54*, 2787.
- [2] U. Raza, P. Kulkarni, M. Sooriyabandara, *IEEE Commun. Surv. Tutorials* **2017**, *19*, 855.
- [3] I. F. Akyildiz, W. Su, Y. Sankarasubramaniam, E. Cayirci, *Comput. Networks* **2002**, *38*, 393.
- [4] B. Warneke, M. Last, B. Liebowitz, K. S. J. Pister, *Computer (Long. Beach. Calif.)* **2001**, *34*, 44.
- [5] J. M. Kahn, R. H. Katz, K. S. J. Pister, *J. Commun. Networks* **2000**, *2*, 188.
- [6] M. D. Scott, B. E. Boser, K. S. J. Pister, *IEEE J. Solid-State Circuits* **2003**, *38*, 1123.
- [7] B. W. Cook, S. Lanzisera, K. S. J. Pister, *Proc. IEEE* **2006**, *94*, 1177.
- [8] J. Carballo, W. Chan, A. B. Kahng, M. Kakimoto, S. Nath, T. Saito, K. Seto, G. Smith, I. Yamamoto, in *Int. Technol. Roadmap Semicond. 2.0*, **2015**.
- [9] A. Raj, D. Steingart, *J. Electrochem. Soc.* **2018**, *165*, B3130.
- [10] D. Steingart, in *Energy Harvest. Technol.*, **2009**, pp. 267–286.
- [11] D. Steingart, S. Roundy, P. K. Wright, J. W. Evans, *MRS Bull.* **2008**, *33*, 408.
- [12] M. R. Lukatskaya, B. Dunn, Y. Gogotsi, *Nat. Commun.* **2016**, *7*, 1.
- [13] S. Kim, R. Vyas, J. Bitto, K. Niotaki, A. Collado, A. Georgiadis, M. M. Tentzeris, *Proc. IEEE* **2014**, *102*, DOI 10.1109/JPROC.2014.2357031.
- [14] F. K. Shaikh, S. Zeadally, *Renew. Sustain. Energy Rev.* **2016**, *55*, 1041.
- [15] J. Rabaey, F. Burghardt, D. Steingart, M. Seeman, P. Wright, in *IEEE Int. Electron Devices Meet.*, **2007**, pp. 363–366.
- [16] S. Roundy, D. Steingart, L. Frechette, P. Wright, J. Rabaey, in *Wirel. Sens. Networks*, **2004**, pp. 1–17.
- [17] M. S. Whittingham, *Proc. IEEE* **2012**, *100*, 1518.
- [18] T. B. Reddy, *Linden's Handbook of Batteries*, McGraw-Hill, New York, **2011**.
- [19] J. Newman, K. E. Thomas-Alyea, *Electrochemical Systems*, Wiley, Hoboken, New Jersey, **2004**.
- [20] E. Maiser, in *AIP Conf. Proc.*, **2014**, pp. 204–218.
- [21] J. M. Tarascon, M. Armand, *Nature* **2001**, *414*, 359.
- [22] S. D. Beattie, D. M. Manolescu, S. L. Blair, *J. Electrochem. Soc.* **2009**, *156*, A44.
- [23] J. Nelson Weker, M. F. Toney, *Adv. Funct. Mater.* **2015**, *25*, 1622.
- [24] Y. Cao, M. Li, J. Lu, J. Liu, K. Amine, *Nat. Nanotechnol.* **2019**, *14*, 200.
- [25] J. Perelaer, P. J. Smith, D. Mager, D. Soltman, S. K. Volkman, V. Subramanian, J. G. Korvink, U. S. Schubert, *J. Mater. Chem.* **2010**, *20*, 8446.
- [26] A. M. Gaikwad, C. Arias, D. A. Steingart, *Energy Technol.* **2015**, *3*, 305.
- [27] A. C. Arias, J. D. MacKenzie, I. McCulloch, J. Rivnay, A. Salleo, *Chem. Rev.* **2010**, *110*, 3.
- [28] S. Khan, L. Lorenzelli, R. S. Dahiya, *IEEE Sens. J.* **2015**, *15*, 3164.
- [29] V. Subramanian, J. M. J. Fréchet, P. C. Chang, D. C. Huang, J. B. Lee, S. E. Molesa, A. R. Murphy, D. R. Redinger, S. K. Volkman, *Proc. IEEE* **2005**, *93*, 1330.
- [30] W. Wu, *Nanoscale* **2017**, *9*, 7342.
- [31] B. E. Kahn, *Proc. IEEE* **2015**, *103*, 497.
- [32] R. R. Søndergaard, M. Hösel, F. C. Krebs, *J. Polym. Sci. Part B Polym. Phys.* **2013**, *51*, 16.
- [33] S. Cruz, L. A. Rocha, J. C. Viana, in *Flex. Electron.*, **2018**, pp. 47–70.

- [34] R. E. Sousa, C. M. Costa, S. Lanceros-møndez, *ChemSusChem* **2015**, *8*, 3539.
- [35] F. Zhang, M. Wei, V. V. Viswanathan, B. Swart, Y. Shao, G. Wu, C. Zhou, *Nano Energy* **2017**, *40*, 418.
- [36] K. Choi, D. B. Ahn, S. Lee, *ACS Energy Lett.* **2018**, *3*, 220.
- [37] J. Kim, R. Kumar, A. J. Bando, J. Wang, *Adv. Elec* **2017**, *3*, 1600260.
- [38] Z. Wang, R. Winslow, D. Madan, P. K. Wright, J. W. Evans, M. Keif, X. Rong, *J. Power Sources* **2014**, *268*, 246.
- [39] B. Kim, R. Winslow, I. Lin, K. Gururangan, J. Evans, P. Wright, *J. Phys. Conf. Ser.* **2015**, *660*, DOI 10.1088/1742-6596/660/1/012009.
- [40] S. H. Lee, A. Mahadevegowda, C. Huang, J. D. Evans, P. S. Grant, *J. Mater. Chem. A* **2018**, *6*, 13133.
- [41] S. D. Lacey, D. J. Kirsch, Y. Li, J. T. Morgenstern, B. C. Zarket, Y. Yao, J. Dai, L. Q. Garcia, B. Liu, T. Gao, S. Xu, S. R. Raghavan, J. W. Connell, Y. Lin, L. Hu, *Adv. Mater.* **2018**, *30*, 1.
- [42] C. C. Ho, J. W. Evans, P. K. Wright, *J. Micromech. Microeng.* **2010**, *20*, 104009.
- [43] A. M. Gaikwad, G. L. Whiting, D. A. Steingart, A. C. Arias, *Adv. Mater.* **2011**, *23*, 3251.
- [44] A. M. Gaikwad, A. M. Zamarayeva, J. Rousseau, H. Chu, I. Derin, D. A. Steingart, *Adv. Mater.* **2012**, *24*, 5071.
- [45] G. A. Ghiurcan, C. Liu, A. Webber, F. H. Feddrix, *J. Electrochem. Soc.* **2003**, *150*, 922.
- [46] E. Madej, M. Espig, R. R. Baumann, W. Schuhmann, F. La Mantia, *J. Power Sources* **2014**, *261*, 356.
- [47] W. Lao-atiman, T. Julaphatachote, P. Boonmongkolras, S. Kheawhom, *J. Electrochem. Soc.* **2017**, *164*, 859.
- [48] A. M. Gaikwad, H. N. Chu, R. Qeraj, A. M. Zamarayeva, D. A. Steingart, *Energy Technol.* **2013**, *1*, 177.
- [49] K. T. Braam, S. K. Volkman, V. Subramanian, *J. Power Sources* **2012**, *199*, 367.
- [50] K. Braam, V. Subramanian, *Adv. Mater.* **2014**, *27*, 689.
- [51] C. C. Ho, K. Murata, D. A. Steingart, J. W. Evans, P. K. Wright, *J. Micromech. Microeng.* **2009**, *19*, 094013.
- [52] R. Kumar, J. Shin, L. Yin, J. You, Y. S. Meng, J. Wang, *Adv. Energy Mater.* **2017**, *7*, 1602096.
- [53] S. Berchmans, A. J. Bando, W. Jia, J. Ram, Y. S. Meng, J. Wang, *J. Mater. Chem. A* **2014**, *2*, 15788.
- [54] A. M. Gaikwad, B. V. Khau, G. Davies, B. Hertzberg, D. A. Steingart, A. C. Arias, *Adv. Energy Mater.* **2015**, *5*, 1401389.
- [55] K. Sun, T. Wei, B. Y. Ahn, J. Y. Seo, S. J. Dillon, J. A. Lewis, *Adv. Mater.* **2013**, *25*, 4539.
- [56] H. Kim, J. Proell, R. Kohler, W. Pfleging, A. Pique, *J. Laser Micro/Nanoengineering* **2012**, *7*, 320.
- [57] Q. Chen, R. Xu, Z. He, K. Zhao, L. Pan, *J. Electrochem. Soc.* **2017**, *164*, 1852.
- [58] T. Wei, B. Y. Ahn, J. Grotto, J. A. Lewis, *Adv. Mater.* **2018**, *30*, 1703027.
- [59] M. Cheng, Y. Jiang, W. Yao, Y. Yuan, R. Deivanayagam, T. Foroozan, Z. Huang, B. Song, R. Rojaee, T. Shokuhfar, Y. Pan, J. Lu, R. Shahbazian-yassar, *Adv. Mater.* **2018**, *1800615*, 1.
- [60] Z. Wang, X. Meng, K. Chen, S. Mitra, *Adv. Mater. Interfaces* **2018**, *5*, 1.
- [61] C. Milroy, A. Manthiram, *Chem. Commun.* **2016**, *52*, 4282.

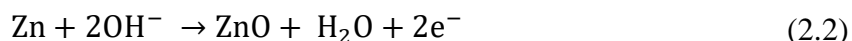
- [62] J. Ding, K. Shen, Z. Du, B. Li, S. Yang, *ACS Appl. Mater. Interfaces* **2017**, *9*, 41871.
- [63] H. A. Figueredo-Rodríguez, R. D. McKerracher, M. Insausti, A. G. Luis, C. P. de León, C. Alegre, V. Baglio, A. S. Aricò, F. C. Walsh, *J. Electrochem. Soc.* **2017**, *164*, A1148.
- [64] M. Hilder, B. Winther-Jensen, N. B. Clark, *J. Power Sources* **2009**, *194*, 1135.
- [65] M. Hilder, B. Winther-Jensen, N. B. Clark, *Electrochim. Acta* **2012**, *69*, 308.

Chapter 2: Scaling Printed Zn-Ag₂O Batteries for Integrated Electronics

2.1 Introduction

Printed batteries are an emerging solution for integrated energy storage using low-cost, high-accuracy fabrication techniques. While several printed batteries have been previously reported, few have designed a battery that could be incorporated into an integrated device. Specifically, a fully-printed battery with a small active electrode area ($< 1 \text{ cm}^2$) achieving high areal capacities ($> 10 \text{ mAh cm}^{-2}$) at high current densities ($1\text{-}10 \text{ mA cm}^{-2}$) has not been demonstrated, which represents the minimum form-factor and performance requirements for many low-power device applications, as discussed in Section 1.5. This chapter addresses these challenges by investigating the scaling limits of a fully-printed Zn-Ag₂O battery and determining the electrochemical limitations for a mm²-scale battery.

Zn-Ag₂O is the chosen electrochemistry for our printed battery given its inherent air stability, high energy density (130 Wh kg^{-1}), high discharge rate capability, and good charge retention.^[1,2] This system uses a zinc anode and a monovalent silver oxide cathode with an aqueous potassium hydroxide (KOH) electrolyte, as shown in Equations 2.1–2.3. Zn-Ag₂O batteries have a theoretical open-circuit potential of about 1.6 V, but operating voltages are typically 1.4–1.5 V, which is still suitable for most low-power device applications. Unlike manganese oxide or lithium-ion batteries, silver oxide batteries maintain a steady discharge voltage over a wide range of discharge rates. This is desirable for integration with IoT devices in order to minimize power electronics requirements and reduce circuit design complexity. For example, silver oxide cells can better handle the current spikes typically seen during radio transmission bursts in IoT devices. Furthermore, silver oxide batteries can be fabricated without the use of inert environments, making them better suited for high throughput manufacturing compared to Li-ion chemistries and allowing for integration into existing chip packaging and assembly process flows.



Using stencil printing to achieve thick electrodes, a vertical cell geometry is established to achieve a fully-printed, primary Zn-Ag₂O battery with low internal resistance and high areal capacity that meet the IoT benchmarks for low-power devices. Ink design for each battery component is discussed, highlighting the materials and processing requirements needed to implement a multilayer printing approach and maintain compatibility with existing semiconductor packaging flows. Important factors affecting printed battery lifetime are characterized, including separator layer pore size and electrode area, which set processing limitations for the printed battery architecture. Finally, power density, internal resistance, and areal capacity measurements are performed to determine battery performance as a function of electrode area.

2.2 Printed Battery Architecture and Processing

Stencil printing is implemented to achieve thick, high-capacity electrodes. Figure 2.1 depicts the stencil printing procedure, where a plastic stencil is used to define the pattern, ink is dispensed into the stencil, and a doctor blade pushes the ink to fill the stencil and form the printed film. Analogous to screen printing, stencil printing utilizes high-mass-loading, high-viscosity inks ($> 1,00$ cP) in order to print thick electrode films and achieve high-capacity electrodes.^[3] Moreover, stencil printing does not require the high upfront design cost of creating a screen and allows for faster prototyping and iteration of cell designs.

Electrode thicknesses ranging from 10s to 100s of μm can be deposited on a variety of substrates including rigid wafers and flexible plastics with high pattern accuracy. Compared to inkjet printing or spray deposition, stencil printing is capable of depositing thicker electrodes and is better suited to achieve high capacity electrodes. In our battery architecture, each layer is stencil printed directly on top of the preceding layer to minimize the battery footprint, with the zinc anode as the bottom electrode. After the silver oxide cathode is printed on top of the sol-gel separator, an encapsulation layer is laminated to the substrate and the top current collector is connected to the cathode. Here, we utilize a spin-coated polydimethylsiloxane (PDMS) encapsulation layer, which has been previously shown to be printable.^[4,5]

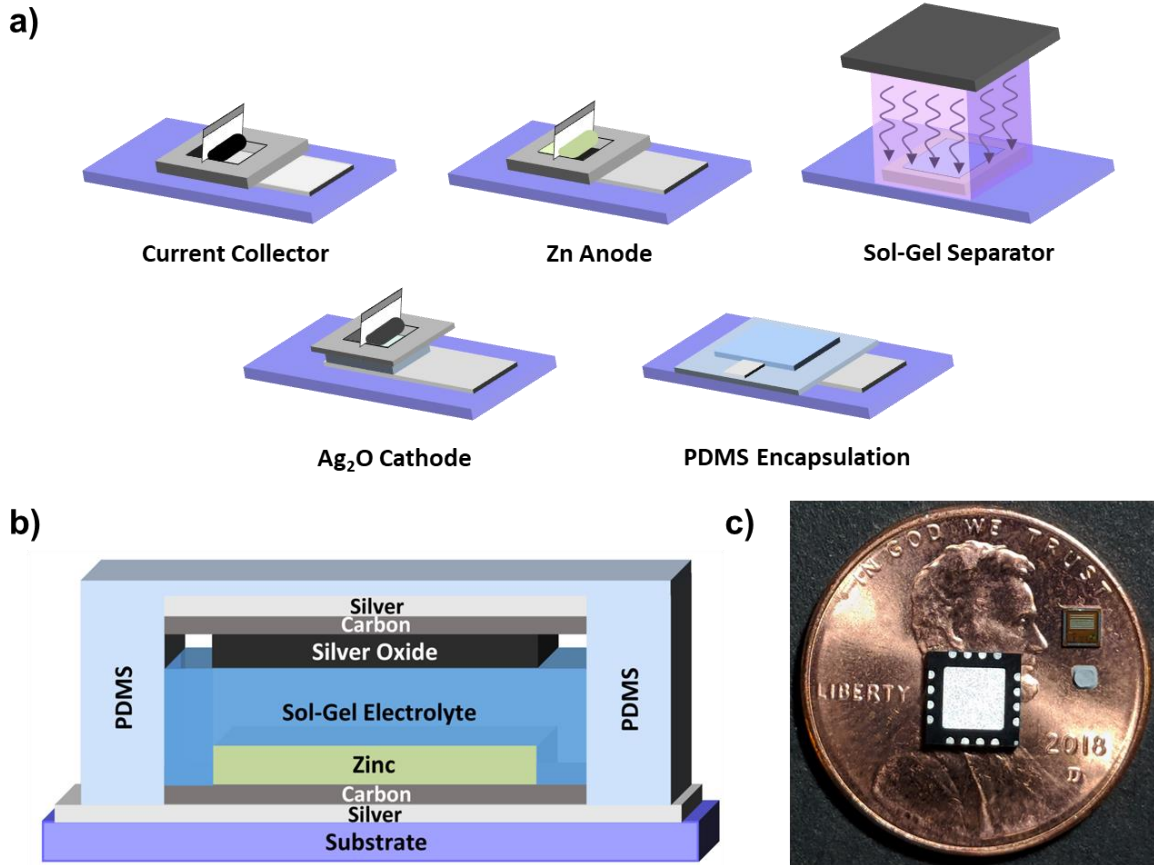


Figure 2.1: a) Schematic representation of the battery fabrication process. b) Cross-sectional view of the printed Zn-Ag₂O battery. c) 1 mm² printed Zn anode compared to a commercially packaged device and an unpackaged chip.

2.2.1 Current Collectors

Battery electrodes are typically thick and porous to enhance battery capacity; so thin current collectors are used to provide a conductive pathway to the positive and negative terminals and minimize internal resistance. Current collectors must not only be highly conductive to ensure efficient charge transfer to and from the battery, but also physically and chemically robust in the presence of the electrolyte in order to maintain good contact with the electrodes. In many printed battery designs, current collectors are commonly excluded from the printed architecture, relying on traditional, non-printed current collectors including foils, meshes, or evaporated films.^[6-9]

In order to eliminate non-printed components from the battery, silver inks have recently been used to print current collectors^[8,10-12], but silver is known to swell and thicken in the presence of concentrated KOH and can crack or delaminate from the substrate.^[13,14] Initially, we attempted O₂-plasma surface treatments to improve adhesion between printed silver films and both glass and PET substrates but were unable to find a suitable set of conditions to prevent film delamination in concentrated KOH solutions. Instead, carbon was proposed as an alternative current collector material, given its chemical and physical compatibility with KOH.

A commercially available carbon ink (Creative Materials #112-48) was used to stencil print carbon films on PET substrates. Carbon films were printed with a Kapton tape stencil to achieve a film thickness of ~50 μm (Figure 2.2a). Film resistivity was measured as a function of annealing temperature and time and was found to plateau at 110 °C with values of ~ 1 x 10⁻³ Ω-cm, or about three orders of magnitude higher than bulk silver (Figure 2.2b). At 110 °C, film compaction was observed by SEM, so the high measured resistance was not attributed to poor particle-particle contact in the printed film (Figure 2c). Printed carbon sheet resistance was found to be around 10 Ω □⁻¹ on glass and slightly higher on PDMS, compared to about 1 Ω □⁻¹ for printed silver (Figure 2.2d). Since the carbon films would constrain the total resistance of the printed battery, we implemented a printed silver-carbon bilayer structure to provide chemical and physical stability while maintaining good conductivity (2-3 Ω □⁻¹). The silver layer (Creative Materials #120-07) was printed on both PET and glass substrates with a Kapton tape stencil and annealed in an oven at 110 °C for 15 min. The carbon layer was then printed on top of the silver layer and annealed at 110 °C for 30 min. Finally, silver-carbon bilayers were also tested for stability in KOH. A few bilayers were printed on PET and immersed in 8.4M KOH for 100 hours and showed minimal change in film resistivity and no signs of delamination or cracking.

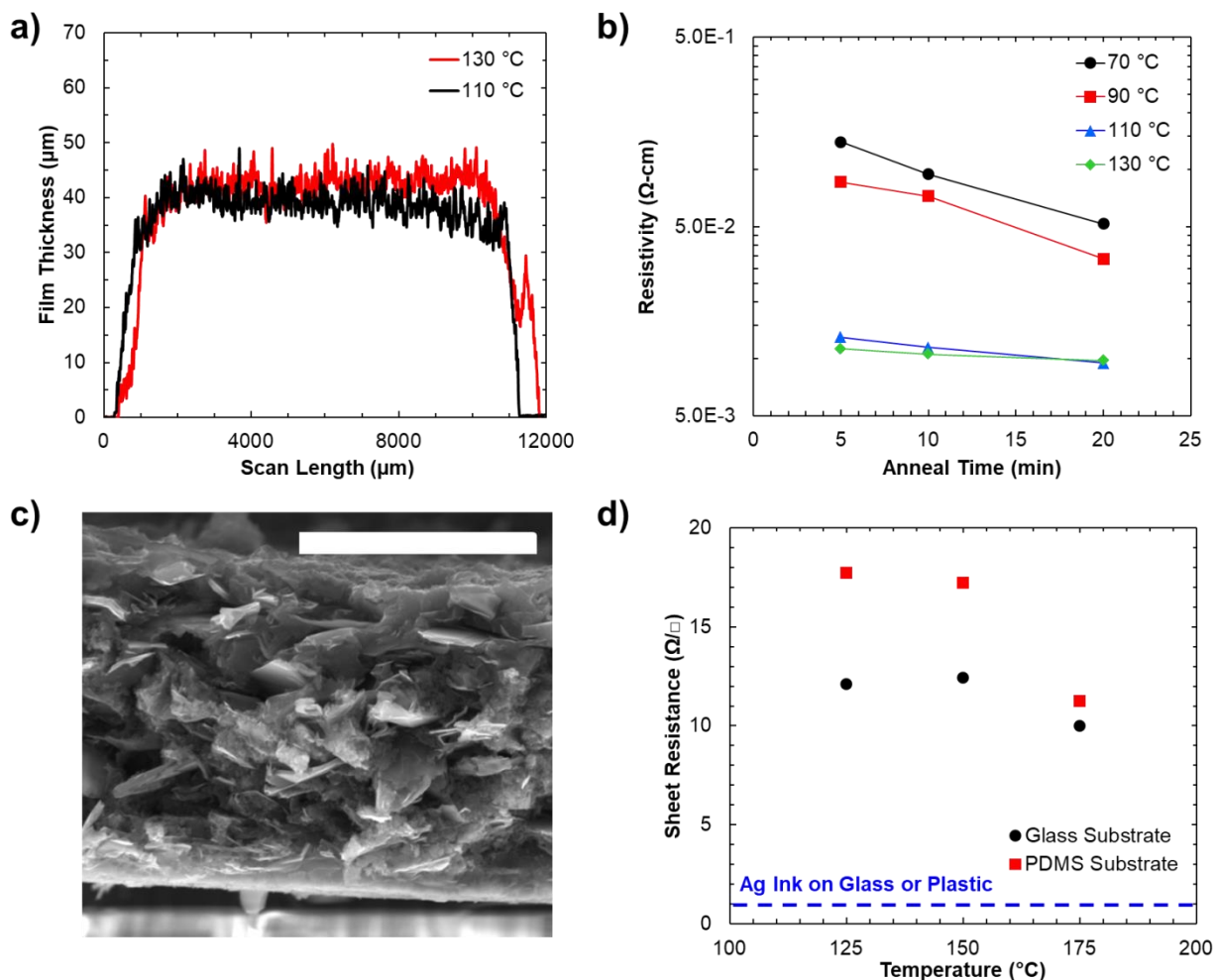


Figure 2.2: a) Typical thickness profile of a printed carbon film. b) Printed carbon film resistivity at annealing temperatures between 70–130 °C. c) Cross-section SEM image of printed carbon film. Scale bar is 30 μm . d) Comparison of printed carbon and printed silver sheet resistance on glass and PDMS.

2.2.2 Sol-Gel Separator and Polymer Encapsulation

Physical separation between the two electrodes is necessary to maintain a constant battery potential and to avoid forming short-circuit pathways. At the same time, the separator must provide suitable ionic conduction between the anode and cathode to allow the redox reactions at each electrode to proceed. Printed batteries often depend on the use of non-printed components for the separator [12,15–17], which requires additional assembly and adds to fabrication costs and complexity. Although some demonstrations of printed separators have been reported, many require planar electrode configurations [9,12,15,16,18–20], which can lead to poor electrode utilization and power densities while increasing the battery footprint and internal resistance.

Previously, our group reported a printable sol-gel separator using a photopolymerizable polyacrylic acid (PAA) solution.^[11] This enabled each layer of the battery to be printed consecutively with a vertical cell architecture, decreasing the battery footprint and distance

between the two electrodes. The PAA sol-gel separator is compatible with the KOH electrolyte and can be fabricated completely in air, a significant advantage for low-cost, high-throughput processing compared to Li-ion chemistries. The sol-gel separator solution was composed of an acrylic acid monomer (Sigma #147230), a crosslinker (Sigma #410195), and a photoinitiator (Sigma #410896) to facilitate crosslinking under UV exposure. The solution was prepared in two parts. First, PEO (0.092 g) was added to a solution of KOH (3.125 mL, 1M) and acrylic acid (250 μ L) and mixed at 500 rpm for 2 hours to allow the PEO to dissolve. The KOH solution was prepared by adding KOH pellets (Fisher) to DI water and mixing with a vortex mixer. Second, the crosslinker (250 μ L) and photoinitiator (19 mg) were added to the solution and mixed at 650 rpm for 15 min. Before stencil printing the sol-gel separator, the solution was bubbled with nitrogen to remove any residual oxygen for 12 min. A Spectroline SB-100P series lamp was used to UV crosslink the monomer in solution and was applied for 10 min. Finally, the sol-gel separator was soaked with \sim 30 μ L of an 8.4 M KOH electrolyte for 20 min.

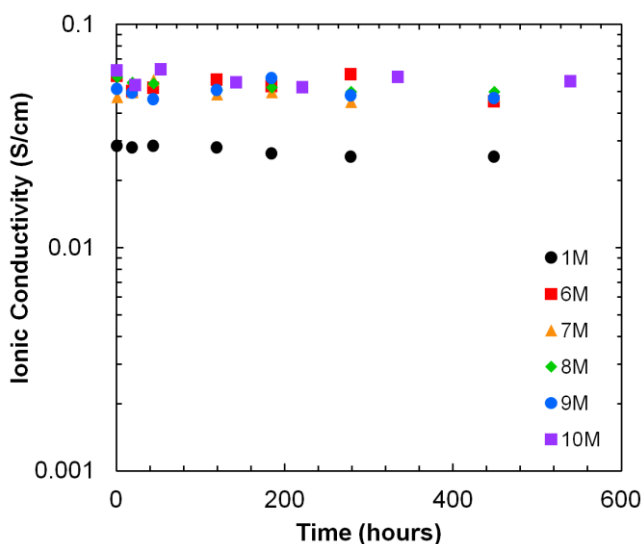


Figure 2.3: Stability of sol-gel separator ionic conductivity over time.

While promising, our previous printed battery configuration suffered from electrolyte dehydration, causing the ionic conductivity of the sol-gel separator to decrease over time and a poor battery shelf life. In order to address this issue, the battery was encapsulated in a PDMS ring, as depicted in Figure 2.1. PDMS is a good moisture barrier, preventing electrolyte dehydration and ensuring suitable ionic conductivity across the separator throughout battery operation. To demonstrate the effectiveness of the encapsulation strategy, PAA sol-gel separators were printed onto gold current collectors inside of PDMS rings. After capping each sol-gel with another gold current collector, the ionic conductivity across the electrolyte was measured for 600 hours using a Gamry Reference 600 and remained stable ($> 10 \text{ mS cm}^{-1}$) over that time span, attesting to the effectiveness of the encapsulation strategy (Figure 2.3).

2.2.3 Zinc and Silver-Oxide Electrodes

In order to develop high-capacity electrodes at device-compatible areas, electrode inks must be carefully designed to meet all processing and performance requirements. Thicker

electrodes with high active mass loadings will provide higher capacity, but electrodes must also maintain chemical and physical compatibility with the other cell components. For printed electrodes, ink composition and rheology must also be considered to ensure electrode inks are compatible with the desired printing method. For small printed batteries powering IoT devices, stencil printing is an ideal deposition technique, given that thick, high-capacity electrode films ($> 100 \mu\text{m}$) can be deposited with sub- cm^2 stencil areas. Consequently, stencil printing is compatible with wafer-level and chip-scale packaging, since batteries can be printed with similar form factors as typical silicon integrated circuit components ($\sim 0.4 - 1 \text{ mm}$ thick) and geometries smaller than the total module footprint ($< 3 \text{ cm}^2$).^[21] In this study, zinc and silver oxide inks were carefully designed to achieve these geometric requirements via stencil printing while optimizing ink composition for high capacity electrodes.

In a typical electrode ink, polymer binders are added to help form a homogenous dispersion of the active electrode material and to improve particle adhesion during drying. For our printed battery, both zinc and silver oxide electrodes used a polyethylene oxide (PEO) binder to form high viscosity slurries for stencil printing. PEO is a biodegradable, water soluble polymer and allowed us to eliminate the need for flammable solvents such as N-methylpyrrolidone that are commonly used in battery electrodes. In order to achieve the highest possible electrode capacity, the active material mass loading should be maximized relative to all other electrode ink components. Thus, we optimized each electrode formulation to minimize the amount of binder in the film while maintaining suitable ink rheology for printing.

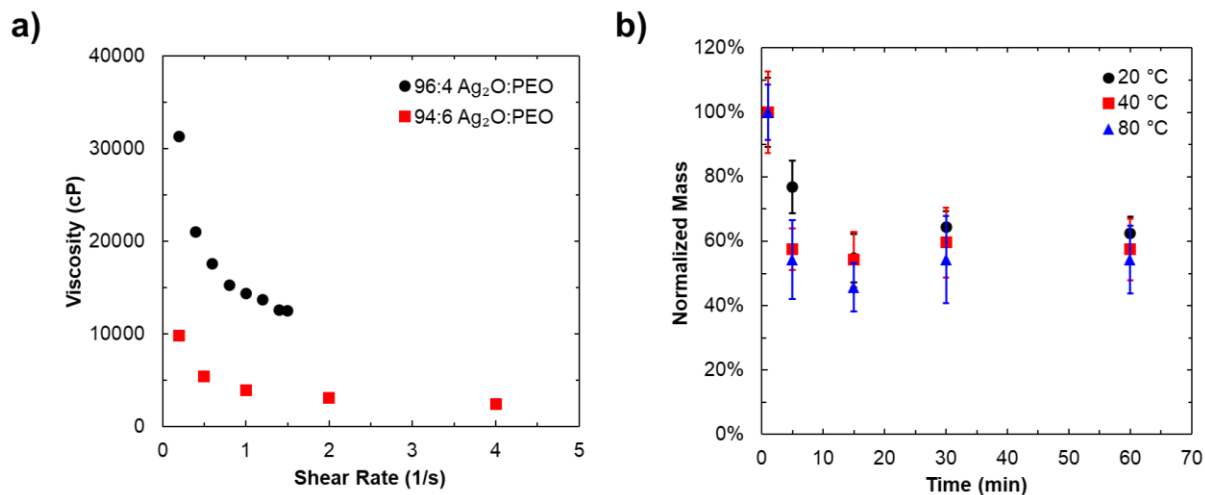


Figure 2.4: a) Ag₂O ink viscosity for two different electrode ink formulations. b) Ag₂O mass loss at different drying temperatures.

In our cell configuration, the Zn and Ag₂O electrodes were the same size; so the Ag₂O electrode limited the cell capacity and was most important component to optimize. This is also typically done in commercial Zn-Ag₂O batteries since silver oxide is the most expensive component of the battery. Ag₂O electrodes were prepared by first creating a binder solution composed of 5 wt% PEO (Sigma #182028) in DI water. The binder was stirred for 2 hours at 500 rpm to homogenize the solution. Next, the Ag₂O slurry was prepared by combining an Ag₂O powder (Strem #93-4743) with the binder in a 96/4 ratio of silver oxide to PEO by weight. The optimized silver oxide slurry demonstrated a viscosity of about 15000 cP (Figure 2.4a), which is

near the upper viscosity limit for stencil or screen printing.^[22,23] Higher silver oxide to PEO ratios resulted in highly viscous, non-homogenous slurries that were difficult to stencil print.

Since the silver oxide cathode was printed directly on the sol-gel separator, room temperature drying was chosen to prevent electrolyte dehydration and any resulting loss in ionic conductivity across the sol-gel. Silver oxide electrodes were also annealed at 40 and 80 °C and showed similar mass loss over time compared to room temperature drying (Figure 2.4b). While higher annealing temperatures may lead to silver oxide electrodes with higher electronic conductivity and better film uniformity, electrolyte dehydration was prioritized and room temperature drying was chosen. Further studies are needed to investigate the change in ionic conductivity of the sol-gel separator as a function of annealing temperature. Some initial results seem to suggest that the sol-gel separators can be annealed to mild temperatures (50 – 70 °C) and recover their original ionic conductivity after re-soaking in KOH, but shrink in size after extended exposure to elevated temperatures and may cause short-circuit pathways between the anode and cathode.

Similarly, for the zinc slurry, a 5 wt% PEO binder (Sigma #182028) was used with a 91/1 ratio of zinc (Alfa #10835) to PEO by weight. The anode film also included 5 wt% ZnO (Sigma #677450) and 3 wt% Bi₂O₃ (Alfa #40394) to suppress hydrogen gas evolution and reduce the rate of zinc corrosion.^[8,24–26] Several corrosion inhibitors have been previously explored in the literature, but Bi₂O₃ is commonly used in commercial precursors and is believed to preferentially reduce to Bi metal before Zn oxidizes and produces hydrogen gas. Additionally, ZnO is used to slow the rate of the hydrogen evolution reaction by Le Chatelier's principle. Since the zinc electrode was printed before the sol-gel separator, a heated drying step could be included to completely dry the film and improve electronic conductivity in the electrode. Through plane film resistance was measured by sandwiching printed zinc films between gold current collectors and was found to be lowest at 40 °C (Figure 2.5). Since PEO has a melting temperature at ~65 °C, it is believed that higher anode drying temperatures resulted in poor contact between zinc particles. In addition, the higher drying temperatures could have led to the formation of a zinc oxide passivation layer at the electrode surface.

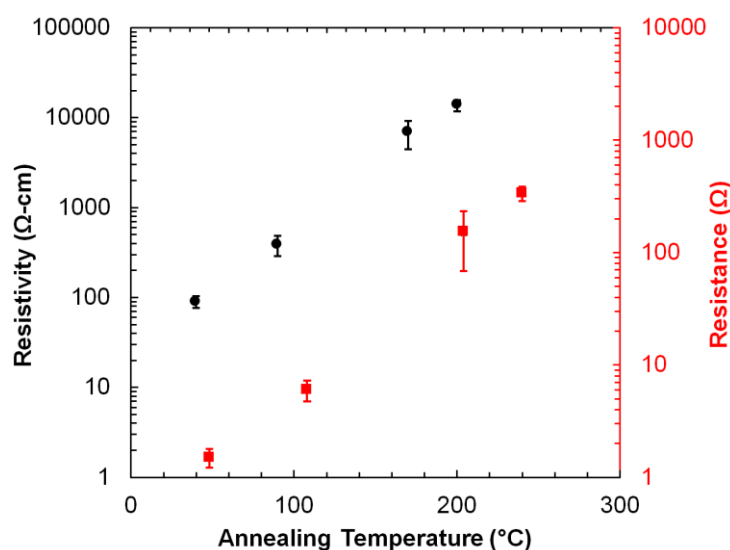


Figure 2.5: Through plane film resistivity and bulk resistance of printed Zn electrodes.

Once the electrode inks were optimized for low-temperature drying and high-mass loading, stencil printing at sub-cm² active areas was examined. Square electrode patterns were formed by laser cutting holes into 125 and 250 μm thick PET stencils with areas ranging from 25 mm² to 0.25 mm². These thicknesses were chosen to maintain a total stack thickness below 1 mm. Both Zn and Ag₂O electrodes were stencil printed on glass substrates and profile scans were used to measure the thickness of the electrodes (Figure 2.6). Printed electrodes with well-defined sidewalls and good adhesion to the substrate were observed at both thicknesses and over the entire range of electrode areas. Surface roughness was measured in the 10s of μm , as expected with stencil printing. This dictated that a separator layer with a thickness greater than 100 μm be used to prevent shorting between the two electrodes. For applications requiring further thickness scaling, it will be necessary to further reduce electrode layer roughness to allow more aggressive thickness reduction of the total battery stack.

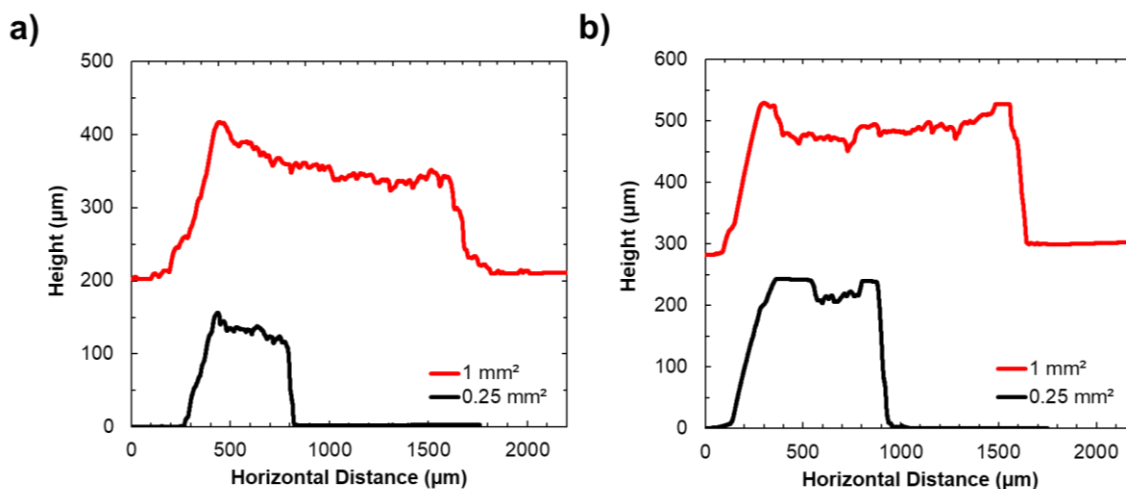


Figure 2.6: Typical thickness profiles of a) printed Zn anodes and b) printed Ag₂O cathodes.

2.3 Battery Characterization and Stability

Integrated batteries for IoT devices must not only deliver suitable performance to power the system, but also maintain electrochemical stability throughout device operation. Therefore, battery degradation must be carefully studied to prevent premature battery failure. For most low-power IoT devices, the input voltage must remain above 1 V for proper device functionality. Thus, we conducted experiments to approximate printed battery stability, defining battery open-circuit lifetime as the time at which the open-circuit voltage fell below 1 V.

In the printed Zn-Ag₂O system, electrolyte dehydration, silver oxide migration, and zinc corrosion were found to be critical degradation mechanisms that reduced cell lifetime. Although PDMS encapsulation was observed to mitigate dehydration and maintain good ionic conductivity in the separator, initial cells still demonstrated short open-circuit lifetimes (< 24 hours). These cells exhibited behavior consistent with short-circuit pathways forming across the separator as the open-circuit voltage would consistently decay to 0 V (Figure 2.7a). This behavior was attributed to silver oxide migration across the separator, a common issue in Zn-Ag₂O batteries.^[2] To mitigate this problem, a 100 μm thick carbon felt (CF) layer was added to the battery stack in between the sol-

gel separator and the silver oxide cathode. The carbon felt was used to adsorb silver oxide particles to the surface and prevent migration through the sol-gel separator. As shown in Figure 2.7a, this dramatically increased the open-circuit lifetime to ~650 hours but required the use of a non-printed component in the battery architecture.

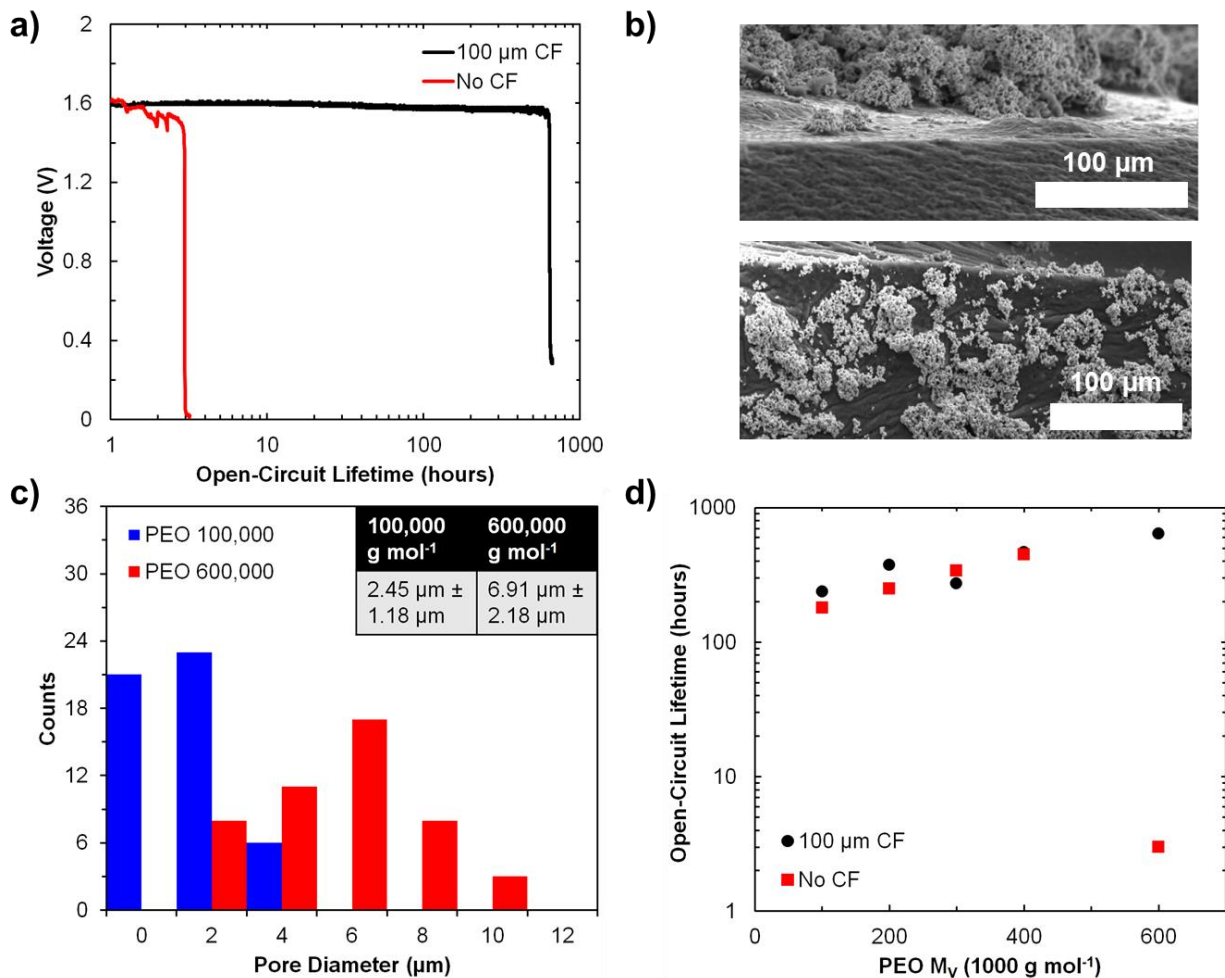


Figure 2.7: a) Printed battery open-circuit lifetime with and without 100 μm carbon felt (CF) barrier layer. b) Cross-section SEM images of Ag₂O electrode printed on sol-gel separators with PEO M_V = 100,000 g mol⁻¹ (top) and M_V = 600,000 g mol⁻¹ (bottom). After sitting for 24 hours, Ag migration only observed in high M_V sol-gel. All scale bars are 100 μm. c) Pore diameter distribution between the two sol-gel separators with average pore diameter shown in inset. d) Printed battery open-circuit lifetime for a range of PEO M_V with and without CF.

Instead of using a barrier layer to prevent silver oxide migration, we aimed to tune the porosity of the PAA sol-gel separator and eliminate the need for non-printed components in the battery stack. In our previous work, the PAA solution used high molecular weight PEO (M_V = 600,000 g mol⁻¹) to improve mechanical stability of the printed sol-gel separator.^[11] A maximum PEO concentration of 2.5 wt% was identified since higher concentrations yielded higher viscosity PAA solutions that could trap air bubbles during processing and lead to pinholes in the polymerized film. Therefore, instead of increasing the PEO concentration, the sol-gel pore size

was tuned by decreasing the PEO molecular weight. PEO has been previously used as a porogen material during sol-gel polymerization, with increasing PEO molecular weight resulting in increased sol-gel porosity.^[27] In our system, PEO occupies space within the PAA sol-gel and creates voids during the polymerization process. By keeping the PEO concentration constant while decreasing the molecular weight, the PEO should occupy more space within the sol-gel and decrease pore size.

To illustrate this effect, sol-gel separators were polymerized using a high and low PEO molecular weight (600,000 and 100,000 g mol⁻¹). Silver oxide cathodes were printed on top of the sol-gel separators that had been soaked in 8.4M KOH and were encapsulated in PDMS to prevent electrolyte dehydration. After 24 hours, the cathode-separator samples were cross sectioned and imaged using an FEI Quanta 250 FEG SEM at 20 keV (Figure 2.7b), showing silver oxide migration only in the high M_v PEO sample. Pores at the sol-gel surface were measured for each sample and smaller average sizes were found in the lower molecular weight PEO sol-gel (Figure 2.7c). Compared to the silver oxide particles, which were measured between 4 and 5 μm, the low M_v PEO sol-gel separator contained small enough pore sizes to block silver oxide migration through the separator. To confirm battery stability, full cells were printed with and without the 100 μm carbon felt layer and tested at open-circuit conditions using sol-gel separators with PEO M_v ranging from 100,000 to 600,000 g mol⁻¹ (Figure 2.7d). At PEO M_v at or below 400,000 g mol⁻¹, the printed batteries demonstrated significantly improved open-circuit lifetimes (> 200 hours) without the use of a carbon felt layer, indicating the sol-gel acted as a sufficient barrier to silver oxide migration. Additionally, PEO M_v had little impact on the ionic conductivity of the sol-gel separator, which verified that PEO content would not increase the cell internal resistance (Figure 2.8).

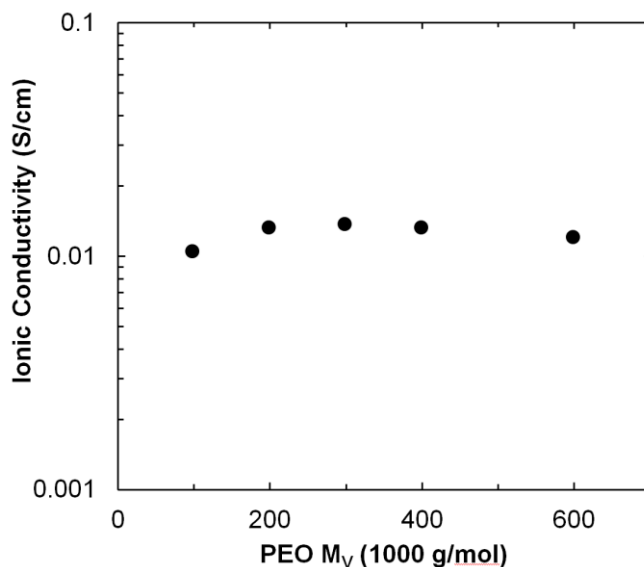


Figure 2.8: Ionic conductivity for sol-gel separators printed with various PEO M_v ranging from 100,000 to 600,000 g mol⁻¹.

After establishing the appropriate sol-gel separator formulation to impede silver oxide migration, scaling limits for the fully-printed Zn-Ag₂O battery were evaluated based on cell

performance and lifetime. First, sol-gel separators with areas ranging from 1 – 150 mm² were printed with both PEO 100,000 and 400,000 g mol⁻¹ to determine how the ionic conductivity of the sol-gel changed with size. Within the range of areas selected, each sol-gel separator had an ionic conductivity above 10 mS cm⁻¹, showing that cell size does not restrict ionic conductivity across the separator (Figure 2.9). Next, full cells were printed with electrode areas ranging from 0.0625 to 25 mm² and measured under open-circuit conditions to assess battery shelf life as a function of battery footprint. Holding all other conditions constant, we observed a decrease in battery open-circuit lifetime with decreasing electrode size (Figure 2.10a). This trend is attributed to corrosion at the zinc electrode and precipitation of zinc oxide at the anode-electrolyte interface. In the presence of highly concentrated KOH, the zinc electrode oxidizes to form a series of zincate species that further react to form zinc oxide, which passivates the electrode-electrolyte interface and inhibits charge transfer.^[28] Correspondingly, the conversion of zinc to zinc oxide leads to a drop in the equilibrium potential of the anode, based on the Nernst equation of the zinc half-cell, and causes the open-circuit potential to fall well below 1.5 V. This effect was observed for all electrode sizes and was pronounced at electrode sizes under 1 mm², where open-circuit lifetimes of less than 24 hours were measured.

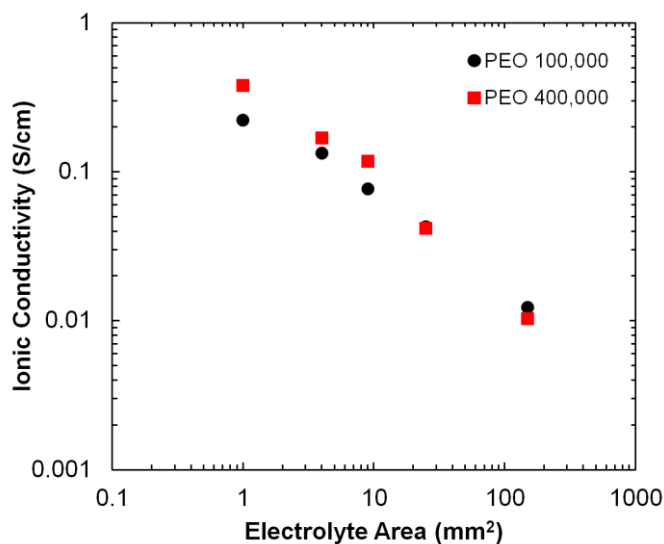


Figure 2.9: Ionic conductivity for sol-gel separators ranging from 1–150 mm² in area.

Figure 2.10b-d compares the surface morphology of Zn electrodes under different corrosion conditions. Figure 3b shows a top-down view of the printed Zn electrode before exposure to the sol-gel separator and electrolyte. Figure 3c and 3d show a 25 mm² and a 0.25 mm² printed Zn electrode, respectively, after contact with the sol-gel separator and electrolyte for 24 hours. The 25 mm² Zn electrode displays characteristic zinc hydroxide precipitation, as evidenced by the needle-like growth on the Zn particles.^[29–32] Based on a dissolution-precipitation model of Zn corrosion, as discussed by Bockelmann *et. al.*, the 25 mm² Zn electrode likely experiences type 1 corrosion, where the precipitated layer does not cover the entire electrode surface and the anodic reaction continues throughout the porous electrode.^[33] In contrast, the 0.25 mm² electrode exhibits a zinc oxide passivation layer forming at the surface, as evidenced by the areas of brighter contrast over the entire electrode. This is characteristic of type 2 corrosion, where a dense zinc oxide layer covers and passivates the electrode surface, resulting in a sudden drop in electrode potential.^[34–36]

EDS spectra were also obtained for the 25 and 0.25 mm² electrodes, with a 1:1 Zn:O signal observed in the smaller electrode and lower oxygen signal observed in the larger electrode.

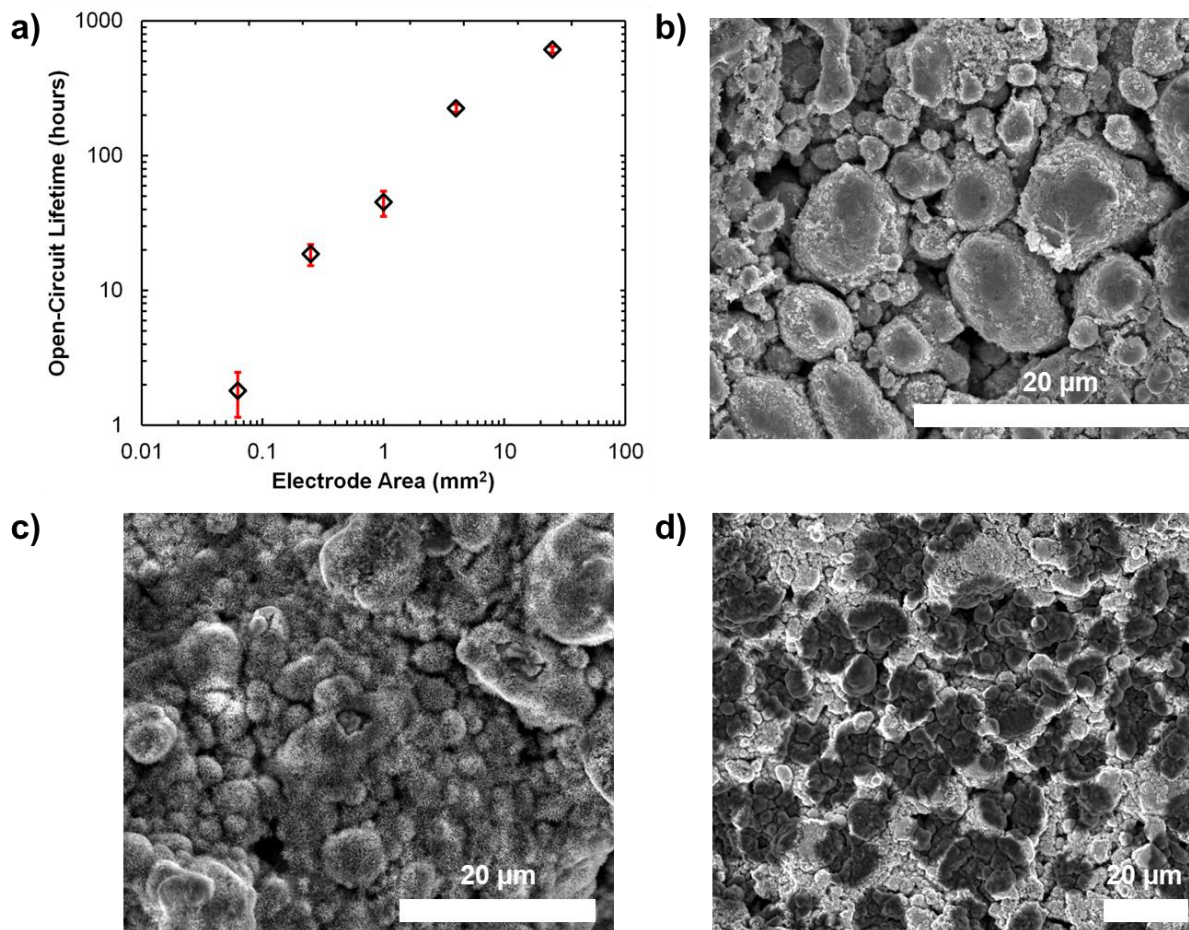


Figure 2.10: a) Open-circuit lifetime as a function of printed electrode size. Error bars show ± 1 standard deviation. b) SEM images of printed Zn electrode before exposure to electrolyte. c) 25 mm² Zn electrode after 24 hour exposure to sol-gel separator and electrolyte. d) 0.25 mm² Zn electrode after 24 hour exposure to sol-gel separator and electrolyte. All scale bars are 20 μm .

Chapter 4 will explore whether the corrosion rate is dependent on electrode size and how reactions at the Zn-electrolyte interface influence charge transfer. For this study, electrodes with 1, 4, and 25 mm² active areas demonstrated suitable and consistent lifetimes (> 24 hours) such that performance testing could be conducted. Furthermore, these electrode sizes are compatible with IoT device goals of sub-cm² active areas and are considerably smaller than previously reported printed battery geometries.

2.4 Battery Performance

For successful integration of printed batteries with IoT devices, sub-cm² printed batteries must exhibit power densities above 10 mW cm⁻² at peak operating currents of at least 1 mA cm⁻².^[21] To evaluate cell performance as a function of electrode size, full cells were printed with 1, 4, and 25 mm² electrodes (all 125 μm thickness). Multiple cells were fabricated at each electrode size

and discharged at current densities ranging from 1 – 12 mA cm⁻². Discharge experiments were conducted using a BST8-MA from MTI Corp and cells were initialized at 10 μA cm⁻² for 1 min prior to discharge. Figure 2.11a shows that the operating voltage decays slightly with increasing current density but remains above 1.4 V over the entire current density range, which is well above the required input voltage for most IoT devices. As evidenced in Figure 2.11b, the printed batteries provide similar power density regardless of electrode size, indicating that the printed Zn-Ag₂O batteries can be tailored to various wafer-level or chip-scale packaging requirements while maintaining consistent performance. The highest power density observed was 17 mW cm⁻², which is well above the maximum power requirements for most low-power IoT devices. In addition, small variations in operating voltage and power density were observed across all electrode sizes and current densities measured, with standard deviations less than 30 mV and 1 mW cm⁻² respectively. This indicates excellent reproducibility of the printed batteries and good electrochemical stability across a wide current density range.

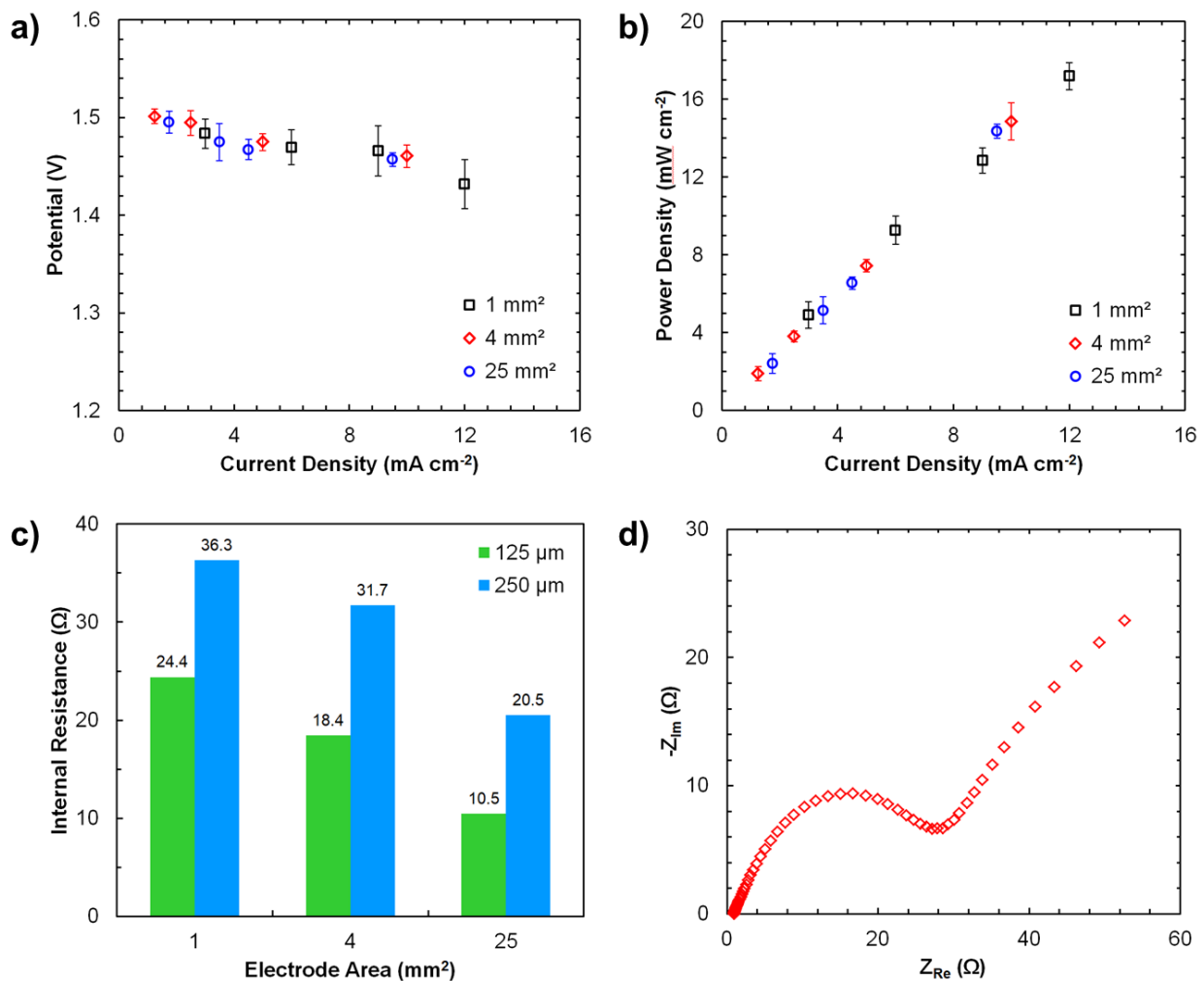


Figure 2.11: a) Polarization curve for 1, 4, and 25 mm² printed electrodes and b) corresponding power densities from 1–12 mA cm⁻². Error bars show ±1 S.D. c) Internal resistance for each printed electrode configuration. d) Example impedance plot of a fully-printed Zn-Ag₂O battery.

In addition to evaluating peak performance, electrochemical impedance spectroscopy was performed using a Gamry Reference 600 to characterize the effect of electrode geometry on internal resistance. The internal resistance, defined as the sum of the ionic and charge transfer resistances, was measured using a two electrode setup with frequencies ranging from 10^6 to 0.1 Hz with an amplitude of 10 mV. The impedance curves were fitted using a Randles cell model where the charge transfer term included both the anode and cathode. Cells with electrode areas of 1, 4, and 25 mm² and electrode thicknesses of both 125 and 250 μ m were constructed and measured. As shown in Figure 2.11c, internal resistance was found to decrease with increasing electrode area and decreasing electrode thickness. Overall, the internal resistance was less than 40 Ω for all electrode conditions, which is suitable for most integrated electronic applications. Furthermore, our results confirm that the printed batteries can be specifically tailored to a range of device requirements since the internal resistance can be lowered by decreasing the electrode thickness. For example, the internal resistance was measured to be as low as 10.5 Ω for the 25 mm², 125 μ m electrode which could be useful for high instantaneous power applications.

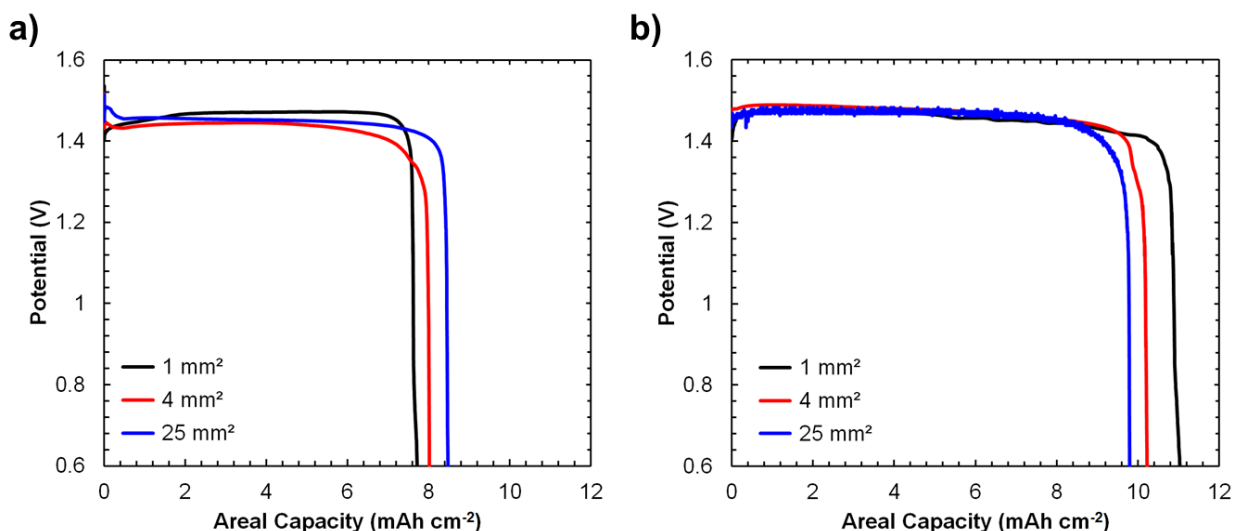


Figure 2.12: Discharge profiles for 1, 4, and 25 mm² printed electrodes with a) 125 μ m thick electrodes and b) 250 μ m thick electrodes.

Finally, fully-printed cells were discharged to determine the areal capacity for each electrode size. Figure 2.12 displays the discharge profile of the printed battery with the highest areal capacity for each cell configuration, showing areal capacities between 7.5 – 8.5 mAh cm⁻² for the 125 μ m electrode cells and 9.5 – 11 mAh cm⁻² for the 250 μ m electrode cells. All batteries were silver oxide limited, so the expected capacity and utilization were defined by the weight of the printed Ag₂O cathode. Similar discharge profiles with flat discharge curves and sudden voltage decay at the end of discharge were consistent across current densities ranging from 1 – 12 mA cm⁻². Average areal capacities ranged from 6 – 8 mAh cm⁻² across the electrode configurations and small variations in operating voltages (< 30 mV) were observed (Table A2.1, Appendix). Electrode utilization was typically measured between 80 and 90% of the expected cell capacity and was also found to be consistent across the same current density range. Figure 6 compares the areal capacities of our fully-printed Zn-Ag₂O battery with other printed batteries reported in the literature.^[6,7,19,20,37–41,8,9,11,12,15–18] Each literature value included in Figure 2.13 is tabulated in the

Appendix (Table A2.2). Our cell design achieves the highest reported areal capacities for a fully-printed battery to date, with 8.45 and 10.85 mAh cm⁻² for the 125 μm and 250 μm electrode thicknesses, respectively. This is approximately 50% and 94% higher than the previously reported record of 5.6 mAh cm⁻² by Gaikwad *et. al.*, but at device relevant current densities near 10 mA cm⁻² with power densities above 10 mW cm⁻².^[8] The excellent battery performance stems from the design of high-capacity electrode inks and the ability to print thick electrode films at small active areas.

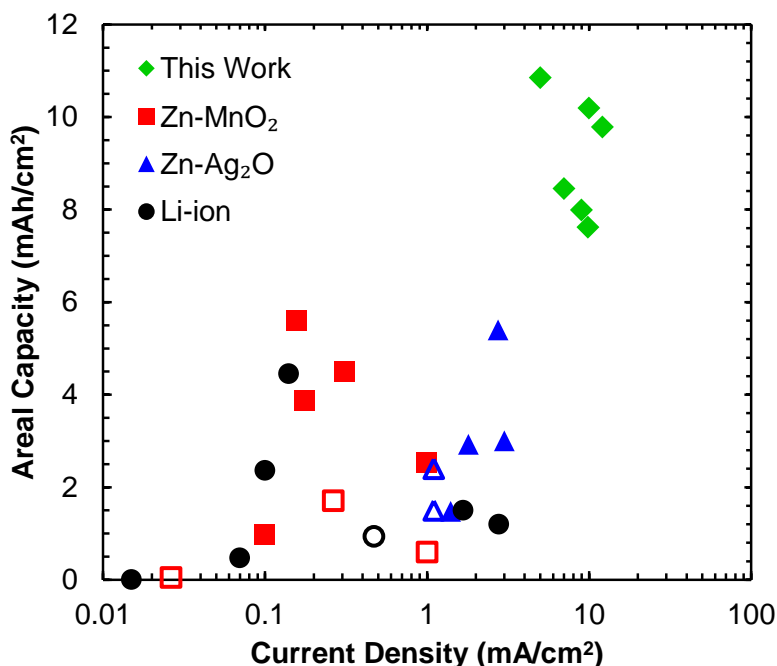


Figure 2.13: Ragone plot comparing performance of our fully-printed Zn-Ag₂O battery to reported literature values. Open symbols represent printed batteries using non-printed separators. Filled symbols represent fully-printed batteries.

2.5 Summary

In summary, this work investigated the scaling limits of a printed Zn-Ag₂O battery and demonstrated the first packaged, fully-printed battery capable of powering ubiquitous electronics with sub-cm² areas. Processed entirely in air and requiring a maximum processing temperature of only 110 °C, our printed battery design can be easily integrated in process designs for CMOS architectures via wafer-level or chip-scale packaging. Printed bilayer current collectors were implemented to ensure substrate adhesion in the presence of KOH while maintaining low resistivity (<3 Ω □⁻¹). Electrode inks were designed with high mass loadings to achieve thick electrode films and low internal resistances (< 40 Ω) in the vertical battery stack. Sol-gel separators were engineered to have smaller pores to prevent electrical shorts via Ag₂O migration without the need for nonprinted barrier layers. Encapsulation was also utilized to maintain high ionic conductivity across the sol-gel separator and prevent electrolyte dehydration. Finally, fully-printed cells were fabricated with vertical geometries and active areas as small as 1 mm². With steady operating voltages (> 1.4 V), areal capacities as high as 11 mAh cm⁻² were measured using

250 μm thick electrodes, the highest reported areal capacity for a fully-printed battery to date. Peak power densities as high as 17 mW cm^{-2} were measured at 12 mA cm^{-2} , highlighting our excellent battery performance and compatibility with IoT device requirements. Overall, our work demonstrates the potential for printed batteries to power a variety of distributed electronics systems in the medical device, smart label, and wireless sensor node industries.

2.6 References

- [1] A. P. Karpinski, B. Makovetski, S. J. Russell, J. R. Serenyi, D. C. Williams, *J. Power Sources* **1999**, 80, 53.
- [2] T. B. Reddy, *Linden's Handbook of Batteries*, McGraw-Hill, New York, **2011**.
- [3] J. Kim, R. Kumar, A. J. Bandodkar, J. Wang, *Adv. Elec* **2017**, 3, 1600260.
- [4] T. J. Hinton, A. Hudson, K. Pusch, A. Lee, A. W. Feinberg, *ACS Biomater. Sci. Eng.* **2016**, 2, 1781.
- [5] D. B. Kolesky, R. L. Truby, A. S. Gladman, T. A. Busbee, K. A. Homan, J. A. Lewis, *Adv. Mater.* **2014**, 26, 3124.
- [6] C. C. Ho, J. W. Evans, P. K. Wright, *J. Micromech. Microeng.* **2010**, 20, 104009.
- [7] K. Sun, T. Wei, B. Y. Ahn, J. Y. Seo, S. J. Dillon, J. A. Lewis, *Adv. Mater.* **2013**, 25, 4539.
- [8] A. M. Gaikwad, G. L. Whiting, D. A. Steingart, A. C. Arias, *Adv. Mater.* **2011**, 23, 3251.
- [9] A. M. Gaikwad, A. M. Zamarayeva, J. Rousseau, H. Chu, I. Derin, D. A. Steingart, *Adv. Mater.* **2012**, 24, 5071.
- [10] A. M. Gaikwad, H. N. Chu, R. Qeraj, A. M. Zamarayeva, D. A. Steingart, *Energy Technol.* **2013**, 1, 177.
- [11] K. Braam, V. Subramanian, *Adv. Mater.* **2014**, 27, 689.
- [12] G. A. Ghiurcan, C. Liu, A. Webber, F. H. Feddrix, *J. Electrochem. Soc.* **2003**, 150, 922.
- [13] K. R. Williams, R. S. Muller, *J. Microelectromechanical Syst.* **1996**, 5, 256.
- [14] K. R. Williams, K. Gupta, M. Wasilik, *J. Microelectromechanical Syst.* **2003**, 12, 761.
- [15] E. Madej, M. Espig, R. R. Baumann, W. Schuhmann, F. La Mantia, *J. Power Sources* **2014**, 261, 356.
- [16] C. C. Ho, K. Murata, D. A. Steingart, J. W. Evans, P. K. Wright, *J. Micromech. Microeng.* **2009**, 19, 094013.
- [17] A. M. Gaikwad, B. V. Khau, G. Davies, B. Hertzberg, D. A. Steingart, A. C. Arias, *Adv. Energy Mater.* **2015**, 5, 1401389.
- [18] S. Berchmans, A. J. Bandodkar, W. Jia, J. Ram, Y. S. Meng, J. Wang, *J. Mater. Chem. A* **2014**, 2, 15788.
- [19] K. T. Braam, S. K. Volkman, V. Subramanian, *J. Power Sources* **2012**, 199, 367.
- [20] R. Kumar, J. Shin, L. Yin, J. You, Y. S. Meng, J. Wang, *Adv. Energy Mater.* **2017**, 7, 1602096.
- [21] J. Carballo, W. Chan, A. B. Kahng, M. Kakimoto, S. Nath, T. Saito, K. Seto, G. Smith, I. Yamamoto, in *Int. Technol. Roadmap Semicond. 2.0*, **2015**.
- [22] K. Suganuma, *Introduction to Printed Electronics*, Springer, New York, **2014**.
- [23] R. J. Horwood, *Electrocompon. Sci. Technol.* **1974**, 1, 129.
- [24] J. McBreen, E. Gannon, *J. Power Sources* **1985**, 15, 169.
- [25] J. W. Gallaway, A. M. Gaikwad, B. Hertzberg, C. K. Erdonmez, Y. C. K. Chen-Wiegart, L. A. Sviridov, K. Evans-Lutterodt, J. Wang, S. Banerjee, D. A. Steingart, *J. Electrochem. Soc.* **2014**, 161, A275.
- [26] M. Yano, S. Fujitani, K. Nishio, Y. Akai, M. Kurimura, *J. Power Sources* **1998**, 74, 129.
- [27] A. G. Lee, C. P. Arena, D. J. Beebe, S. P. Palecek, *Biomacromolecules* **2010**, 11, 3316.
- [28] X. Zhang, *Corrosion and Electrochemistry of Zinc*, Springer, New York, **1996**.
- [29] J. O. M. Bockris, Z. Nagy, D. Drazic, *J. Electrochem. Soc.* **1973**, 120, 30.
- [30] S. Szpak, C. J. Gabriel, *J. Electrochem. Soc.* **1979**, 126, 1914.

- [31] H. Kim, E. Kim, S. Kim, H.-C. Shin, *J. Appl. Electrochem.* **2015**, *45*, 335.
- [32] E. Faegh, T. Omasta, M. Hull, S. Ferrin, S. Shrestha, J. Lechman, D. Bolintineanu, M. Zuraw, W. E. Mustain, *J. Electrochem. Soc.* **2018**, *165*, 2528.
- [33] M. Bockelmann, L. Reining, U. Kunz, T. Turek, *Electrochim. Acta* **2017**, *237*, 276.
- [34] W. Hong, Z. Jia, B. Wang, *J. Appl. Electrochem.* **2016**, *46*, 1085.
- [35] K. Huber, *J. Electrochem. Soc.* **1953**, *100*, 376.
- [36] D. D. Macdonald, K. M. Ismail, E. Sikora, *J. Electrochem. Soc.* **1998**, *145*, 3141.
- [37] H. Kim, J. Proell, R. Kohler, W. Pfleging, A. Pique, *J. Laser Micro/Nanoengineering* **2012**, *7*, 320.
- [38] T. Wei, B. Y. Ahn, J. Grotto, J. A. Lewis, *Adv. Mater.* **2018**, *30*, 1703027.
- [39] W. Lao-atiman, T. Julaphatachote, P. Boonmongkolras, S. Kheawhom, *J. Electrochem. Soc.* **2017**, *164*, 859.
- [40] M. Cheng, Y. Jiang, W. Yao, Y. Yuan, R. Deivanayagam, T. Foroozan, Z. Huang, B. Song, R. Rojaee, T. Shokuhfar, Y. Pan, J. Lu, R. Shahbazian-yassar, *Adv. Mater.* **2018**, *1800615*, 1.
- [41] Q. Chen, R. Xu, Z. He, K. Zhao, L. Pan, *J. Electrochem. Soc.* **2017**, *164*, 1852.

2.7 Appendix

Table A2.1: Summary of printed battery discharge data for all electrode configurations.

Electrode Area [mm ²]	Electrode Thickness [μm]	Average Areal Capacity [mAh cm ⁻²]	Average Operating Voltage [V]
1	125	6.05 ± 1.58	1.478 ± 0.020
1	250	6.28 ± 3.26	1.450 ± 0.017
4	125	7.10 ± 1.69	1.483 ± 0.026
4	250	7.44 ± 1.88	1.462 ± 0.029
25	125	6.93 ± 1.44	1.492 ± 0.017
25	250	7.74 ± 1.20	1.475 ± 0.016

Table A2.2: Summary of printed battery literature and comparison to our fully-printed battery design.

Battery Chemistry	Reference Number	Architecture	Printing Method	Current Density [mA cm ⁻²]	Areal Capacity [mAh cm ⁻²]	
Zn-MnO ₂	7	Vertical	3D - Direct Write	0.10	0.98	
Zn-MnO ₂	8	Vertical	Stencil (mesh-supported electrodes)	0.31	4.50	
				0.16	5.60	
Zn-MnO ₂	9	Planar	Stencil (fabric-embedded electrodes)	0.18	3.88	
Zn-MnO ₂	10	Planar	Screen (non-printed separator)	1.00	0.60	
Zn-MnO ₂	11	Planar	Screen (non-printed separator)	0.03	0.05	
				0.26	1.71	
Zn-MnO ₂	12	Vertical	Screen	1.00	2.53	
Zn-Ag ₂ O	14	Planar	Extrusion	1.80	2.93	
Zn-Ag ₂ O	15	Vertical	Stencil	2.75	5.40	
Zn-Ag ₂ O	16	Planar	Inkjet (bath electrolyte)	1.10	1.50	
				1.10	2.40	
Zn-Ag ₂ O	17	Planar	Screen	3.00	3.00	
Zn-Ag ₂ O	18	Planar	Screen	1.40	1.48	
Li-ion	19	Vertical	Doctor Blade (non-printed separator)	0.47	0.94	
Li-ion	20	Interdigitated	3D - Direct Write	1.67	1.50	
				2.78	1.20	
Li-ion	21	Vertical	Laser Direct Write	0.10	2.36	
Li-ion	22	Vertical	Stereolithography	0.015	0.0014	
Li-ion	23	Vertical	3D - Direct Write	0.14	4.45	
Li-ion	24	Interdigitated	3D - Direct Write	0.07	0.47	
Zn-Ag ₂ O	This Work	Vertical	Stencil (250 μm)	5.00	10.85	
				10.00	10.19	
				12.10	9.78	
			Stencil (125 μm)		7.00	8.45
					9.00	7.99
					9.85	7.62

Chapter 3: Printed Cathodes for Aqueous Metal-Air Batteries

3.1 Introduction

Developing low-cost energy storage for integrated electronics depends on the ability to increase energy and power densities while reducing materials and manufacturing costs. As a result, several emerging battery chemistries have been explored as alternatives to Zn-MnO₂, Zn-Ag₂O, and Li-ion printed batteries.^[1–6] Among these alternative chemistries, metal-air batteries are a promising solution for next-generation energy storage.

Metal-air batteries combine design features from both conventional batteries and fuel cells, featuring a solid-metal anode and a nearly infinite oxygen “fuel” source from the air that permeates through a porous cathode.^[7] Compared with other battery chemistries such as Zn-MnO₂, Zn-Ag₂O, and Li-ion, metal-air batteries offer superior theoretical energy densities since the oxygen cathode is not stored in the cell and the anode contains a high ratio of valence electrons to atomic nuclei. Metal-air batteries are divided into aqueous and non-aqueous chemistries based on the anode used and resulting electrolyte required.^[8] While both have their merits, aqueous metal-air batteries utilize low-cost, earth-abundant anode materials such as Zn, Al, and Mg and have simpler processing and packaging requirements compared to non-aqueous systems. Thus, aqueous metal-air batteries are particularly attractive for IoT device integration.

Equations 3.1–3.2 describe the half-cell reactions for an aqueous metal-air battery. Metal atoms at the anode are oxidized, releasing electrons to the external circuit. At the cathode, oxygen diffuses into the cathode and must react with both electrons from the porous cathode and water molecules from the liquid electrolyte. As a result, the oxygen reduction reaction (ORR) occurs at a triple-phase interface between the solid cathode, liquid electrolyte, and gaseous oxygen source, as shown in Figure 3.1.

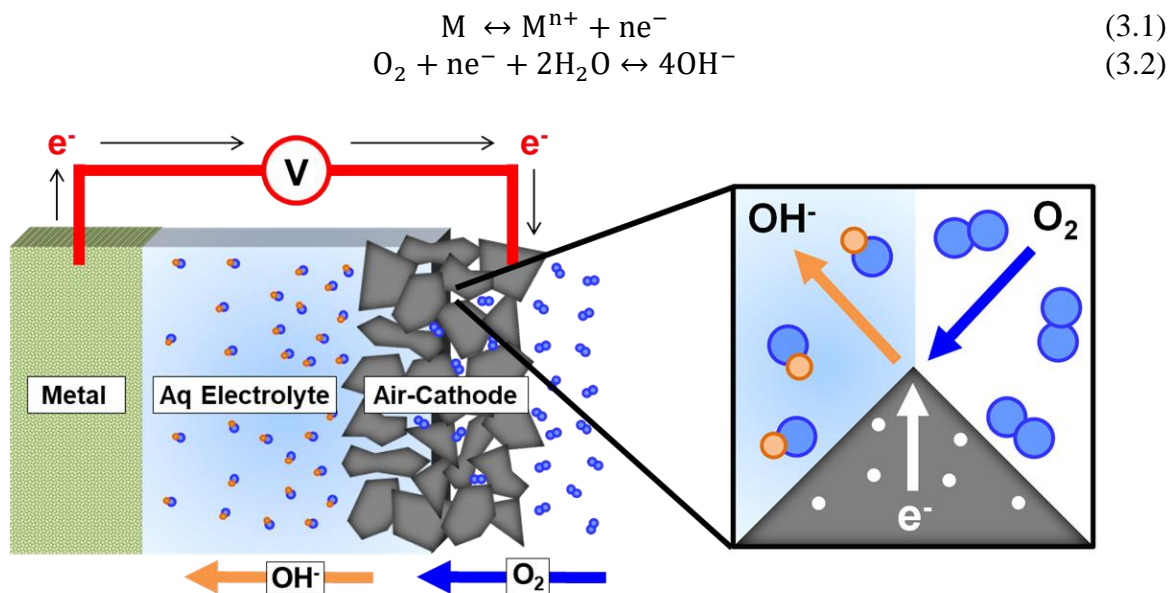


Figure 3.1: Illustration of the triple phase boundary in an aqueous metal-air battery. Oxygen, water, and electrons converge at the solid-liquid-gas interface to reduce oxygen molecules to hydroxide ions, which are carried across the electrolyte to complete the electrochemical circuit.

Aqueous metal-air battery performance hinges on the design of the air cathode since the ORR is kinetically unfavorable.^[7,9] Catalysts are typically required to facilitate this reaction in order to avoid high overpotentials, low power densities, and low discharge rate capabilities. Recent studies in non-printed metal-air batteries have introduced new catalyst materials to improve cathodic efficiency, but often rely on elevated temperatures (> 400 °C) and prolonged processing times to achieve good air cathode performance, making them unsuitable for IoT device integration via conventional semiconductor packaging flows.^[10–16] Consequently, rapid synthesis of air cathodes at low temperatures remains a significant challenge for high-throughput production of aqueous metal-air batteries.^[17]

This chapter describes the development of a printed air cathode for aqueous metal-air batteries that can be fabricated below 100 °C, enabling the possibility of using integrated metal-air batteries to power electronics. Air cathode inks are designed for stencil printing, achieving thick, porous films at low processing temperatures compatible with wafer-level and chip-scale packaging as well as many low-cost flexible plastics. Additionally, binder, solvent, and catalyst interactions are characterized to determine their influence on air cathode performance as a function of temperature. This includes *operando* pressure decay and differential electrochemical mass spectrometry (DEMS) experiments to directly measure the effects of ink design on cathodic efficiency, which to our knowledge is the first implementation of these techniques for printed air cathodes. Finally, a primary Zn-air battery with a printed anode, cathode, and separator is demonstrated, establishing record performance benchmarks for a printed battery that eclipse the areal capacities and power densities presented in Chapter 2.

3.2 Air Cathode Design and Printed Battery Architecture

In order to develop printable air cathodes, electrode inks must be carefully designed to optimize the triple-phase interface. Air cathodes require catalysts to facilitate oxygen reduction and minimize ORR overpotential for high power density batteries. Common ORR catalysts include noble metals, metal alloys, and metal oxides and are usually in the form of nanoparticles on a carbon support. The carbon support must be porous to allow oxygen diffusion to the catalyst sites and should have high surface area to increase the number of reaction sites. While permeable to air, the carbon support should be hydrophobic to prevent electrolyte flooding in the electrode, which can reduce the number of active catalytic sites.

As discussed in Section 1.4, a printable electrode ink is composed of the active material, polymeric binder, and associated solvent. While most research on aqueous metal-air batteries have focused on developing new carbon structures or catalyst materials, recent studies suggest that binder and solvent selection may have a substantial impact on cathode performance.^[18–20] In particular, polyvinylidene fluoride (PVDF), one of the most commonly used binders for battery electrodes, has been shown to have several drawbacks including poor chemical and mechanical stability.^[21–25] Thus, this work aims to identify how binder and solvent selection influence oxygen reduction in a printed metal-air cathode and determine ideal processing conditions for suitable battery performance. Specifically, we aim to achieve a low temperature, high performance air cathode for successful integration with IoT devices; so temperature effects on cathode component interactions will be closely examined.

In this study, PVDF is compared against another commonly used polymer binder, poly(tetrafluoroethylene) (PTFE). PTFE is chosen since it can be dissolved in a low boiling point

solvent such as ethanol while PVDF is typically dissolved in n-methyl-2-pyrrolidone (NMP), as shown in Figure 3.2. For the PVDF binder, a 10 wt% PVDF solution in NMP was prepared by stirring the polymer and solvent for 30 min at 750 rpm at 125 °C. For the PTFE binder, a 15 wt% PTFE solution in ethanol was prepared by stirring for 30 min at 750 rpm at room temperature. Cathode inks use a commercially available carbon powder with a Pt nanoparticle catalyst (Fuel Cell Store #591075) as a proof of concept design for the printed air cathode. Pt is chosen as the cathode catalyst due to its high oxygen reduction activity and good electrochemical stability.^[26–28] Primary cell configurations are the focus of this study due to their compatibility with several IoT systems, as discussed in Chapter 2, but future studies should explore the use of bifunctional catalyst materials for secondary metal-air batteries.

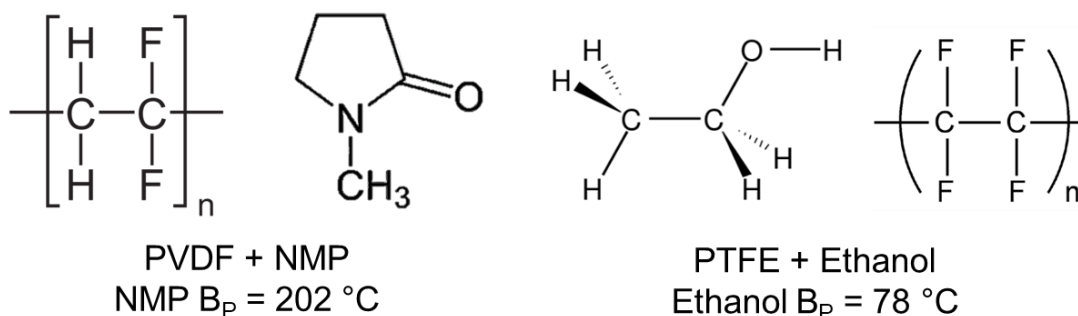


Figure 3.2: Lewis diagrams of binder and solvent materials and solvent boiling points.

Stencil printing is implemented to achieve thick, porous air cathodes with small feature sizes ($< 1 \text{ cm}^2$) to ensure IoT device compatibility. Figure 3.3a depicts the stencil printing procedure for the air cathode, where a plastic stencil is used to define the pattern, ink is dispensed into the stencil, and a doctor blade pushes the ink to fill the stencil and form the printed film. Air cathodes are printed onto porous carbon felt substrates (Fuel Cell Store #590437) using a 125 μm thick PET stencil. The carbon felt substrates, which serve as the cathodic current collector for the metal-air battery, are wet-proofed with PTFE to prevent cathode flooding from moisture in the air and limit electrolyte dehydration. For the PVDF cathode ink, the C/Pt powder was added to the PVDF binder in a 10:90 weight ratio and printed films were dried in an oven at 125 °C for 30 min and annealed in a tube furnace at either 200 or 350 °C for 30 min. For the PTFE cathode ink, the C/Pt powder was added to the PTFE binder in a 15:85 weight ratio and printed films were dried in an oven at 80 °C for 30 min and annealed at either 80 or 200 °C for an additional 30 min. These temperature conditions were chosen to demonstrate the difference between printed cathodes annealed at temperatures close to and well above the boiling point of the chosen solvents for each ink. Figures 3.3b and 3.3c show the thickness profile and morphology of a typical printed air cathode, highlighting the high porosity of the printed films to ensure high oxygen permeability to the triple-phase interface. Pt content in the cathode inks was optimized to ensure high print quality and electrode performance. Cathode inks containing C/Pt powders with 5, 20, and 30 % Pt by weight were printed to compare film homogeneity and resistivity, as shown in Figure 3.4a. Inks with 5% Pt showed the lowest resistivity, which is likely due to better carbon particle-particle contact compared to the 20 and 30% Pt films. Additionally, inks with higher Pt mass loadings displayed higher numbers of printing artifacts and slightly worse film adhesion compared to inks with lower Pt mass loadings, which may also contribute to higher resistivity in these films (Figure 3.4b and c).

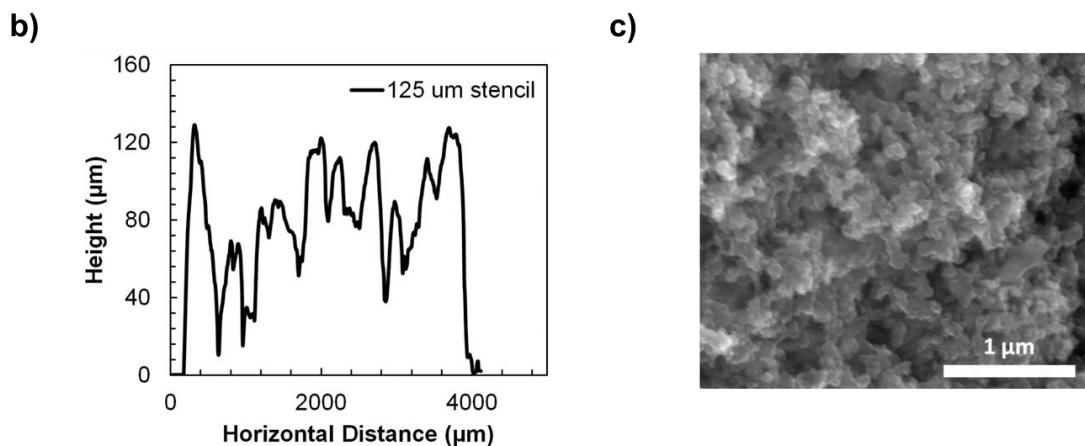
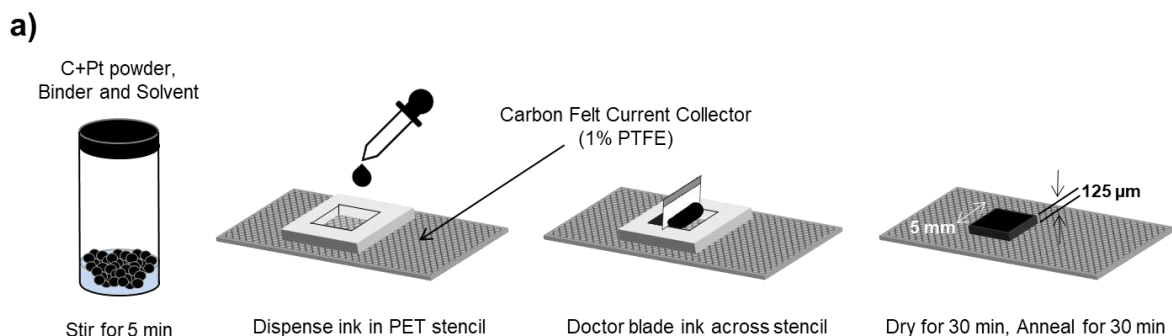


Figure 3.3: a) Schematic representation of the air cathode fabrication process. b) Typical thickness profile of a printed air cathode. c) SEM image of a printed air cathode.

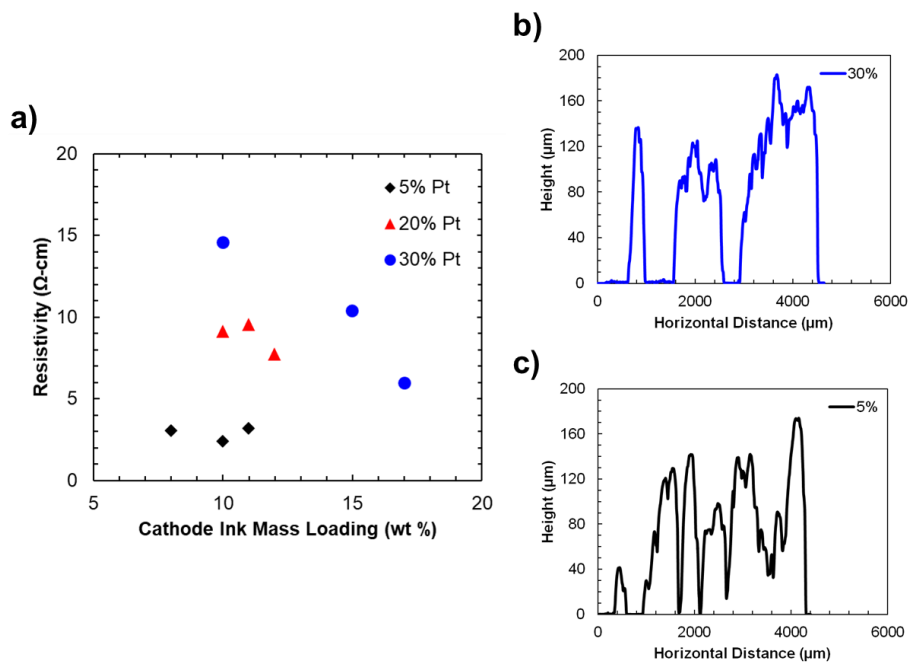


Figure 3.4: Cathode ink optimization for 5, 20, and 30 wt% Pt on C powders in a PVDF binder via a) resistivity and b-c) thickness profile scans.

Finally, printed air cathode performance is demonstrated in a printed Zn-air battery. Among aqueous metal-air chemistries, Zn-air batteries are highly promising given their low materials and processing costs and high practical energy densities (350 – 500 Wh kg⁻¹).^[8,29,30] Similar to Zn-Ag₂O cells, Zn-air batteries also offer good charge retention and maintain flat discharge profiles, which are advantageous for IoT device integration.^[31] Furthermore, Zn-air batteries can be fabricated without the use of inert environments, making them well suited for high throughput manufacturing and compatible with existing chip packaging and assembly process flows. Zn-air batteries have a theoretical open-circuit potential of about 1.65 V, but high overpotentials at the air cathode typically reduce the operating voltage to about 1.2 – 1.4 V depending on the ORR catalyst used. The half-cell and full-cell reactions for a Zn-air battery with a Pt catalyst are shown in Equations 3.3–3.5.^[7] In Chapter 2, we established a high capacity printed Zn anode and a novel sol-gel separator with high ionic conductivity that enabled a vertical battery architecture. This work utilizes these components to design a printed Zn-air battery shown in Figure 3.5. Zn anodes are stencil printed onto evaporated Cr/Au anode current collectors. The sol-gel separator is soaked with ~30 μL of a 6 M KOH electrolyte with a 1 wt% polyethylene glycol 400 additive for 10 min. The air cathode printed on the carbon felt current collector is then laminated on the anode and separator and a PDMS encapsulation ring is used to prevent electrolyte dehydration.

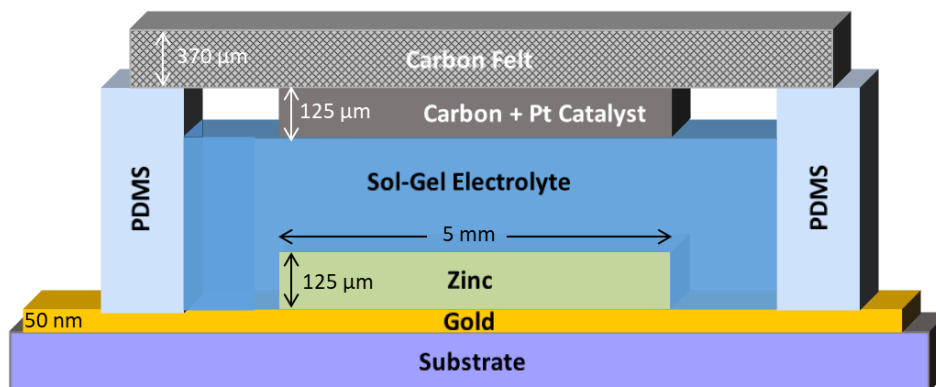


Figure 3.5: Cross-sectional schematic of the printed Zn-air battery.

3.3 Cathode Materials Characterization

Integration of metal-air batteries for IoT devices hinges on the development of air cathode processing at low temperatures to ensure system compatibility and low design costs. After printing the cathode ink, thermal treatment is necessary to achieve a suitable triple-phase boundary for oxygen reduction. This process removes excess solvent, homogenizes the printed film, and facilitates good electrical contact between adjacent particles. Previous reports suggest that temperature plays a critical role in binder stability and interactions between the binder, solvent,

and active species.^[18,22,32,33] Therefore, physical and chemical changes to the printed cathode films as a function of temperature must be carefully studied and compared to cathodic performance.

Thermogravimetric analysis (TGA) can be used to observe physical changes in battery electrodes due to various thermal events such as vaporization, absorption, and decomposition. Here, TGA is utilized to examine solvent removal from the PTFE and PVDF cathode inks. TGA experiments were conducted with a TA Instruments SDT 650 at the Stanford Soft & Hybrid Materials Facility. All experiments used a 5 °C min⁻¹ ramp rate. To confirm binder and active component stability, PTFE and PVDF binders as well as 5 wt% Pt and 20 wt% Pt on C powders were measured up to 350 °C, as shown in Figure 3.6a and 3.6b. The PTFE and PVDF binders show transitions at 55 and 140 °C respectively and remain constant at higher temperatures, indicating solvent vaporization in each binder. Full solvent removal is evident since the PTFE and PVDF binders have final relative weights that match their initial concentrations (15 and 10%). For the C/Pt powders, a constant profile is observed with a relative weight near 93%, which corresponds to the removal of adsorbed water from the powder during a bake out step before measurement. Thus, both the binders and active components in the cathode inks are stable individually up to 350 °C.

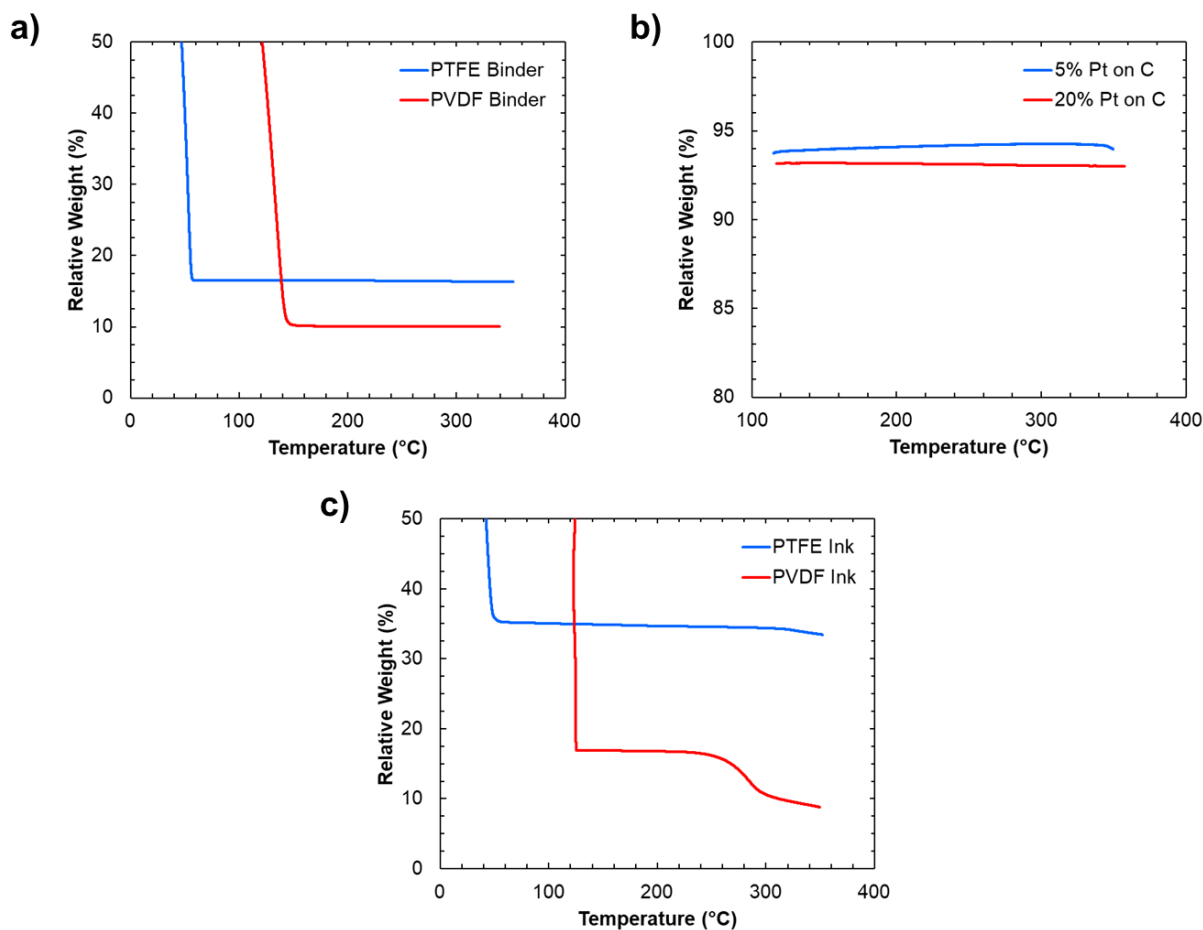


Figure 3.6: TGA profiles of a) PTFE and PVDF binders, b) C/Pt powders with 5 and 20 wt% Pt loadings, and c) PTFE and PVDF cathode inks.

Figure 3.6c shows TGA profiles of the PTFE and PVDF cathode inks with binder and active components mixed. For the PTFE ink, the system undergoes one transition at 55 °C and remains constant at higher temperatures, similar to the binder only sample and indicating ethanol vaporization. Given the PTFE ink formulation, full solvent removal should result in a final relative weight of 28%. A slightly higher value of about 34% is observed due to ethanol vaporization at room temperature before the ink was loaded into the instrument, which is expected given that ethanol has a high vapor pressure. Interestingly, the PVDF ink undergoes two transitions at about 130 and 280 °C. While the first transition is likely indicative of NMP vaporization and similar to the binder only sample, the second transition is more gradual and well above the boiling point of NMP. Furthermore, the solid loading fraction of the ink (C/Pt + polymer) before the 280 °C transition is 19%, which closely matches the expected relative weight of the PVDF ink after full solvent removal. However, at higher temperatures, the relative weight continues to decrease, with a value of about 10% at 350 °C. Thus, the interaction between the binder and C/Pt powder in the PVDF ink must contribute to some secondary physical change in the system. We suggest that PVDF may undergo a decomposition reaction catalyzed by C or Pt near 280 °C. Additionally, a small amount of NMP may be adsorbed to C or Pt sites in the cathode ink and require a higher temperature to be fully removed from the system, but likely does not solely account for the substantial weight loss observed between 250 and 350 °C (~9%).

To further investigate interactions between the cathode ink components, X-ray photoelectron spectroscopy (XPS) is used to provide chemical analysis of the printed air cathodes. XPS samples were prepared by printing 25 mm² PTFE and PVDF cathodes onto carbon felt substrates and following either the low or high temperature anneal condition outlined in Section 3.2 (200 or 350 °C for PVDF, 80 or 200 °C for PTFE). XPS data were collected using a Perkin Elmer PHI 5600 with a 2 mm Al monochromated source at 15 keV at the Berkeley Biomolecular Nanotechnology Center. Changes in the carbon and fluorine spectra are compared for both the PTFE and PVDF cathode films in Figure 3.7. As shown in Figure 3.7a, the carbon signal for the PVDF cathodes shows a strong dependence on annealing temperature. In the PVDF 200 °C sample, three distinct peaks are observed and correspond to C-C (284 eV), C-H (286 eV), and C-F (291 eV) bonds. In the PVDF 350 °C sample, the C-H and C-F peaks are reduced and the C-C peak has a higher intensity compared to the PVDF 200 °C sample. Furthermore, the fluorine signal reduces dramatically from the PVDF 200 °C to the 350 °C sample, as shown in Figure 3.7c, which further suggests PVDF decomposition at elevated temperatures. Carbon and fluorine spectra were also collected for the PTFE cathodes and showed minimal changes between the low and high temperature samples (Figures 3.7b and 3.7d).

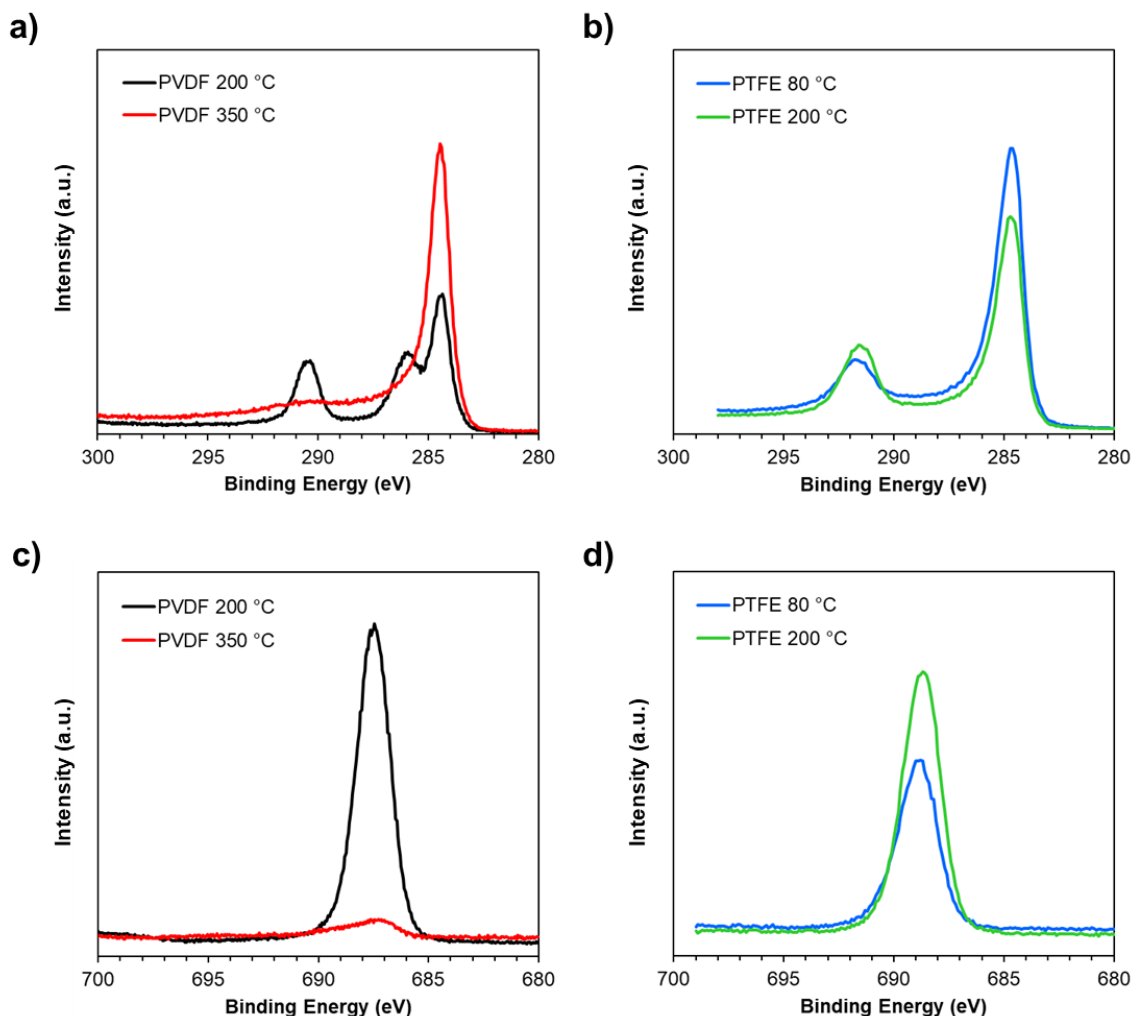


Figure 3.7: Carbon XPS spectra for printed cathodes with a) PVDF and b) PTFE binders. Fluorine XPS spectra for printed cathodes with c) PVDF and d) PTFE binders.

Additional XPS measurements were taken on the PVDF binder itself to determine if binder-solvent interactions were responsible for PVDF degradation, as shown in Figure 3.8. Samples were prepared by casting the PVDF binder on a Si substrate and following the PVDF annealing procedure outlined in Section 3.2. Clear changes to the PVDF binder are observed with increasing processing temperature from 200 to 350 °C, including increases in the C-H (286 eV) and C-F (291 eV) peak intensities, as shown in Figure 3.8a, and an increase in the fluorine peak intensity, as shown in Figure 3.8b. Finally, nitrogen spectra were also collected for the PVDF binder, as shown in Figure 3.8c, which may suggest that NMP is not fully removed from the binder at 200 °C. Overall, the PVDF binder annealed at 350 °C shows an XPS profile characteristic of pristine PVDF, which suggests that interactions between the C/Pt powder and the PVDF binder lead to the degradation of the PVDF air cathode highlighted in Figure 3.7.

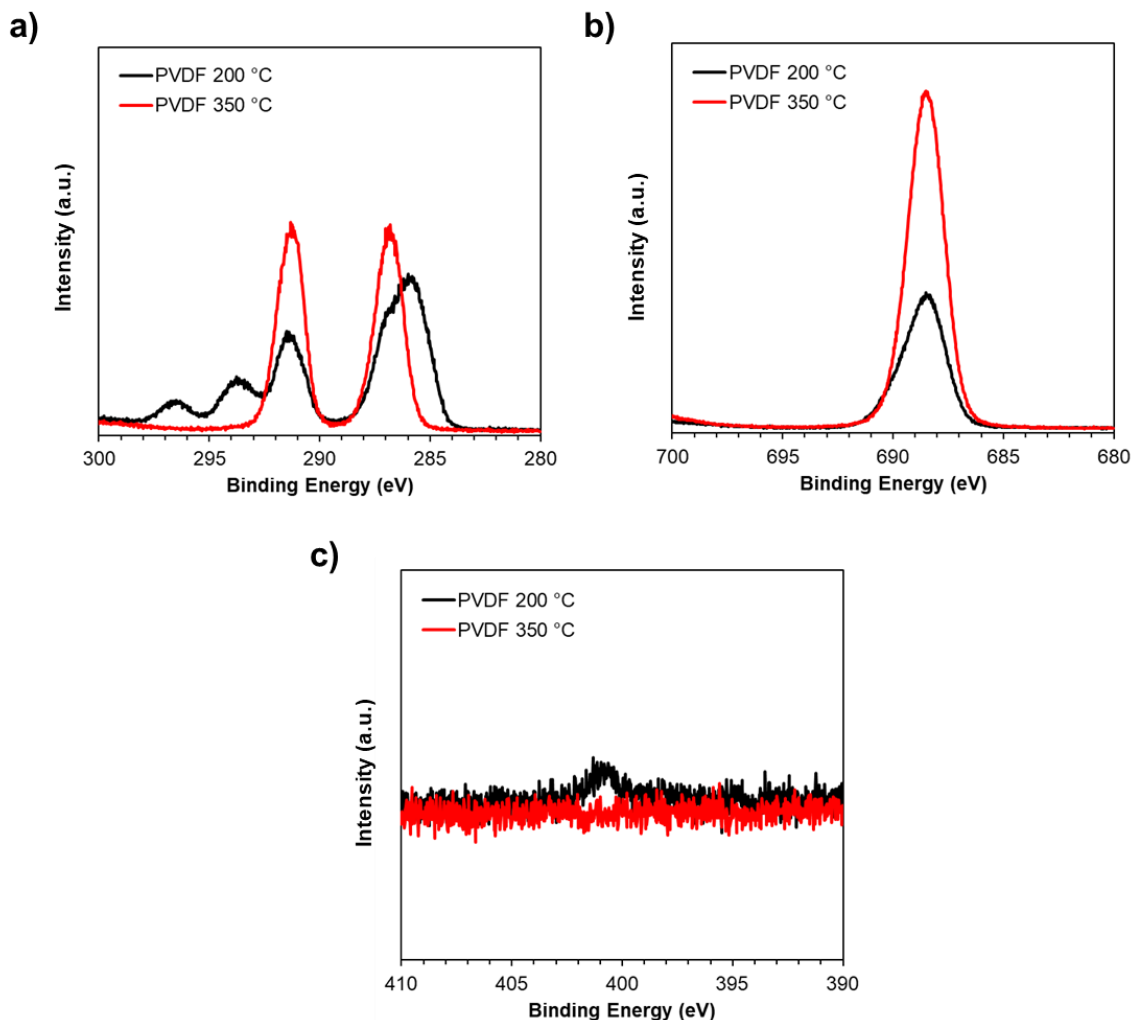


Figure 3.8: XPS spectra for PVDF binder cast on a Si substrate, showing a) carbon, b) fluorine, and c) nitrogen signals.

In summary, the TGA and XPS data show that the PVDF ink undergoes a transition near 280 °C that likely corresponds to an interaction between the C/Pt powder and the PVDF binder. Given our TGA and XPS results, we suggest that the C or Pt catalyzes PVDF degradation at and above 280 °C, which leads to additional weight loss in the PVDF ink and a reduction in fluorine signal. In contrast, the PTFE ink shows no strong interactions between the C/Pt powder and the PTFE binder and remains stable at temperatures between 80 and 200 °C. Thus, our analysis suggests that PTFE is the preferred binder for low-temperature processing of air cathode inks.

3.4 *Operando* Characterization of Printed Cathodes

Evaluating the physical and chemical changes of the printed cathode films elucidated several differences between the PTFE and PVDF inks. While these studies suggest that PVDF inks may degrade at elevated temperatures, additional studies are needed to examine the effect of cathode ink formulation and processing temperatures on metal-air battery performance and oxygen

reduction. To directly establish the impact of binder-solvent selection, we utilize *operando* electrochemical techniques to measure ORR efficiency in a printed Zn-air battery. Specifically, differential electrochemical mass spectrometry (DEMS) and *operando* pressure decay analysis are used to determine faradaic efficiency of printed Zn-air cells designed with air cathodes from PTFE and PVDF inks.

DEMS and pressure decay analysis are commonly used to quantitatively measure the production and consumption of gaseous species during electrochemical reactions.^[34–36] With high sensitivity and short detection times, these techniques can monitor electrochemical processes in real time and quantify small changes in reaction species during battery operation. DEMS and pressure decay analysis have recently been utilized in other non-aqueous metal-air battery chemistries to understand complex reaction mechanisms and evaluate battery performance.^[19,37–39] These studies couple coulometry measurements (typically galvanostatic charge and discharge) with gas consumption and evolution data and compare the results to expected electrochemical reactions. Thus, DEMS and pressure decay measurements provide insight to the faradaic processes occurring in electrochemical reactions and can be used to approximate faradaic efficiency in metal-air batteries.

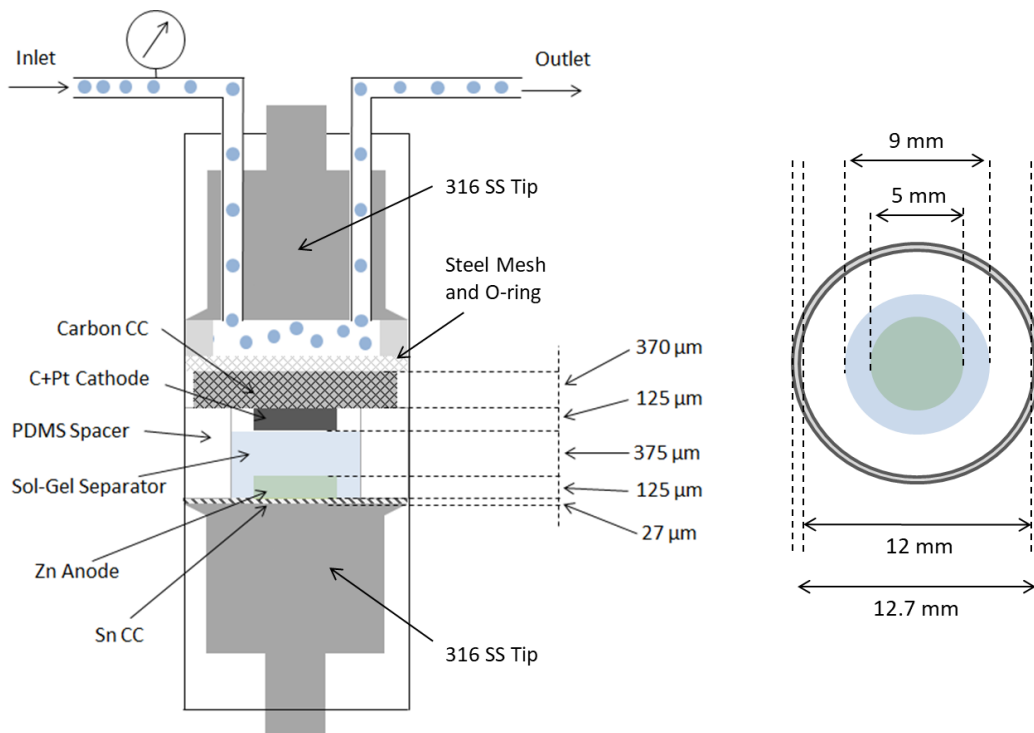


Figure 3.9: Schematic of Swagelok cell design for pressure decay and DEMS measurements.

To perform DEMS and pressure decay experiments, a custom-built cell was developed based on a modified Swagelok cell design to ensure high hermetic integrity for accurate pressure and mass spectrometry analysis.^[19,40] As shown in Figure 3.9, a fused silica tube is sealed against 1/2" stainless steel current collectors (McMaster-Carr) with compressed ethylene-propylene (EP) o-rings. Tin foil (Sigma #356948) is used as the anodic current collector and is cut into 12 mm diameter circles. The Zn-air battery is printed using the same procedure as the standard cell design

discussed in Section 3.2 with a circular electrode geometry. The Zn anode is printed directly onto the anode current collector and the sol-gel separator and air cathode are printed vertically to ensure a minimal separation between the anode and cathode. Using PDMS encapsulation, a stainless steel mesh and ring spacer are placed on top of the cathode to define the volume of the gas headspace, which was approximately 2100 μL for each cell, including the inlet and outlet capillaries. All electrochemical experiments were conducted under pure oxygen at an initial pressure of ~ 1100 torr. Ambient temperature was also measured throughout each experiment to account for temperature dependent fluctuations in headspace pressure. Galvanostatic discharge measurements for pressure-decay analysis were conducted using a Bio-Logic VSP Potentiostat. All pulse experiments (Figure 3.11) were performed with alternating open-circuit and discharge periods for 5 min each. All discharge experiments (Figure 3.10 and Figure 3.12) were discharged until a 0.2 V cutoff potential was reached and were initialized at $10 \mu\text{A cm}^{-2}$ for 1 min prior to discharge.

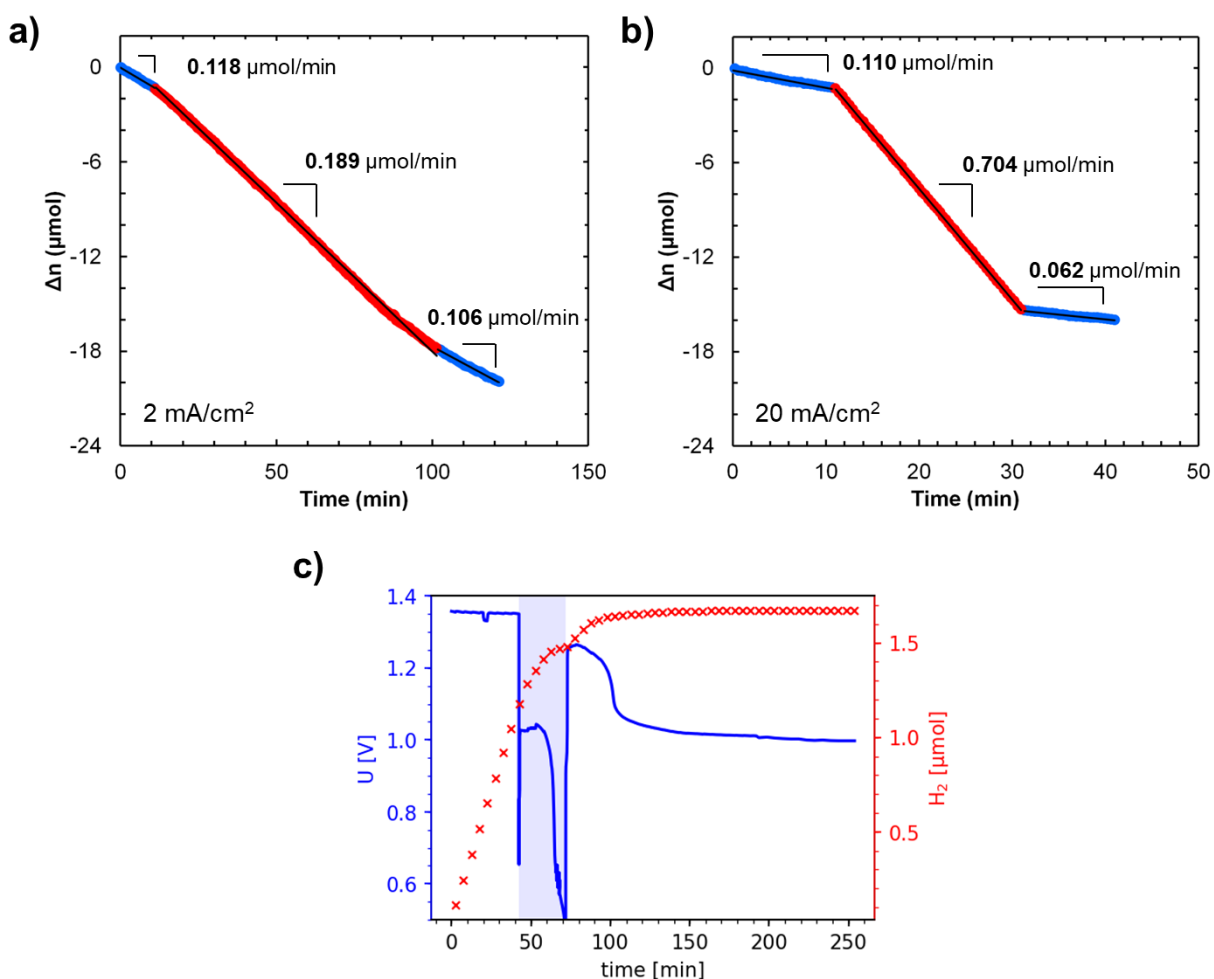


Figure 3.10: Example of a pressure decay profile of a Zn-air battery discharged at a) 2 mA cm^{-2} and b) 20 mA cm^{-2} . Both cells shown use a PTFE 200 cathode and are discharged to 0.5 V (red regions) with an open-circuit hold (blue region) before and after discharge. C) DEMS data for a Zn-air battery (PTFE 200 cathode) showing hydrogen evolution from the Zn anode at open-circuit conditions (white highlight) and under discharge (blue highlight, 20 mA cm^{-2}).

In order to compare the faradaic efficiencies of the PTFE and PVDF printed cathodes, galvanostatic (constant current) discharge experiments were performed in the pressure decay cell. As shown in Equation 3.3, ORR in a Zn-air battery with a Pt catalyst requires 4 electrons per oxygen molecule consumed, so the oxygen consumption rates for each printed cathode were compared against this process. Figure 3.10a-b show an example of oxygen consumption data for printed Zn-air batteries discharged at 2 and 20 mA cm⁻². The red regions indicate cell discharge and the blue regions indicate open-circuit conditions before and after discharge. Here, oxygen consumption was observed at both discharge and open-circuit conditions, as indicated by the negative slope. This effect is caused by Zn corrosion in the printed Zn-air battery and is an artifact of the experimental setup. Because Zn has a reduction potential more negative than water, the hydrogen evolution reaction (HER) occurs at the Zn-electrolyte interface (further details in Chapter 4). Evolution of hydrogen in the printed Zn-air battery is confirmed using DEMS, as shown in Figure 3.10c. In our system, evolved hydrogen can diffuse through the separator and react with pure oxygen at Pt catalyst sites in the porous cathode to produce water. Thus, two oxygen consumption processes are observed in the pressure-decay cell: one due to Zn corrosion and one due to ORR during discharge.

Oxygen consumption due to ORR must be isolated in order to calculate true faradic efficiencies, so the amount of oxygen consumption due to Zn corrosion must be subtracted from the total amount of oxygen consumption observed. To determine the rate of oxygen consumption due to Zn corrosion, pulsed discharge experiments were conducted on the Zn-air batteries. Figure 3.11a-b shows an example of a pulsed Zn-air battery experiment, with alternating discharge and open-circuit intervals. The slope of the blue open-circuit regions remains constant before and after each discharge pulse, indicating that oxygen consumption due to corrosion is independent of discharge rate. This result was verified by conducting multiple pulsed discharge experiments for each cathode condition, which showed that oxygen consumption rate due to corrosion was consistent and independent of cathode formulation, averaging 0.153 μmol min⁻¹ with a 5% standard deviation (0.008 μmol min⁻¹). The pulse discharge experiments were also conducted where the current density was varied randomly between discharge pulses, which also showed that oxygen consumption due to corrosion was constant.

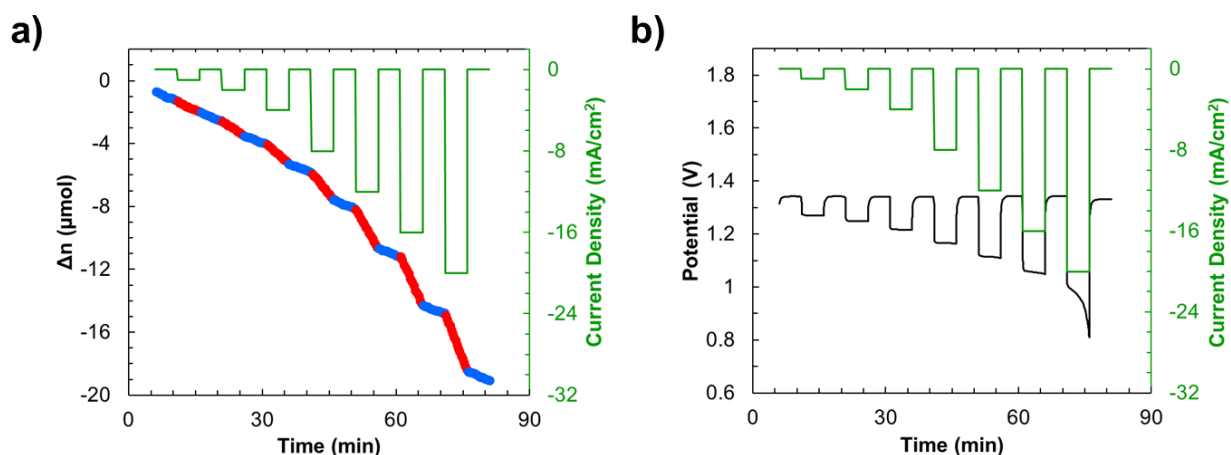


Figure 3.11: a) Pressure decay and b) electrochemical data from pulsed discharge of a Zn-air battery with a PTFE 80 air cathode, highlighting the comparison between discharge (red regions) and open-circuit (blue regions) conditions.

However, the reader should note that oxygen consumption due to corrosion changes as the battery approaches a high depth of discharge where the cell potential rapidly falls (also termed the sudden death region). In this region, the open-circuit oxygen consumption rate typically decreased, but the exact profile varied from cell to cell. This variation is caused by Zn conversion to ZnO and the non-equilibrium state of the Zn-electrolyte interface. ZnO precipitates cause a passivation of the electrode surface that corresponds to a sudden drop in the open-circuit potential of the cell, as shown in the black line in Figure 3.11b. The passivated Zn surface limits further hydrogen evolution at the anode and thus changes the rate of oxygen consumption at open-circuit. This was confirmed via DEMS, as shown in Figure 3.10c, where the slope of the evolved hydrogen over time decreases towards the end of cell discharge. The hydrogen rate increases after the cell potential increases (more Zn surface sites available) and then decreases again after the open-circuit potential falls from about 1.2 to 1.0 V. This process will be further explained in Chapter 4, but for this analysis, oxygen consumption due to corrosion was calculated only during normal battery operation (stable open-circuit voltage before sudden death region).

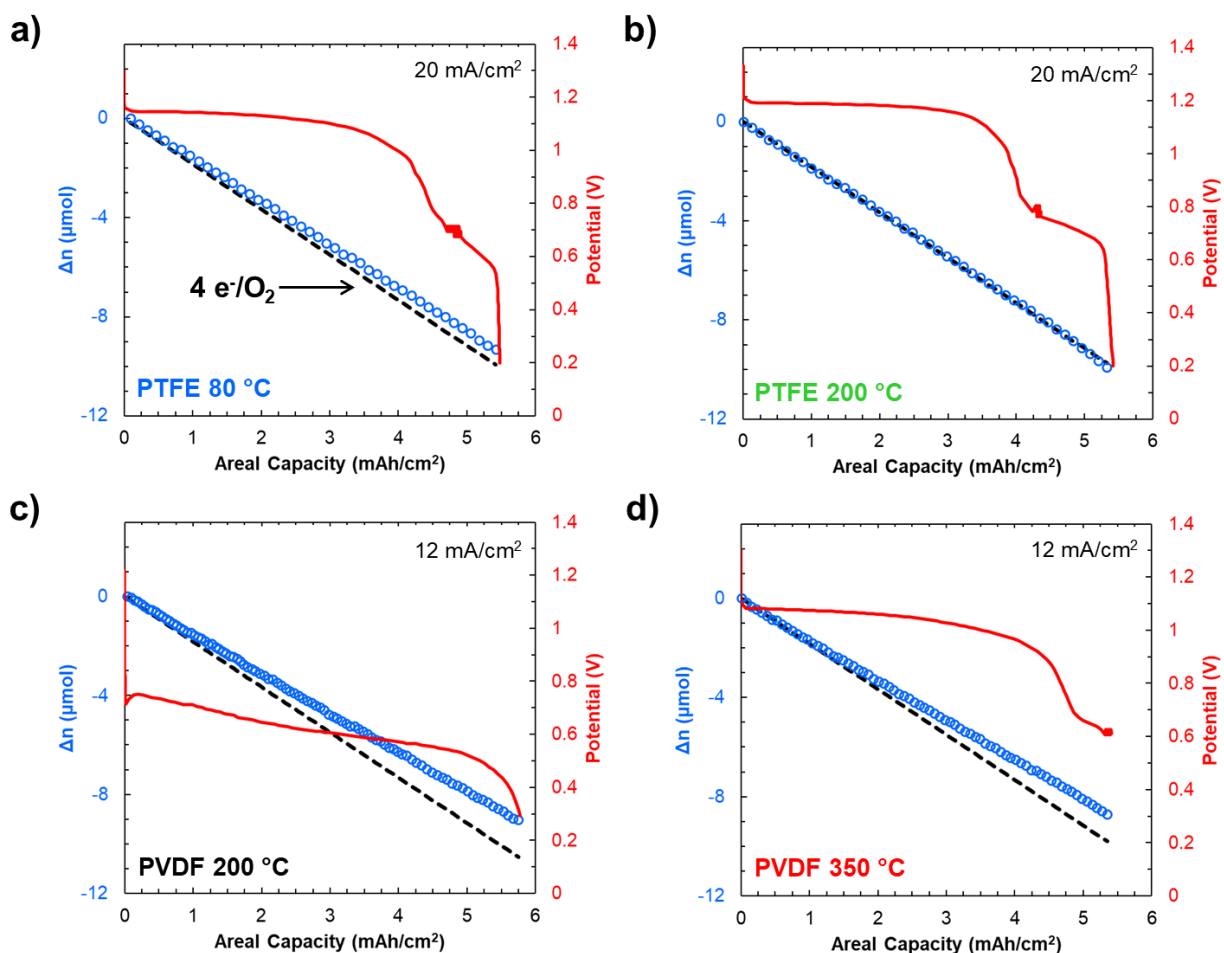


Figure 3.12: Discharge profiles and oxygen consumption data for a) PTFE 80, b) PVDF 200, c) PTFE 200, and d) PVDF 350 air cathodes. Blue points show corrosion corrected oxygen consumption compared to theoretical oxygen reduction (dotted black line).

Using the pressure decay method, PTFE and PVDF cathodes were tested in the pressure-decay cell, as described in Figure 3.12. All batteries were fully discharged and compared to the $4 e^-/O_2$ process, as shown by the dotted line in each plot. PTFE and PVDF cells were discharged at their maximum discharge current density (as defined in Section 3.5). In Figure 3.12a-b, the PTFE 80 and 200 °C batteries show high operating potentials (> 1 V) and pressure-decay rates that closely match the $4 e^-/O_2$ process. In contrast, the PVDF 200 and 350 °C batteries shown in Figure 3.12c-d have much lower operating voltages and pressure-decay rates that deviate slightly from the $4 e^-/O_2$ process. This information is summarized in Figure 3.13 and Table 3.1, where the coulometry data are coupled with the gas consumption data to calculate a faradaic efficiency for each printed cathode configuration (where $4 e^-/O_2$ corresponds to 100% faradaic efficiency). As shown, the faradaic efficiencies of the PTFE cells are higher than for the PVDF cells and faradaic efficiency increases with increasing processing temperature. These results indicate that at high operating current densities, PTFE cathodes require fewer electrons per molecule of oxygen to facilitate ORR at the printed cathode compared to the PVDF cathodes. This is likely due to the higher overpotentials observed in the PVDF cells and is also likely related to the PVDF binder-solvent interactions discussed in Section 3.3.

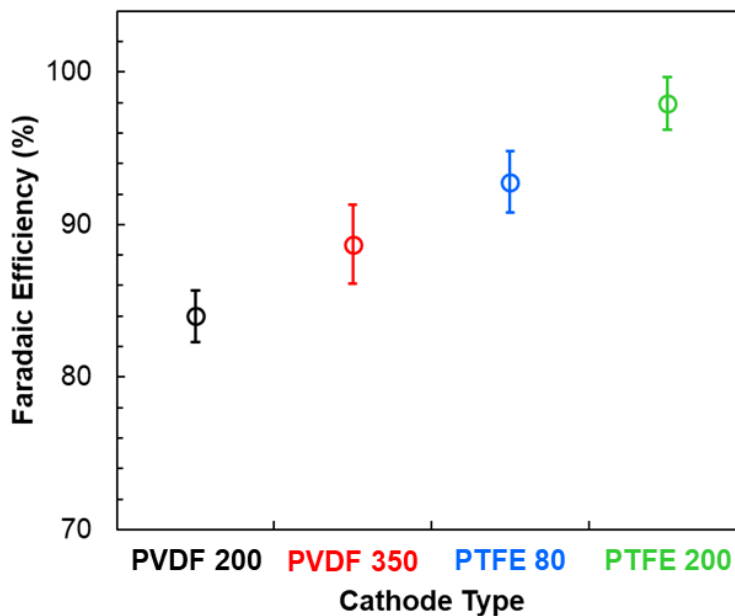


Figure 3.13: Faradic efficiency comparison between air cathode conditions.

Table 3.1: Air cathode performance data from *operando* Zn-air characterization.

Cathode Type	Current Density [mA cm ⁻²]	Average Operating Potential [V]	e^- / O_2 [$\mu\text{mol}/\mu\text{mol}$]	Faradaic Efficiency [%]
PTFE 200	20	1.192	4.09	98.0 ± 1.7
PTFE 80	20	1.139	4.31	92.8 ± 2.0
PVDF 350	12	1.062	4.51	88.7 ± 2.6
PVDF 200	12	0.683	4.76	84.0 ± 1.7

3.5 Zn-Air Battery Performance

Based on our *operando* experiments on printed Zn-air batteries, PTFE cathodes demonstrate higher performance at lower processing temperatures compared to PVDF cathodes. To validate the pressure-decay data, additional discharge experiments were conducted to evaluate Zn-air battery performance as a function of cathode ink formulation and processing temperature. Specifically, we set out to determine a maximum operating current density for each cathode condition, as this impacts IoT device functionality. The maximum current density was obtained by defining a cutoff operating voltage, which is typically 1.0 V for low-power nodes (as discussed in Sections 1.1 and 2.3). Experiments were conducted in air using a BST8-MA from MTI Corp. Cells were initialized at $10 \mu\text{A cm}^{-2}$ for 1 min prior to discharge. Since these experiments were conducted in air instead of pure oxygen, lower potentials are expected due to the lower oxygen partial pressure.

Figure 3.14 shows polarization measurements for the cathode configurations. PTFE cells were discharged up to 32 mA cm^{-2} , whereas PVDF 350 cells could only be discharged up to 16 mA cm^{-2} . PVDF 200 cells demonstrated operating voltages near 0.6 V at 2 mA cm^{-2} and thus were not included in our comparison. PTFE 80 and 200 cathodes achieved superior power densities compared to PVDF cells based on their higher operating potentials, matching our pressure-decay observations. This confirms that cathodic overpotentials are lower in the PTFE inks compared to the PVDF inks. The highest power densities observed were 25 and 28 mW cm^{-2} for the PTFE 80 and 200 cathodes, respectively. Furthermore, our printed Zn-air batteries achieve higher power densities compared to the printed Zn- Ag_2O batteries presented in Chapter 2 (17 mW cm^{-2}). Maximum current densities of about 20 and 25 mA cm^{-2} were established for the PTFE 80 and 200 cathodes, respectively, although cells could still be discharged at higher current densities and maintain operating voltages below 1 V. By comparison, PVDF 350 cells achieved a maximum current density of only 4 mA cm^{-2} . Compared to previous reports of printed Zn-air batteries^[5,6], our PTFE cathode design achieves significantly higher power densities ($\sim 0.25 \text{ mW cm}^{-2}$) with much higher operating voltages (0.877 V).

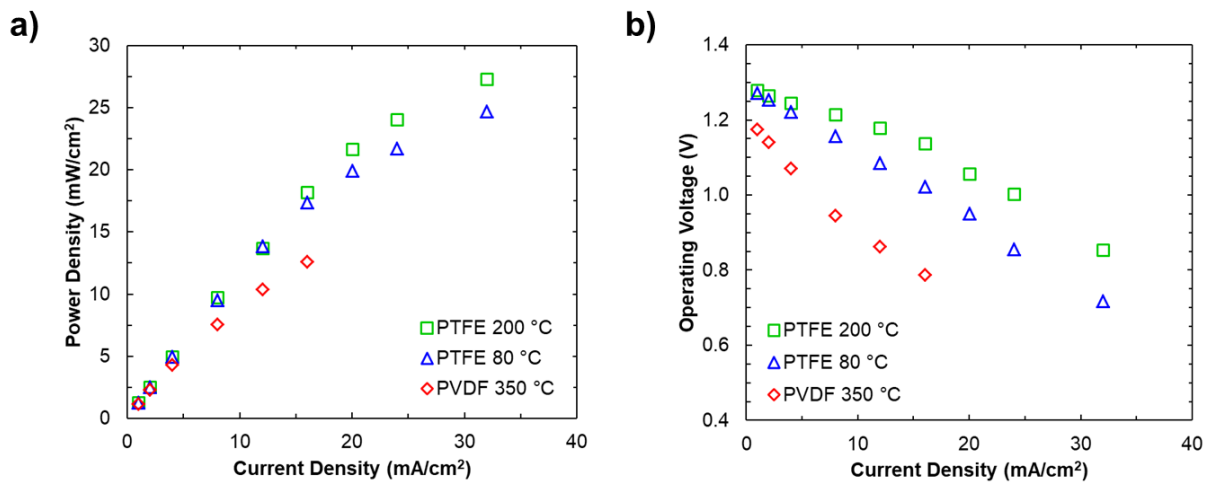


Figure 3.14: Polarization data showing the a) power density and b) operating voltage of the PTFE 80, PTFE 200, and PVDF 350 air cathodes.

Additional tests were conducted to optimize the ink formulation conditions, namely the Pt catalyst concentration and the binder-solvent ratio. As shown in Figure 3.15a, Zn-air batteries with 5, 20, and 30% Pt by weight in the Pt/C precursor were discharged at current densities between 1 – 16 mA cm⁻². A 10 wt% PVDF binder was used for these experiments. Pt concentration had little effect on the overall power density of the cell, so the 5 wt% Pt precursor was confirmed to be suitable for Zn-air battery fabrication. In Figure 3.16b, Zn-air batteries with 10 and 15% PTFE by weight in the polymer binder were discharged from 1 – 32 mA cm⁻². Again, polymer binder content was not shown to have a strong interaction on the overall performance of the battery, so 15 wt% PTFE was chosen for the polymer binder concentration.

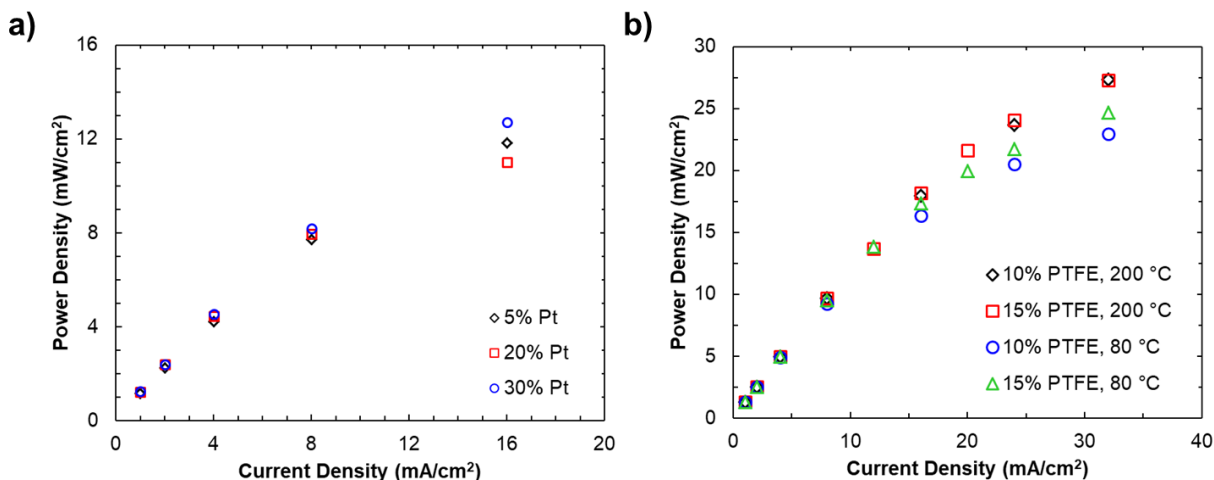


Figure 3.15: Polarization data showing the comparison between a) Pt concentration in the Pt/C precursor and b) PTFE content in the polymer binder.

Finally, Zn-air batteries with PTFE 80 cathodes were discharged between 2 – 20 mA cm⁻² to determine their areal capacity. Figure 3.16 shows these results, with a maximum areal capacity of 12 mAh cm⁻² observed and operating voltages well above 1 V for the entire current density range. This demonstrates the first printed Zn-air battery processed entirely below 100 °C, a crucial step towards low-temperature synthesis of metal-air batteries capable of powering integrated electronic devices. Furthermore, to the best of our knowledge, the printed Zn-air design achieves the highest reported power density and areal capacity for a printed battery to date, as this battery beats the previously reported record of 17 mW cm⁻² and 11 mAh cm⁻² (Chapter 2). However, the observed areal capacity only corresponds about 10% Zn utilization, which indicates that most of the Zn anode is isolated during discharge due to Zn corrosion. This issue will be further discussed in Chapter 4, where *operando* characterization techniques can be further utilized to monitor Zn corrosion in real time.

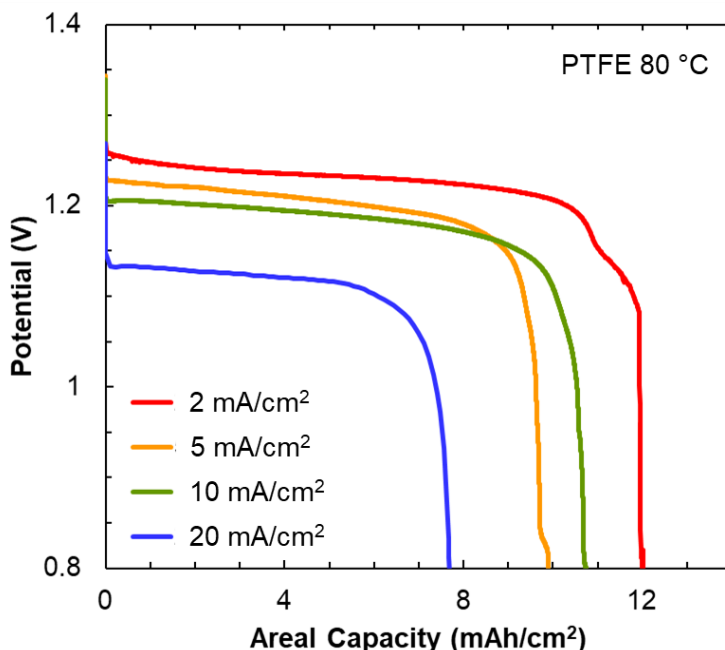


Figure 3.16: Discharge profiles for printed Zn-air batteries with a PTFE 80 air cathode.

3.6 Summary

In summary, this work demonstrated a printable air cathode processed entirely below 100 °C, a critical step towards high-throughput production of metal-air batteries. Printable PVDF and PTFE cathode inks were compared to determine how binder and solvent selection influence cathodic performance and dictate required processing temperatures. TGA and XPS analysis identified a phase change in the PVDF ink between 250 and 300 °C, while the PTFE ink remained stable between 80 and 350 °C. This corresponded to a critical processing temperature for PVDF inks, as the PVDF 200 cathodes displayed much higher overpotentials and lower power densities compared to PVDF 350 cathodes. *Operando* pressure decay and DEMS measurements confirmed that binder-solvent selection impacted oxygen reduction efficiency, with PVDF cathodes demonstrating faradaic efficiencies below 90% compared to the PTFE 80 and 200 cathodes at 93 and 98%, respectively. To the best of our knowledge, this is the first demonstration of *operando* pressure decay and DEMS analysis of a printed metal-air battery, and thus serves as an important electrochemical technique to evaluate future printed metal-air battery designs. Finally, printed Zn-air batteries were fabricated to test printed cathode performance in a full cell. With steady operating voltages well above 1.0 V, areal capacities as high as 12 mAh cm⁻² were measured with a PTFE 80 cathode, demonstrating the highest reported areal capacity for a printed battery to date. PTFE cathodes could be discharged at high current densities (1 – 32 mA cm⁻²) and achieved power densities as high as 28 mW cm⁻², highlighting our excellent battery performance and compatibility with peak current and power requirements for IoT devices. Overall, our work highlights the potential for rapid, low-temperature processing of metal-air batteries that can power a variety of distributed electronic devices.

3.7 References

- [1] Z. Wang, X. Meng, K. Chen, S. Mitra, *Adv. Mater. Interfaces* **2018**, *5*, 1.
- [2] C. Milroy, A. Manthiram, *Chem. Commun.* **2016**, *52*, 4282.
- [3] J. Ding, K. Shen, Z. Du, B. Li, S. Yang, *ACS Appl. Mater. Interfaces* **2017**, *9*, 41871.
- [4] H. A. Figueredo-Rodríguez, R. D. McKerracher, M. Insausti, A. G. Luis, C. P. de León, C. Alegre, V. Baglio, A. S. Aricò, F. C. Walsh, *J. Electrochem. Soc.* **2017**, *164*, A1148.
- [5] M. Hilder, B. Winther-Jensen, N. B. Clark, *J. Power Sources* **2009**, *194*, 1135.
- [6] M. Hilder, B. Winther-Jensen, N. B. Clark, *Electrochim. Acta* **2012**, *69*, 308.
- [7] F. Cheng, J. Chen, *Chem. Soc. Rev.* **2012**, *41*, 2172.
- [8] Y. Li, J. Lu, *ACS Energy Lett.* **2017**, *2*, 1370.
- [9] V. Neburchilov, H. Wang, J. J. Martin, W. Qu, *J. Power Sources* **2010**, *195*, 1271.
- [10] Y. Li, M. Gong, Y. Liang, J. Feng, J. E. Kim, H. Wang, G. Hong, B. Zhang, H. Dai, *Nat. Commun.* **2013**, *4*, 1805.
- [11] H. W. Liang, Z. Y. Wu, L. F. Chen, C. Li, S. H. Yu, *Nano Energy* **2015**, *11*, 366.
- [12] J. Park, M. Park, G. Nam, J. S. Lee, J. Cho, *Adv. Mater.* **2015**, *27*, 1396.
- [13] J. Wang, H. Wu, D. Gao, S. Miao, G. Wang, X. Bao, *Nano Energy* **2015**, *13*, 387.
- [14] Q. Liu, Y. Wang, L. Dai, J. Yao, *Adv. Mater.* **2016**, *28*, 3000.
- [15] A. Flegler, S. Hartmann, J. Settelein, K. Mandel, G. Sextl, *Electrochim. Acta* **2017**, *258*, 495.
- [16] A. Sumboja, M. Lübke, Y. Wang, T. An, Y. Zong, Z. Liu, *Adv. Energy Mater.* **2017**, *7*, 1.
- [17] F. Cheng, J. Shen, B. Peng, Y. Pan, Z. Tao, J. Chen, *Nat. Chem.* **2011**, *3*, 79.
- [18] H. Chen, M. Ling, L. Hencz, H. Y. Ling, G. Li, Z. Lin, G. Liu, S. Zhang, *Chem. Rev.* **2018**, *118*, 8936.
- [19] B. D. McCloskey, D. S. Bethune, R. M. Shelby, G. Girishkumar, A. C. Luntz, *J. Phys. Chem. Lett.* **2011**, *2*, 1161.
- [20] V. S. Bryantsev, J. Uddin, V. Giordani, W. Walker, D. Addison, G. V. Chase, *J. Electrochem. Soc.* **2013**, *160*, 160.
- [21] J. K. Papp, J. D. Forster, C. M. Burke, H. W. Kim, A. C. Luntz, R. M. Shelby, J. J. Urban, B. D. McCloskey, *J. Phys. Chem. Lett.* **2017**, *8*, 1169.
- [22] F. Wang, X. Li, *ACS Omega* **2018**, *3*, 6006.
- [23] C. C. Nguyen, T. Yoon, D. M. Seo, P. Guduru, B. L. Lucht, *ACS Appl. Mater. Interfaces* **2016**, *8*, 12211.
- [24] C. V. Amanchukwu, J. R. Harding, Y. Shao-Horn, P. T. Hammond, *Chem. Mater.* **2015**, *27*, 550.
- [25] R. Black, S. H. Oh, J. H. Lee, T. Yim, B. Adams, L. F. Nazar, *J. Am. Chem. Soc.* **2012**, *134*, 2902.
- [26] J. K. Nørskov, J. Rossmeisl, A. Logadottir, L. Lindqvist, J. R. Kitchin, T. Bligaard, H. Jónsson, *J. Phys. Chem. B* **2004**, *108*, 17886.
- [27] J. Greeley, I. E. L. Stephens, A. S. Bondarenko, T. P. Johansson, H. A. Hansen, T. F. Jaramillo, J. Rossmeisl, I. Chorkendorff, J. K. Nørskov, *Nat. Chem.* **2009**, *1*, 552.
- [28] P. Strasser, S. Koh, T. Anniyev, J. Greeley, K. More, C. Yu, Z. Liu, S. Kaya, D. Nordlund, H. Ogasawara, M. F. Toney, A. Nilsson, *Nat. Chem.* **2010**, *2*, 454.
- [29] Y. Li, H. Dai, *Chem. Soc. Rev.* **2014**, *43*, 5257.
- [30] J. S. Lee, S. T. Kim, R. Cao, N. S. Choi, M. Liu, K. T. Lee, J. Cho, *Adv. Energy Mater.* **2011**, *1*, 34.

- [31] T. B. Reddy, *Linden's Handbook of Batteries*, McGraw-Hill, New York, **2011**.
- [32] L. R. Jordan, A. K. Shukla, T. Behrsing, N. R. Avery, B. C. Muddle, M. Forsyth, *J. Power Sources* **2000**, 86, 250.
- [33] S. Gao, Y. Su, L. Bao, N. Li, L. Chen, Y. Zheng, J. Tian, J. Li, S. Chen, F. Wu, *J. Power Sources* **2015**, 298, 292.
- [34] O. Wolter, J. Heitbaum, *Phys. Chem. Chem. Phys.* **1984**, 88, 2.
- [35] C. Zhao, Y. Lu, Y. Li, L. Jiang, X. Rong, Y.-S. Hu, H. Li, L. Chen, *Small Methods* **2017**, 1, 1600063.
- [36] A. A. Abd-El-Latif, C. J. Bondue, S. Ernst, M. Hegemann, J. K. Kaul, M. Khodayari, E. Mostafa, A. Stefanova, H. Baltruschat, *Trends Anal. Chem.* **2015**, 70, 4.
- [37] B. D. McCloskey, C. M. Burke, J. E. Nichols, S. E. Renfrew, *Chem. Commun.* **2015**, 51, 12701.
- [38] C. M. Burke, R. Black, I. R. Kochetkov, V. Giordani, D. Addison, L. F. Nazar, B. D. McCloskey, *ACS Energy Lett.* **2016**, 1, 747.
- [39] J. E. Nichols, B. D. McCloskey, *J. Phys. Chem. C* **2017**, 121, 85.
- [40] S. D. Beattie, D. M. Manolescu, S. L. Blair, *J. Electrochem. Soc.* **2009**, 156, A44.

Chapter 4: Characterizing Zn Corrosion via *Operando* Techniques

4.1 Introduction

Printed Zn batteries are well suited to power a wide variety of integrated electronic applications. As discussed in Chapters 2 and 3, both Zn-Ag₂O and Zn-air chemistries have been developed and offer significant advantages over other battery chemistries given their high performance at high discharge rates and use of low-cost, earth-abundant materials with inherent air stability. Despite these significant advantages, further research is needed to address battery degradation and failure mechanisms that limit overall performance. A few of these degradation modes have already been addressed. In Chapter 2, electrolyte dehydration and silver migration through the electrolyte were resolved by incorporating cell encapsulation and engineering the sol-gel separator. In Chapter 3, binder-solvent-catalyst interactions in the air cathode inks and printed films were studied in order to optimize the oxygen reduction reaction (ORR) at the cathode. However, through our previous studies, Zn corrosion has been identified as the dominant failure mechanism in both Zn-Ag₂O and Zn-air batteries, limiting battery scaling, capacity, and lifetime. Zn corrosion in alkaline electrolytes has been studied for several decades, but the kinetics of these reactions at electrode-electrolyte interfaces are still poorly understood. Zn corrosion in alkaline solutions follows a complex series of intermediate reactions and is highly dependent on properties of the electrolyte (OH⁻ concentration, use of additives), properties of the electrode (particle size, porosity), and cell operating conditions (temperature, current density, depth of discharge, cell geometry).^[1] Thus, each of these factors can alter the fundamental Zn corrosion mechanism and need to be studied systematically to understand their influence on battery performance.

In order to better understand Zn corrosion and its effect on battery integration for wireless sensor networks, this work utilizes *operando* characterization techniques, which have recently become an emerging set of tools to investigate transient, non-equilibrium materials such as electrochemical interfaces.^[2,3] These methods allow for the coupling of standard electrochemical measurements with various characterization techniques to simultaneously gather chemical or physical information and battery performance in real time. The use of *operando* characterization techniques represents a significant shift in the research of battery materials. In most electrochemical systems, degradation and corrosion studies have primarily relied on ex-situ analysis, which are not representative of battery operating conditions and cannot directly probe reactions at an electrochemical interface. Furthermore, typical experiments from previous studies often rely on post-mortem analysis, which are subject to experimental or environmental artifacts and limit our understanding of corrosion mechanisms. Instead, moving to *operando* characterization techniques including X-ray (diffraction, absorption, tomography), spectroscopic (Raman, infrared), and spectrometric (mass, neutrons) techniques allow for direct observation of electrochemical interfaces and can help identify critical factors that influence corrosion.

This chapter sets out to provide a framework for designing more corrosion resistant anode materials for printed batteries. Anodic corrosion is a limiting factor in a variety of aqueous battery chemistries, including several emerging metal-air systems such as Zn-air, Mg-air, and Al-air batteries. By coupling additive manufacturing with *operando* characterization, this work demonstrates a rapid screening approach to determine how battery materials and operating conditions affect corrosion in a printed aqueous battery. Here, we investigate corrosion mechanisms in Zn-air batteries as a proof of concept of our screening method, using the printed

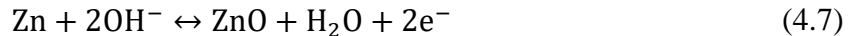
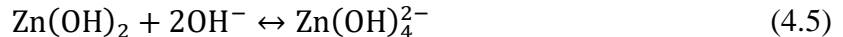
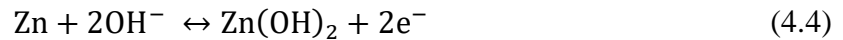
Zn-air battery developed in Chapter 3. Pressure decay analysis and differential electrochemical mass spectrometry (DEMS) are at the core of our rapid screening method, utilizing fairly simple and inexpensive instrumentation to quantify *operando* corrosion rates for different electrode/electrolyte compositions and battery geometries. This enables a high-throughput approach to quickly compare hydrogen evolution rates for different cell designs. Additionally, *operando* X-ray diffraction (XRD) experiments are incorporated to verify the formation of solid corrosion products at the electrode-electrolyte interface and examine their evolution under critical battery degradation factors.

4.2 Zn Corrosion in Alkaline Environments

Zn corrosion in alkaline electrolytes limits battery performance by isolating active Zn particles and lowering the capacity of the battery. In commercial Zn-air batteries for example, Zn electrodes are typically designed to be two to three times the volume of the cathode in order to have sufficient Zn available for discharge, but typically less than 60% of the Zn is utilized under discharge.^[4] This capacity loss is due to the electrochemical nature of the electrode-electrolyte interface for a Zn electrode in an alkaline electrolyte. Zn undergoes a series of chemical reactions that lead to both hydrogen evolution and ZnO precipitation on the electrode surface, causing passivation of the Zn electrode that restricts the flow of charge in the battery.^[5-7] This concept is illustrated in Figure 4.1 for a Zn-air battery. Because Zn has a reduction potential outside of the water stability window (more negative than hydrogen), the hydrogen evolution reaction (HER) occurs when Zn comes in contact with water. The HER in Zn can be described by the half reactions (Equations 4.1–4.2) and the overall reaction (Equation 4.3):



As hydrogen is evolved through HER, Zn oxidation occurs at open-circuit conditions. This process competes with Zn conversion during discharge, which follows a series of intermediate reactions (Equations 4.4–4.6) that sum to the overall anodic half-cell reaction (Equation 4.7):



Thus, Zn undergoes two competing oxidation reactions, one that is useful (hydroxide formation) and one that is not useful (oxide formation), which is referred to as corrosion. In both cases, additional ZnO formation typically passivates the surface, but this greatly depends on several operating conditions including depth of discharge, temperature, electrolyte concentration, and many others.^[1] In the case of depth of discharge, Figure 4.2 shows a proposed evolution of hydroxide and oxide species that leads to passivation. As referenced in Section 2.3, type 1 behavior indicates hydroxide evolution that is soluble in the alkaline solution, which will not result in surface passivation. At some critical depth of discharge (or critical time as indicated in Figure 4.2),

hydroxide species will begin oxidizing further to ZnO, which will precipitate out of solution and begin forming a passivation layer, characterized as type 2 behavior.^[5,8] Finally, at sufficiently high depths of discharge, direct oxidation of Zn to ZnO becomes possible through type 3 behavior. This third behavior is not fully understood in the literature but is suggested to be connected to decreases in the electrochemical potential of the anode. It is also possible that hydrogen evolution is accelerated in this region, but conclusive studies to determine the mechanism have not been established. This is partially due to the complex nature of the series of corrosion reactions and their direct dependence on a variety of battery architectures and operating conditions.

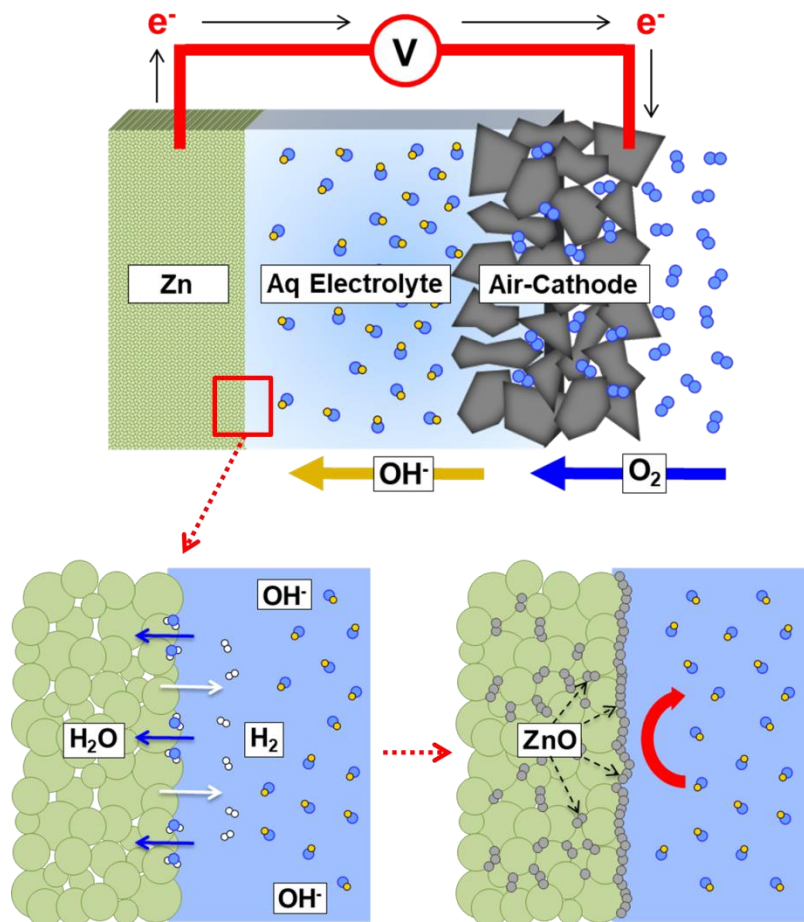


Figure 4.1: Illustration of the corrosion mechanism for a Zn electrode in an alkaline electrolyte. Hydrogen gas is formed at Zn sites in contact with water molecules, which can lead to pressure increases and volume expansion of packaged cells. The corrosion reaction proceeds until all Zn surface sites have been converted to ZnO. This passivates the electrode and prevents useful discharge of the cell since OH^- ions cannot reach available Zn sites.

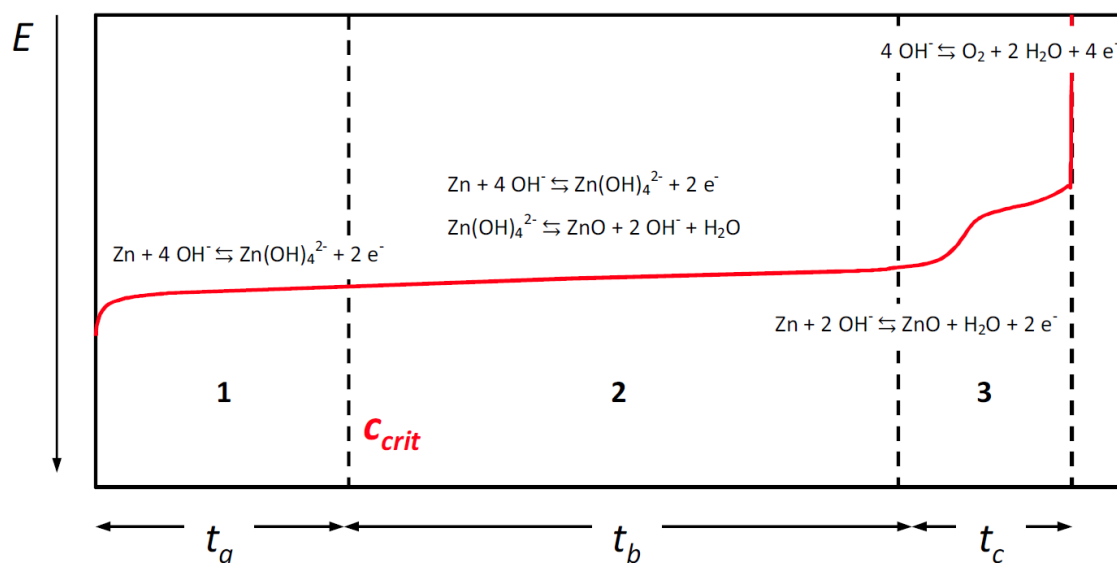


Figure 4.2: Proposed mechanism for anodic passivation of Zn electrodes as a function of depth of discharge.^[5]

In order to suppress the hydrogen evolution reaction, several electrode and electrolyte additives have also been investigated for use in Zn batteries. These studies have primarily utilized metal-oxide additives in the electrode such as bismuth oxide, indium oxide, calcium oxide, and aluminum oxide to increase the overpotential of the HER.^[9–14] Mechanisms for this increase in overpotential are unclear and still being debated in the literature. Some studies suggest preferential reduction of metal-oxide additives, such as Bi_2O_3 to Bi, which leads to an increased electrode conductivity and a greater charge transfer in the Zn electrode. Others suggest a morphological change to the Zn anode, indicating that these metal additives decrease porosity in the Zn anode near the electrolyte interface that can impact zincate dissolution and ZnO precipitation. Additional studies have also examined additives to the alkaline electrolyte to mitigate Zn corrosion. These have included methods to both increase zincate saturation and decrease zincate saturation.^[15] Additives that increase zincate saturation help prevent surface passivation to ZnO and enhance capacity in primary cells, but lead to accelerated redistribution of redox products and significant shape change of the electrode microstructure over time.^[16–18] Conversely, additives that decrease zincate saturation force earlier ZnO precipitation, but restrict zincate diffusion away from the electrode surface, which can help minimize shape change and enhance reversibility of the Zn electrode at the cost of lower capacity.^[19,20]

Although Zn corrosion has been widely studied, most investigations have only examined a few design variables and have ignored the dynamic interactions that occur at the electrode-electrolyte interface. Given the intermediate stages of Zn corrosion described in Equations 4.4–4.7 and shown in Figure 4.2, Zn corrosion rates are dependent on several interdependent factors, including properties of the electrolyte (OH^- concentration, use of additives), properties of the electrode (particle size, porosity), and cell operating conditions (temperature, current density, depth of discharge, cell geometry). For printed batteries, cell operating conditions and cell geometry are crucial parameters and often dictated by the supported device. As discussed in Section 2.3, printed battery geometry plays a critical role in cell performance, limiting battery

lifetime as electrode size decreases. Differences in electrode surface morphology with decreasing electrode size were also observed, as shown in Figure 4.3, and were attributed to different intermediate reactions and concentrations of zincate and ZnO species at the electrode surface. This work aims to further investigate this observation and determine whether or not electrode size influences corrosion rate, among several other important design parameters in the printed Zn-air battery.

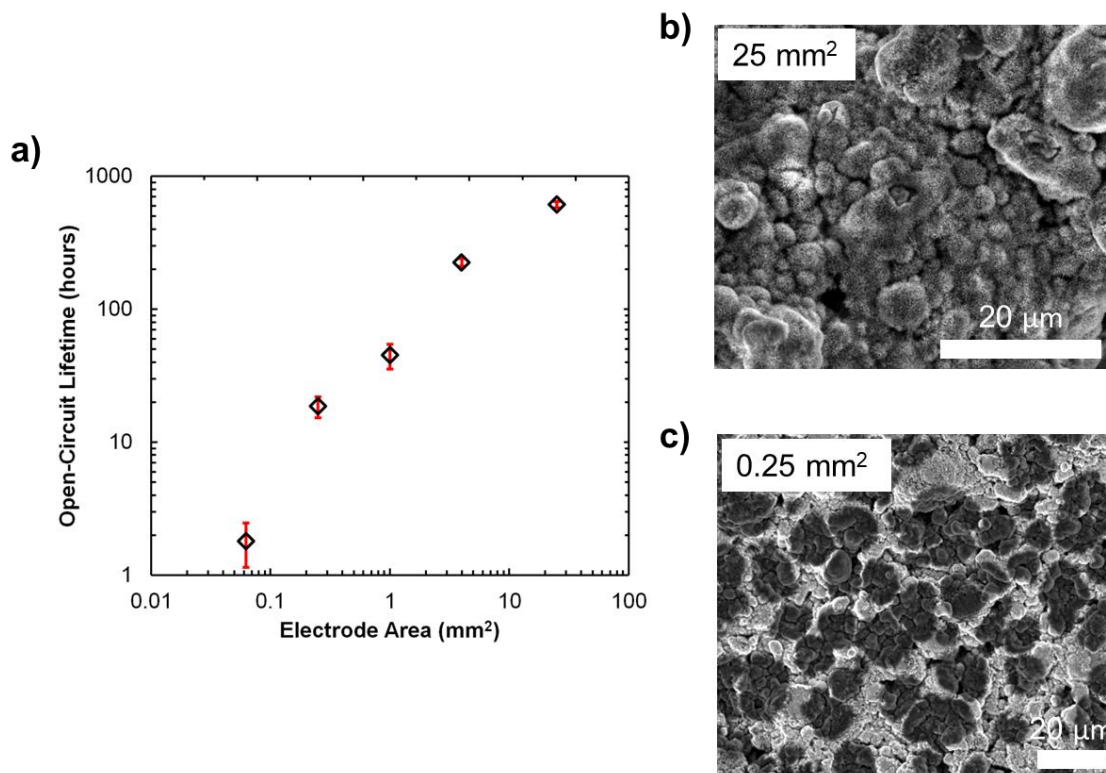


Figure 4.3: a) Open-circuit lifetime as a function of printed electrode size, with SEM images highlighting the morphological differences in ZnO formation between b) 25 mm² and c) 0.25 mm² Zn electrodes after 24 hours of exposure to an 8.4 M KOH electrolyte. The 25 mm² printed electrode shows homogenous hydroxide precipitation over the electrode surface with needle-like growth, whereas the 0.25 mm² electrode shows a ZnO passivating film at the electrode surface.

4.3 Quantifying Corrosion Rates via DEMS and Pressure Decay Measurements

Operando characterization of cell electrochemistry often relies on using qualitative techniques to identify reaction mechanisms and monitor evolution of interfaces. In Zn batteries, several researchers have utilized X-ray tomography and optical microscopy to observe the nature of Zn particle shape change during battery operation.^[21–26] However, these methods are somewhat subjective and rely on image processing that can be tedious and time consuming, which restricts the ability to rapidly screen several electrode/electrolyte properties and cell operating conditions simultaneously. Rather than solely monitoring physical changes to the anode structure, we can simply monitor the evolution of hydrogen gas to determine Zn corrosion rates. As defined in Equation 4.3, the amount of hydrogen evolution corresponds directly to Zn dissolution and

passivation and allows us to quantify cell corrosion rates. Using DEMS to confirm molecular species of the produced gaseous products and pressure decay analysis (as outlined in Chapter 3) to rapidly measure gas evolution, we can closely monitor Zn corrosion under realistic operating conditions and high depths of discharge, which has been lacking in prior literature reports. Furthermore, this methodology allows us to determine corrosion characteristics of the entire anode rather than analyzing only a small fraction of the anode volume. Essentially, we can measure a total corrosion rate in the cell and evaluate several batteries in parallel to find average corrosion rates for a variety of battery parameters and operating conditions.

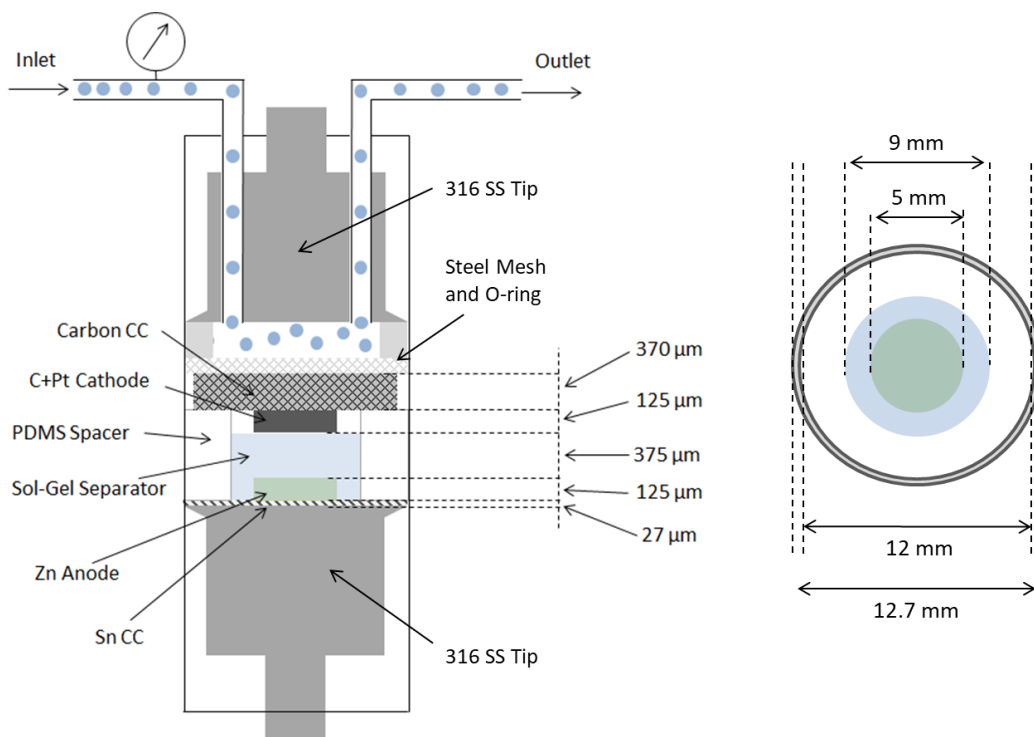


Figure 4.4: Schematic of Swagelok cell design for pressure decay and DEMS measurements.

To perform DEMS and pressure decay experiments, a custom-built cell was developed based on a modified Swagelok cell design to ensure high hermetic integrity for accurate pressure and mass spectrometry analysis. As shown in Figure 4.4, a fused silica tube is sealed against 1/2" stainless steel current collectors (McMaster-Carr) with compressed ethylene-propylene (EP) o-rings. Zn-air batteries are printed using the same procedure outlined in Section 3.4 with a circular electrode geometry. The headspace volume was approximately 2100 μL for each cell, including the inlet and outlet capillaries, and all electrochemical experiments were conducted using a pure oxygen source. Ambient temperature was also measured throughout each experiment to account for temperature dependent fluctuations in headspace pressure. Cell potential during DEMS and pressure-decay experiments were collected using a Bio-Logic VSP Potentiostat. As discussed in Chapter 3, the pressure decay method utilizes oxygen consumption in the printed Zn-air battery to approximate the hydrogen evolution rate of the cell. Evolved hydrogen from the Zn anode, as described by the HER in Equation 4.3, can diffuse through the separator and react with pure oxygen at Pt catalyst sites in the porous cathode to produce water. Although the oxygen consumption rate does not directly match the hydrogen evolution rate as measured by DEMS, the pressure decay

method offers a convenient way to quickly screen battery parameters and operating conditions since the oxygen consumption rate will correlate with hydrogen evolution and anodic corrosion. Thus, we utilize pressure decay measurements to quickly compare corrosion across cell conditions and validate observed trends using DEMS to directly measure hydrogen evolution.

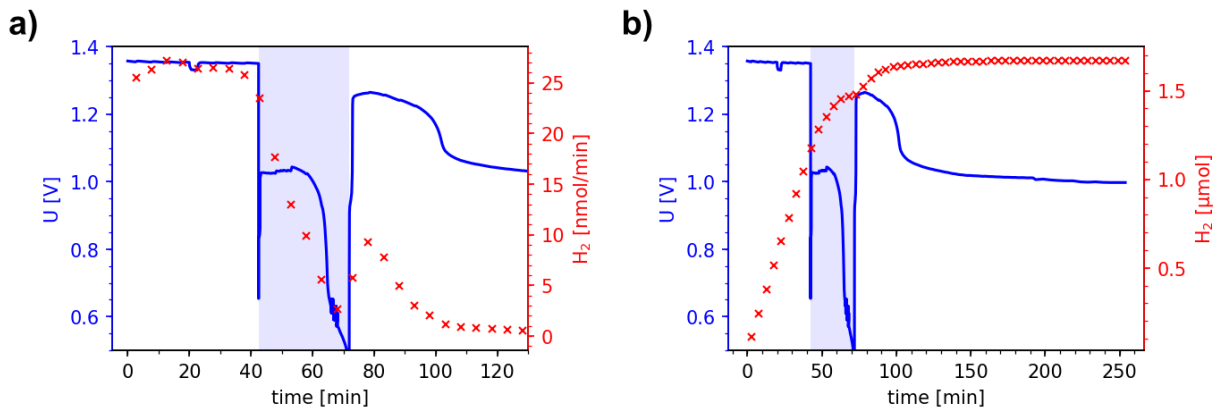


Figure 4.5: DEMS analysis of initial Zn-air battery design, showing a) hydrogen evolution rate and b) total evolved hydrogen gas. White sections correspond to open-circuit conditions and blue sections correspond to 20 mA cm^{-2} discharge.

As shown in Figure 4.5, our initial printed Zn-air battery design demonstrated a hydrogen evolution rate of about 25 nmol min^{-1} at open-circuit conditions. We also note that the corrosion rate decays to zero as the cell potential approaches the sudden death regime (type 3 behavior in Figure 4.2) where the anode surface completely passivates due to conversion of Zn to ZnO. Based on these initial DEMS results, we set out to determine the effects of individual factors on anodic corrosion through pressure decay experiments. These experiments included properties of the electrode (particle size, binder composition, current collector material), properties of the electrolyte (OH^- concentration, use of additives), and cell fabrication conditions (electrode thickness, electrode area). Pressure decay experiments analyzing these factors are included in Figures 4.6 – 4.10, with all cells measured at open-circuit conditions. Each experiment varied single factors, keeping all other conditions constant. Corrosion rates from pressure decay experiments were approximated with a 15 point rolling average of the rate of change of the oxygen consumption. This leads to some noise in the corrosion-rate data, which is typically less than $20\text{--}30 \text{ nmol min}^{-1}$. In addition, 4 to 6 printed cells were tested at each screening condition to estimate cell to cell variation, which showed that cell variance was typically less than 50 to 60 nmol min^{-1} . In each of the following figures, two cell measurements are shown to illustrate reproducibility of the pressure decay method. Based on our observations, changes of more than $100 \text{ nmol min}^{-1}$ were considered significant compared to background noise. This value is important in distinguishing which processing factors significantly affect corrosion. Table 4.1 summarizes the significance of each factor tested.

Among the factors tested, the anode current collector material had the greatest impact on corrosion rate, cell potential, and resulting battery lifetime. Figure 4.6 shows printed Zn-air batteries with Sn, Cu, Ni, and Mo anodic current collectors. Sn, Cu, Ni, and Mo were all chosen

Table 4.1: Significance of Zn corrosion factors as measured by pressure decay analysis.

Factor	p-value
Current Collector	0.003
Electrolyte Concentration	0.008
Electrolyte Additive	0.009
Zn Particle Size	0.036
Electrode Area	0.211
Electrode Thickness	0.241
Electrode Mass Loading	0.414

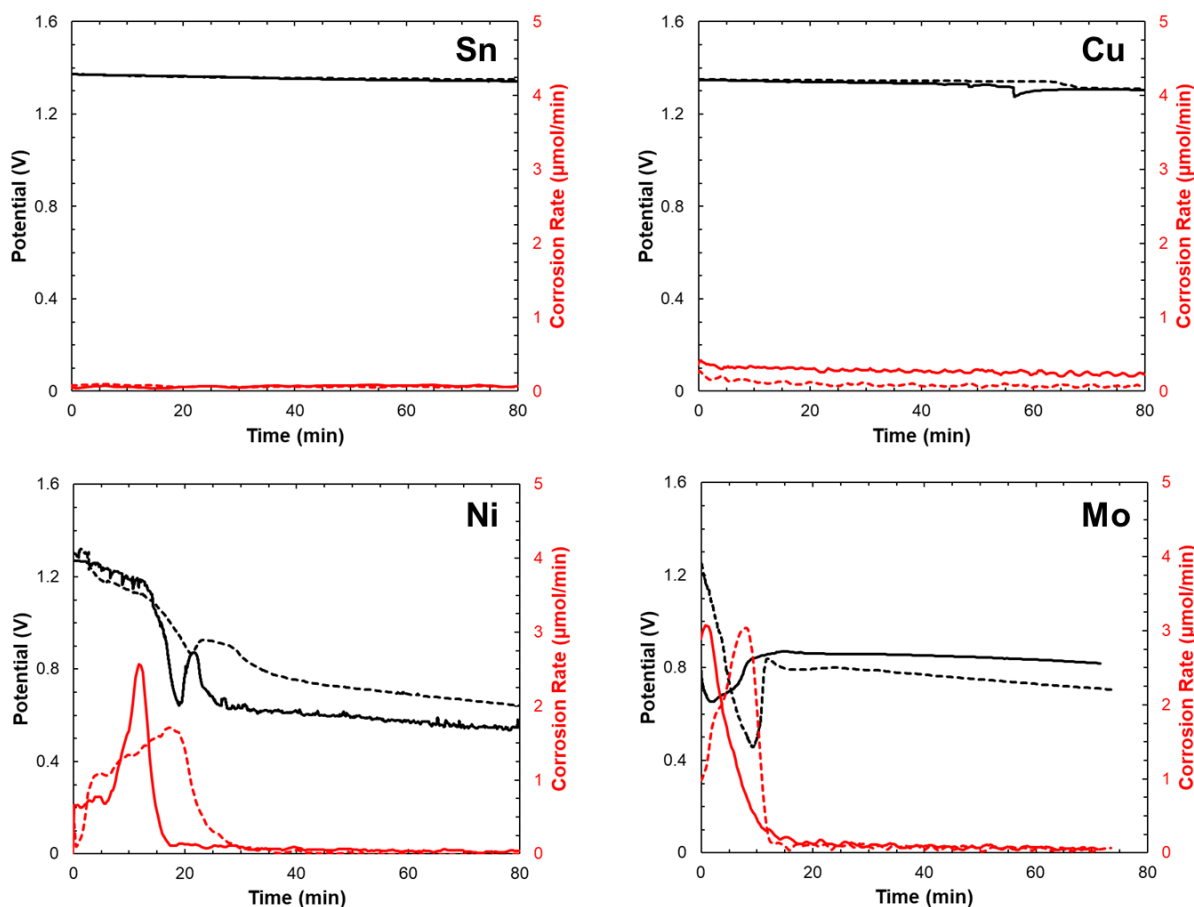


Figure 4.6: Pressure decay data from printed Zn-air batteries with various anodic current collector materials. Solid and dashed lines represent two batteries at the same condition, highlighting the reproducibility of the measurement. Decreases in cell potential follow correlate with increases corrosion rate, which is especially evident in the Ni and Mo samples.

since they have modest half-cell reduction potentials (-0.1 to -0.4 V vs. SHE) and form fairly conductive oxides. Compared to more inert materials such as Au or Ag, these metals should prevent Zn from being preferentially oxidized due to the mismatch in cell reduction potential. While Sn and Cu current collectors maintained low corrosion rates and stable cell potentials

throughout the measurement, Ni and Mo current collectors demonstrated large spikes in corrosion rate (red curves in Fig 4.6) within the first 20 minutes of cell testing. These sudden increases in corrosion rate also corresponded to rapid decreases in open-circuit potential (black curves in Fig 4.6). This follows the sudden death mechanism described in Figure 4.5, where high corrosion rates correspond to rapid passivation of the anode surface and conversion from Zn to ZnO. In the Ni and Mo samples, the corrosion rate falls significantly after the open-circuit potential stabilizes to a new equilibrium potential below 1 V, which signifies the complete passivation of the Zn surface. Given these results, Sn current collectors were chosen for all other studies given its slightly lower corrosion rate compared to copper and higher oxide conductivity.

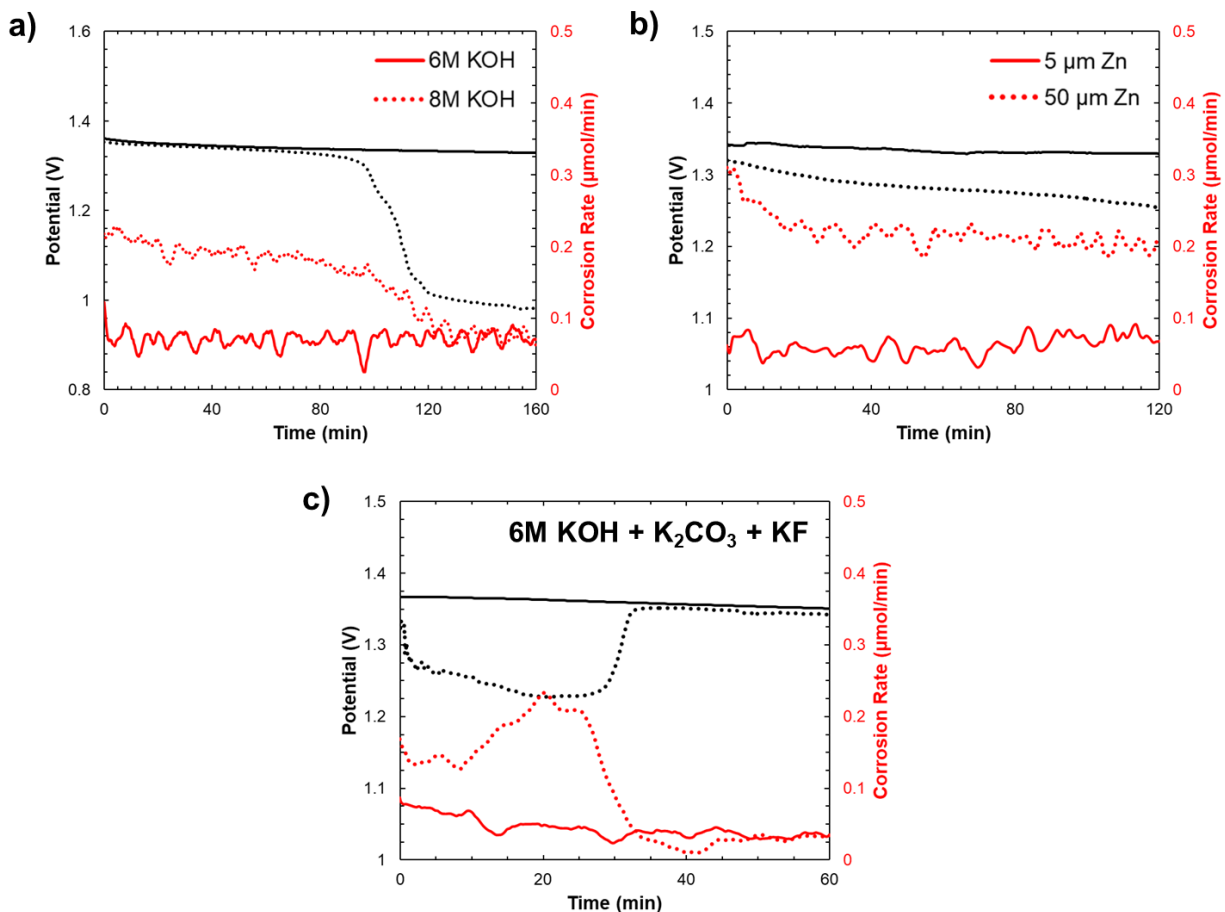


Figure 4.7: Screening experiments for a) electrolyte concentration, b) Zn particle size, and c) electrolyte additives. Electrolyte concentration and Zn particle size are shown to cause significant changes in corrosion rate on Sn anodic current collectors.

In addition to anode current collector, a few other factors were shown to significantly affect cell corrosion rate. Figure 4.7 highlights the effects of electrolyte concentration, Zn particle size in the printed electrode, and the use of potassium carbonate and potassium fluoride as electrolyte additives. Using Sn current collectors, lower corrosion rates were observed with a 6M KOH electrolyte and a 5 μm Zn particle size ($> 100 \text{ nmol min}^{-1}$ difference). Similar experiments with varying electrolyte concentration were performed on Au, a more inert and electropositive metal,

which showed that higher KOH concentrations are preferred. This seems to suggest a relationship between water activity and current collector reduction potential. Interestingly, Figure 4.7c shows what is likely an initialization process for a battery with K_2CO_3 and KF electrolyte additives, which are expected to decrease zincate solubility.^[15] The solid and dashed curves represent cells with the same processing conditions, but the dashed cell shows an increase and subsequent decrease in corrosion rate that tracks directly with the open-circuit potential. This observation may show that decreasing the zincate solubility may allow the Zn electrode to form a stable interphase region that helps prevent further Zn oxidation and hydrogen evolution, although further discharge studies are needed to show that these additives do not significantly reduce electrode capacity. However, these results further reinforce that open-circuit voltage and corrosion rate are correlated and verify that the pressure decay method is a useful tool for quickly identifying changes in corrosion rate.

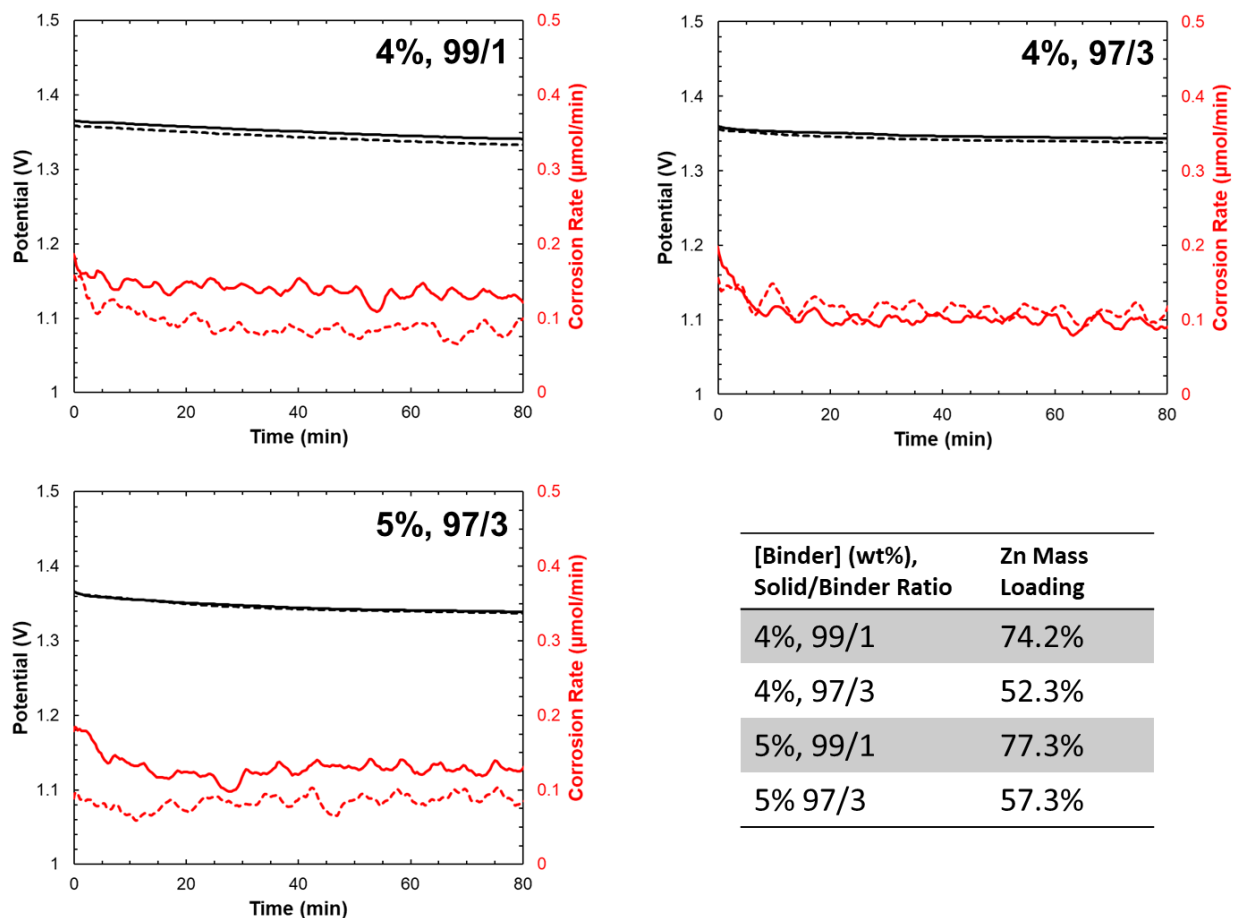


Figure 4.8: Screening experiments for electrode formulation based on binder concentration and the ratio of Zn with additives to binder. Each of the conditions tested showed similar corrosion rates of about $100 \text{ nmol min}^{-1}$.

While current collector material, electrolyte concentration, Zn particle size, and electrolyte additives were shown to influence Zn corrosion rates, several other factors were found to have no effect on corrosion. Figure 4.8 shows batteries with varying electrode formulation based on the binder concentration and resulting Zn mass loading in the electrode slurry. Regardless of binder

content and Zn mass loading, cell corrosion rates remained consistent at 80 to 120 nmol min⁻¹ with cell to cell variations of 10 to 30 nmol min⁻¹. Similar observations were found for electrode area and electrode thickness, as shown in Figures 4.9 and 4.10. This indicates that the cell lifetime results shown in 4.3 are not a product of accelerated corrosion at smaller electrode sizes, but that the smaller electrodes simply corrode faster due to the reduction in interface area. This suggests that decreasing particle size further or increasing electrode porosity may improve cell lifetime for batteries with small electrode areas, but further experiments are needed to verify this hypothesis.

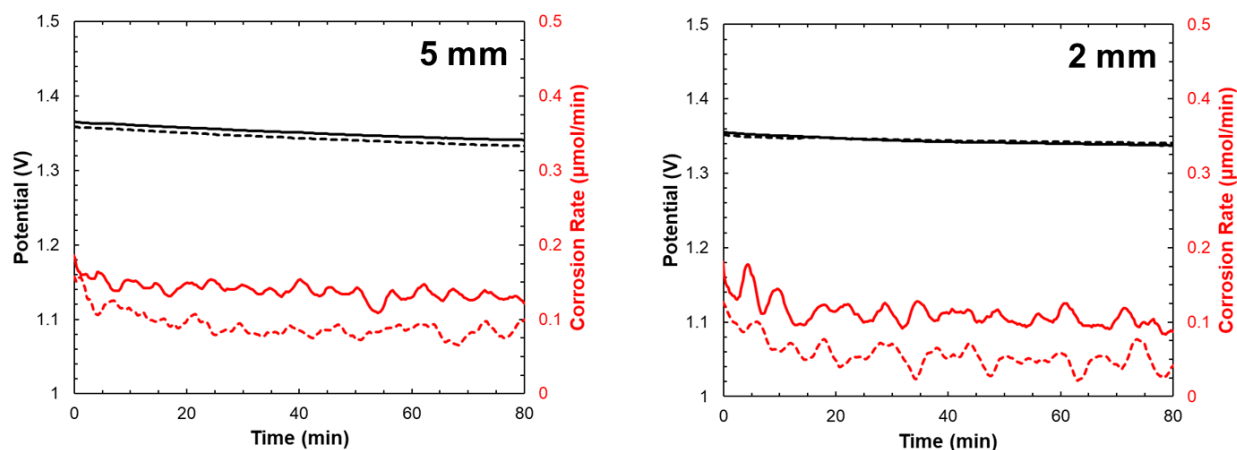


Figure 4.9: Screening experiments for Zn electrode diameter in the Swagelok cell, with similar corrosion rates observed at both 5 and 2 mm (~100 nmol min⁻¹).

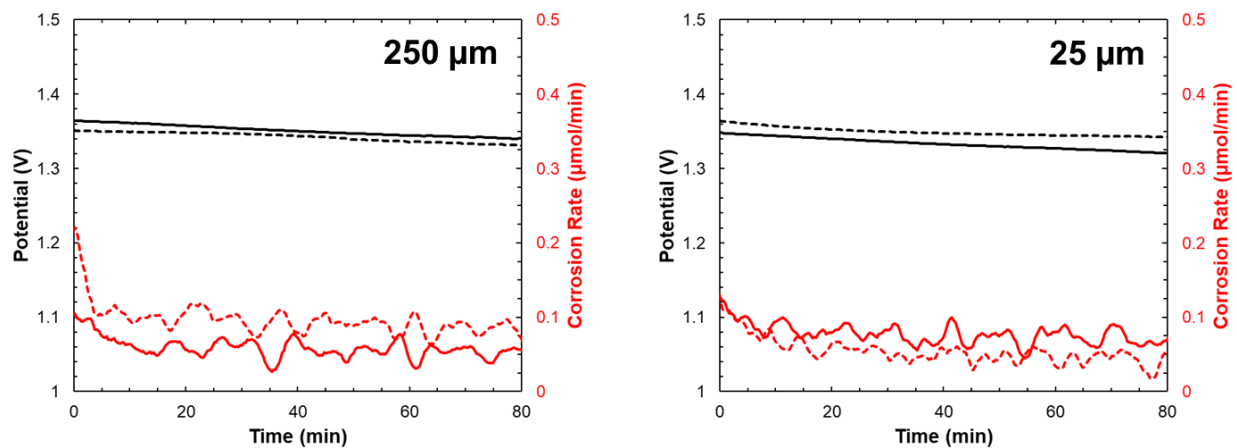


Figure 4.10: Screening experiments for Zn electrode thickness in the Swagelok cell, with similar corrosion rates observed at both 250 and 25 μm (~80 nmol min⁻¹).

Finally, DEMS analysis was conducted for an optimized Zn-air cell based on the results of our pressure decay experiments. Batteries were constructed with Sn current collectors, 6M KOH with K₂CO₃ and KF electrolyte additives, and a 5 μm Zn particle size. Figure 4.11 shows these results for two printed batteries at the same cell processing conditions. Hydrogen evolution rates under open circuit conditions were measured between 5 and 6 nmol min⁻¹, compared to ~25 nmol min⁻¹ for the unoptimized cells shown in Figure 4.5 (8M KOH, no electrolyte additive, 10 μm Zn

particle size). This demonstrates the efficacy of the pressure decay method to quickly screen battery parameters and operating conditions and determine their effect on corrosion rates. As confirmed by DEMS, we observed a significant reduction in the hydrogen evolution rate in printed Zn-air batteries using our optimized cell design.

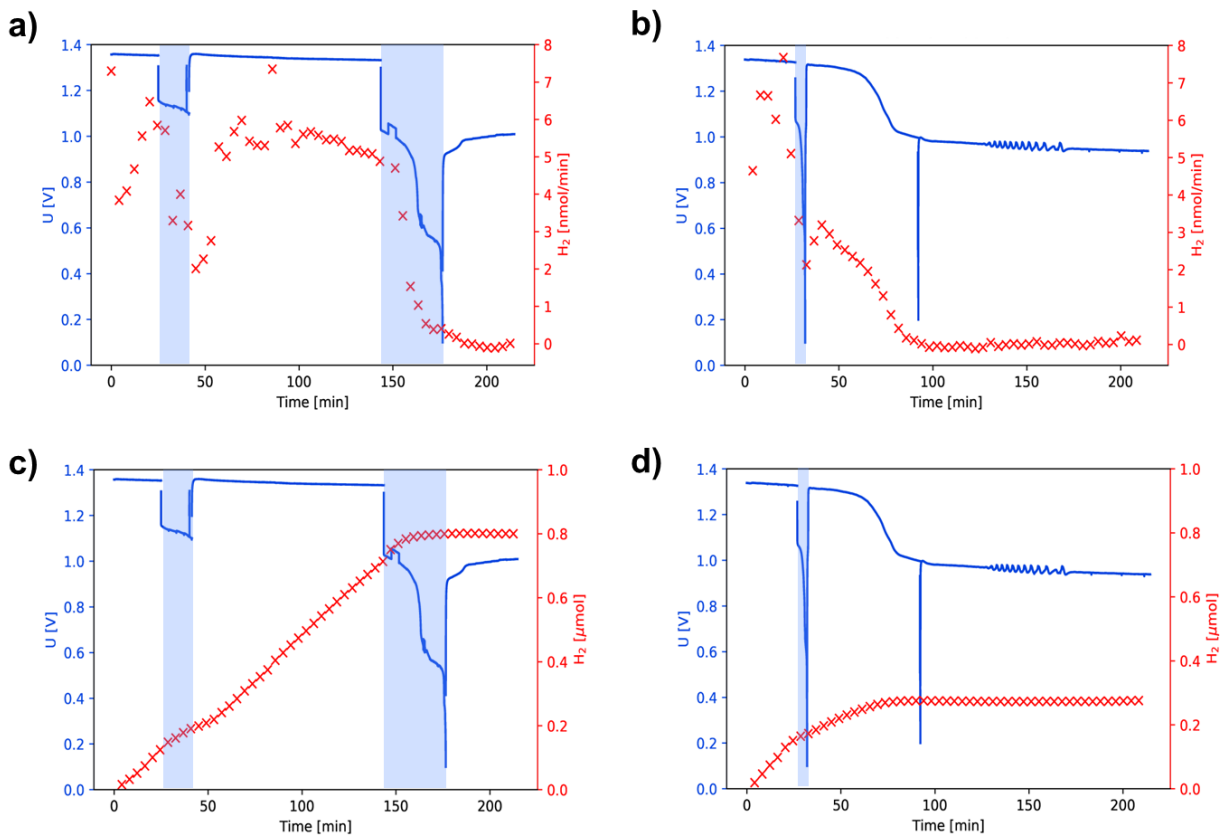


Figure 4.11: DEMS analysis of final Zn-air battery design, showing a,b) hydrogen evolution rate and c,d) total evolved hydrogen gas for two different cells with the same cell conditions. White sections correspond to open-circuit conditions and blue sections correspond to 20 mA cm⁻² discharge.

4.4 Operando X-ray Diffraction Analysis of Zn Corrosion

Pressure decay and DEMS experiments determined several factors that influence Zn corrosion in printed Zn-air batteries. To further visualize the reactions occurring at the electrode-electrolyte interface, *operando* X-ray characterization techniques are used to examine how important cell factors influence Zn corrosion. These experiments are intended to compliment pressure decay and DEMS measurements by directly detecting physical changes in the electrode under realistic operating conditions. To our knowledge, this is the first use of *operando* X-ray characterization techniques for printed batteries; so an explanation of the *operando* cell architecture will first be given to highlight key design criteria for compatibility with X-ray techniques.

All *operando* X-ray experiments in this work were conducted in transmission mode; so the battery stack was configured such that X-ray absorption was minimized throughout the stack. First, polyimide was chosen as an X-ray transparent substrate due to its common use in X-ray transmission experiments and its high mechanical stability at elevated temperatures compared to other polymer materials. This permitted us to evaporate metal anodic current collectors onto polyimide substrates with good substrate adhesion. Thin current collectors were required to prevent X-ray absorption, so evaporation was chosen such that metal films with thickness below 200 nm could be deposited. Zn anodes were also optimized to ensure suitable X-ray transmission for all experiments. Porous electrode films were achieved by varying the binder-solvent-active particle ratios in the precursor Zn inks. By lowering the binder concentration to 4% (compared to 5% in previous work) and decreasing the Zn mass loading to approximately 60% (compared to 77% in previous work), a suitable X-ray transparency was achieved. The cathode and cathodic current collector design remained the same from that described in Chapter 3 as the Pt content was kept at 5 wt% and was not expected to lower X-ray transmission significantly. However, the electrolyte volume was restricted to 30 μL to minimize scattering in the sol-gel.

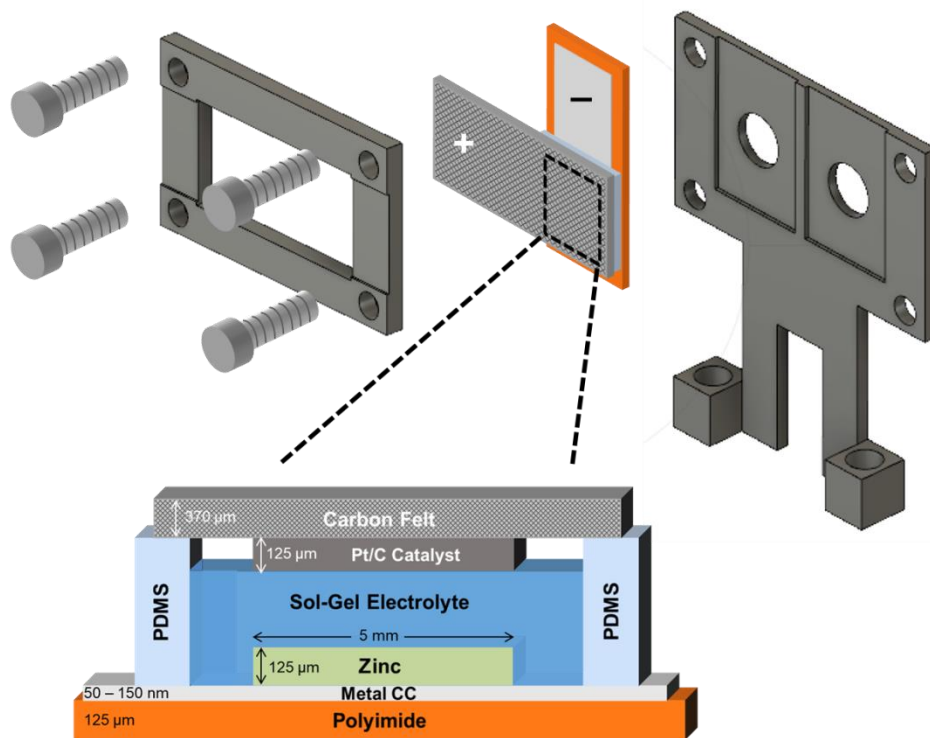


Figure 4.12: Schematic of *operando* X-ray cell design. Batteries are printed on polyimide to provide an X-ray transparent substrate.

Printed Zn-air batteries were tested at the Stanford Synchrotron Radiation Lightsource (SSRL) at the SLAC National Accelerator Laboratory. Beamlines 7-2 and 11-3 were used for diffraction experiments. Given that each experimental beamline had different stage and alignment configurations, customizable cell mounts were created using a 3D printer. As shown in Figure 4.12, the printed Zn-air batteries were assembled into a vertical mount. 3D printed cell holders were made using a Monoprice MP Select 3D Printer with PET filament to ensure no electrolyte

leakage or contamination. Battery slots were printed with grooves that matched the cell thickness dimensions, holding the cell in a constant position during testing. This also allowed multiple batteries to be tested in parallel at the lightsource. Holes were aligned to with the battery stack, enabling simple cell alignment during X-ray measurements since the thick PET holder showed high X-ray absorption relative to the printed battery.

With this *operando* X-ray cell design, diffraction experiments were conducted to determine the nature of Zn conversion to ZnO in the printed Zn-air battery. Specifically, the effects of anodic current collector material and electrolyte concentration on Zn corrosion were studied, given that these factors were deemed significant from the pressure decay analysis. Previous studies using *operando* XRD to study Zn corrosion are very limited, primarily focusing on the evolution of electrode additives such as Bi₂O₃ and its conversion to metallic Bi.^[27] Using pressure decay and DEMS analysis to guide our approach, we could focus our synchrotron based studies on factors shown to influence Zn corrosion. This is an important consideration for any *operando* X-ray characterization study given the time and cost required to perform these experiments. Diffraction experiments were conducted using a 14 keV source and scans were collected on each sample approximately every 10 seconds. A Bio-Logic VSP potentiostat was connected to the *operando* cell inside the beamline hutch and used to measure cell potential and control discharge currents.

Figure 4.13 shows the comparison of Sn and Au anodic current collectors in the *operando* cell. Both cells used a 6M KOH electrolyte and 5 μm Zn particles in the electrode ink. Both cells also demonstrated an initial open-circuit voltage above 1.2 V, as shown in Figure 4.13a, and were discharged at 10 mA cm⁻² until reaching 0.8 V, followed by open-circuit conditions. The Au cell reaches sudden death and type 3 corrosion faster than the Sn cell, and Figure 4.13b-c shows that conversion from the Zn to ZnO phase occurs more rapidly in the Au cell compared to the Sn cell. Decreases to the Zn (101) peak and increases in the ZnO (100) and (002) peaks are observed in both cells, which is consistent with previous *operando* X-ray experiments on Zn electrodes.^[27]

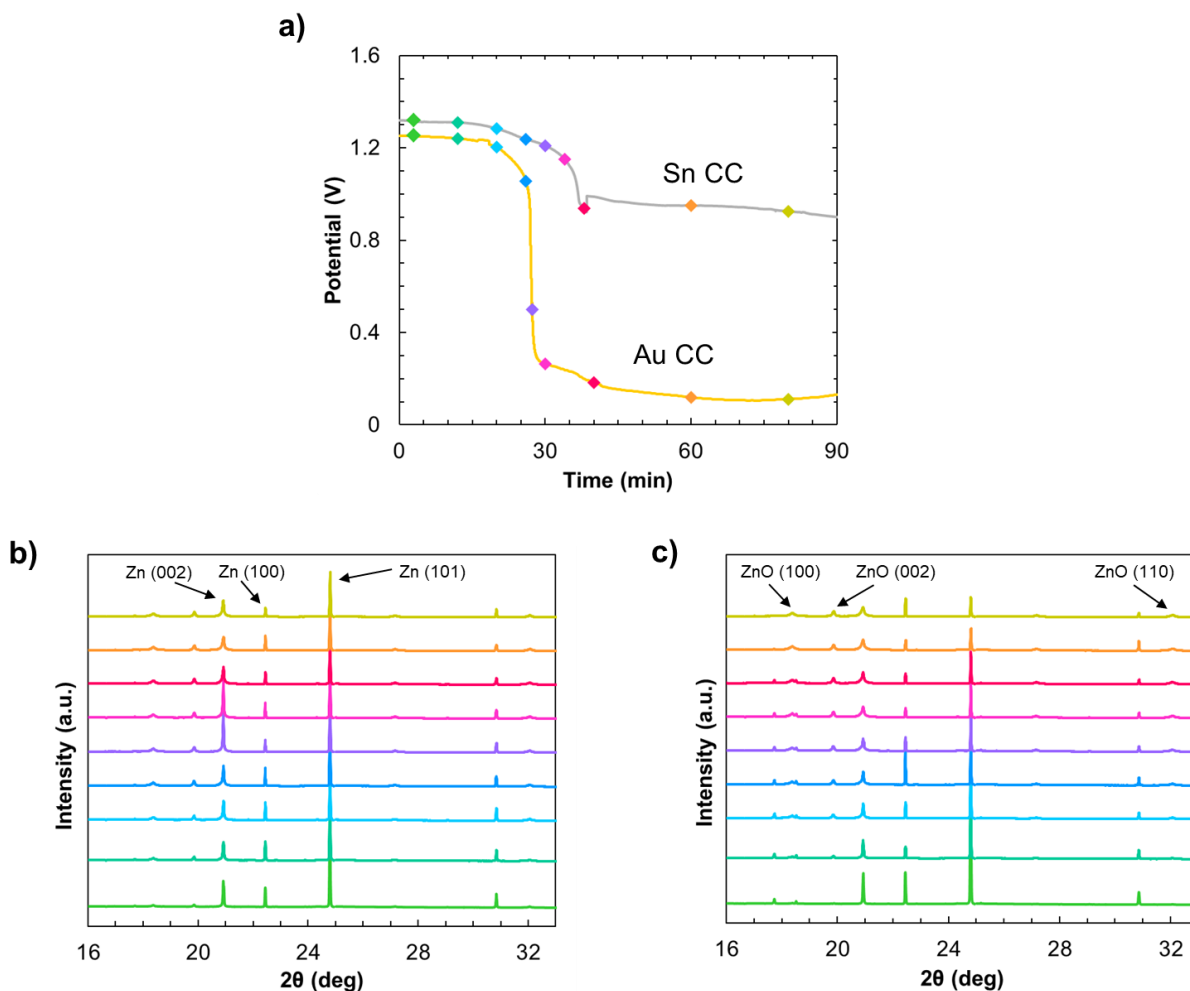


Figure 4.13: a) Discharge profiles of *operando* cells with Sn and Au current collectors, with X-ray scans collected for the b) Au cell and c) Sn cell. Colors of the X-ray scans match the time markers in the discharge profiles. Prominent Zn and ZnO diffraction peaks are labelled.

Figure 4.14 shows the comparison of 6M and 8M electrolytes in the *operando* cell with both batteries using a Sn current collector and 5 μm Zn particles. Both cells were discharged at 10 mA cm^{-2} until reaching 0.8V. As shown in Figure 4.14a, the 6M cell had a higher initial open-circuit potential than the 8M cell. Similar results to the current collector studies were observed with the 8M cell reaching sudden death and type 3 corrosion faster than the 6M cell. Again, this corresponded to a more rapid conversion of the Zn phase to ZnO phase for the 8M cell compared to the 6M cell, as shown in Figure 4.14b-c, with decreases in the Zn (101) peak and increases in the ZnO (100) and (002) peaks.

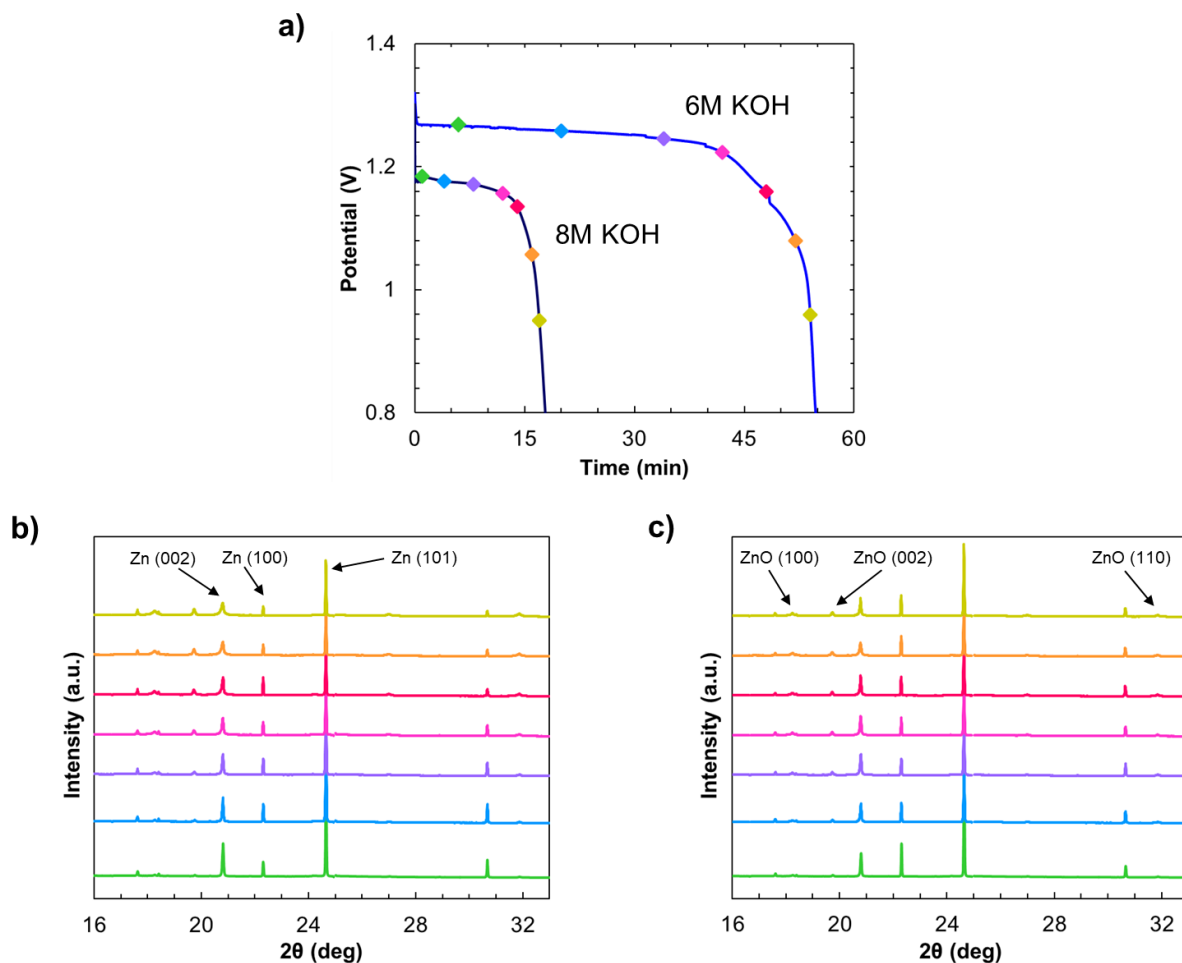


Figure 4.14: a) Discharge profiles of *operando* cells with 8M and 6M KOH electrolytes, with X-ray scans collected for the b) 8M cell and c) 6M cell. Colors of the X-ray scans match the time markers in the discharge profiles. Prominent Zn and ZnO diffraction peaks are labelled.

Additionally, characteristic differences in Zn dissolution were observed via *operando* XRD for the Zn-air cells with a higher corrosion rate. Figure 4.15 highlights the ratio of the Zn (002) peak intensity versus the Zn (101) peak intensity for each *operando* experiment, with each data point corresponding to an individual X-ray scan. Zn-air cells with lower corrosion rates (Sn current collector, 6M KOH) showed fairly constant peak ratio values throughout cell discharge. In contrast, Zn-air cells with higher corrosion rates (Au current collector, 8M KOH) showed sudden increases in the peak ratio. The time of the peak ratio increases match the onset of type 3 corrosion and sudden death in both Zn-air cells (25-30 min region for Au current collector, 15-20 min region for 8M KOH). Increases in the Zn (002) to Zn (101) peak ratio may indicate a preferential orientation for Zn corrosion in cells exhibiting a high corrosion rate, with Zn (101) conversion to ZnO occurring more rapidly than other Zn planes. This suggests that tailoring the Zn-particle surface orientation could affect the Zn corrosion mechanism, but further studies are needed to examine these observations.

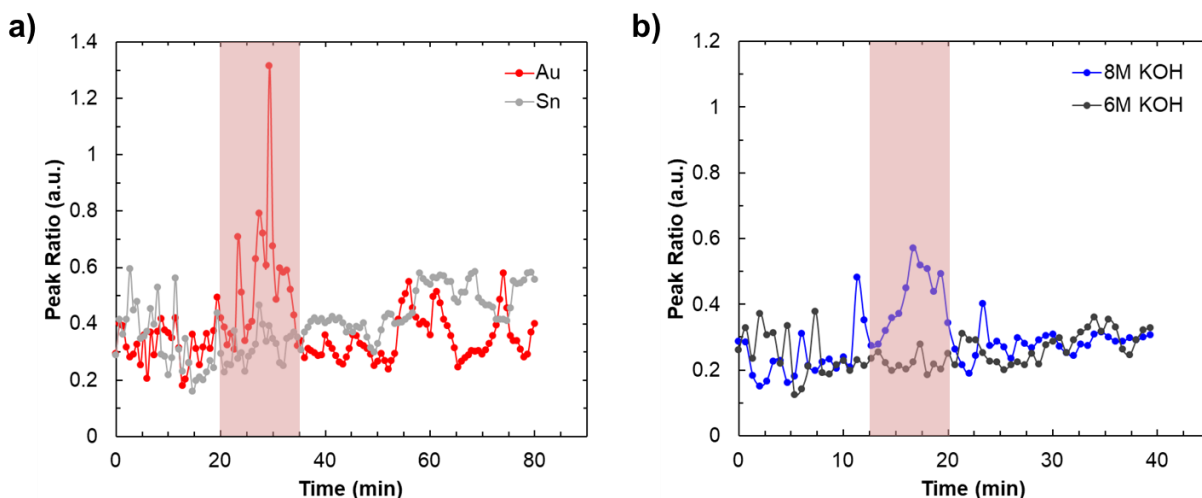


Figure 4.15: Ratio of Zn (002) to Zn (101) peak intensity for a) current collector and b) electrolyte concentration experiments with the corresponding regions of type 3 corrosion highlighted in red for the Au current collector and 8M KOH samples.

Overall, *operando* XRD measurements further support the pressure decay and DEMS data and show that current-collector material and electrolyte concentration influence Zn corrosion rate. Current-collector material will dictate the galvanic couple formed at the anode and thus can have a large influence on the thermodynamic driving force for Zn oxidation. Meanwhile, our results indicate that the kinetics of Zn corrosion are likely surface limited as KOH concentration dictates the solubility of zincate and hydroxide ions and the progression of the reactions described in Equations 4.4–4.7. Furthermore, Zn-particle size also influences total electrode surface area and should be further investigated as a limiting factor for anodic corrosion.

4.5 Summary

In summary, *operando* X-ray and electrochemical characterization techniques were used to elucidate critical factors that influence corrosion in printed Zn-air batteries. DEMS experiments were utilized to quantify hydrogen evolution at the Zn anode while pressure decay experiments enabled rapid screening of cell conditions and high-throughput experimentation to determine corrosion rate statistics. Overall, anode current collector material, electrolyte concentration, and Zn particle size were observed to significantly impact corrosion rates in printed Zn-air cells, leading to a reduction in hydrogen evolution rate from 25 to 5 nmol min^{-1} for the optimized cell design. *Operando* XRD experiments confirmed that the use of Sn current collectors and lower electrolyte concentrations result in delayed type 3 corrosion behavior in printed Zn-air batteries. Additional studies are needed to explore the effect of Zn particle size, total electrode surface area, and Zn particle surface orientation as Zn corrosion is likely surface limited. Overall, this chapter provides a framework for future investigation of anodic corrosion in other aqueous battery chemistries and offers a fairly simple, inexpensive, and fast approach to quantify corrosion rates for a variety of battery architectures.

4.6 References

- [1] X. Zhang, *Corrosion and Electrochemistry of Zinc*, Springer, New York, **1996**.
- [2] J. Nelson Weker, M. F. Toney, *Adv. Funct. Mater.* **2015**, *25*, 1622.
- [3] D. Schröder, C. L. Bender, T. Arlt, M. Osenberg, A. Hilger, S. Risse, M. Ballauff, I. Manke, J. Janek, *J. Phys. D. Appl. Phys.* **2016**, *49*, 404001.
- [4] T. B. Reddy, *Linden's Handbook of Batteries*, McGraw-Hill, New York, **2011**.
- [5] M. Bockelmann, L. Reining, U. Kunz, T. Turek, *Electrochim. Acta* **2017**, *237*, 276.
- [6] K. Huber, *J. Electrochem. Soc.* **1953**, *100*, 376.
- [7] D. D. Macdonald, K. M. Ismail, E. Sikora, *J. Electrochem. Soc.* **1998**, *145*, 3141.
- [8] W. Hong, Z. Jia, B. Wang, *J. Appl. Electrochem.* **2016**, *46*, 1085.
- [9] A. M. Gaikwad, G. L. Whiting, D. A. Steingart, A. C. Arias, *Adv. Mater.* **2011**, *23*, 3251.
- [10] J. McBreen, E. Gannon, *J. Power Sources* **1985**, *15*, 169.
- [11] J. W. Gallaway, A. M. Gaikwad, B. Hertzberg, C. K. Erdonmez, Y. C. K. Chen-Wiegart, L. A. Sviridov, K. Evans-Lutterodt, J. Wang, S. Banerjee, D. A. Steingart, *J. Electrochem. Soc.* **2014**, *161*, A275.
- [12] M. Yano, S. Fujitani, K. Nishio, Y. Akai, M. Kurimura, *J. Power Sources* **1998**, *74*, 129.
- [13] M. Yano, S. Fujitani, K. Nishio, Y. Akai, M. Kurimura, *J. Appl. Electrochem.* **1998**, *28*, 1221.
- [14] J. Y. Huot, E. Boubour, *J. Power Sources* **1997**, *65*, 81.
- [15] J. F. Parker, I. R. Pala, C. N. Chervin, J. W. Long, D. R. Rolison, *J. Electrochem. Soc.* **2016**, *163*, A351.
- [16] K. Bass, P. J. Mitchell, G. D. Wilcox, J. Smith, *J. Power Sources* **1991**, *35*, 333.
- [17] P. C. Foller, *J. Appl. Electrochem.* **1986**, *16*, 527.
- [18] R. W. Lewis, J. Turner, *J. Appl. Electrochem.* **1975**, *5*, 343.
- [19] T. C. Adler, F. R. McLarnon, E. J. Cairns, *J. Electrochem. Soc.* **1993**, *140*, 289.
- [20] E. Fraçkowiak, J. M. Skowroński, *J. Power Sources* **1998**, *73*, 175.
- [21] I. Manke, J. Banhart, A. Haibel, A. Rack, S. Zabler, N. Kardjilov, A. Hilger, A. Melzer, H. Riesemeier, *Appl. Phys. Lett.* **2007**, *90*, 214102.
- [22] T. Arlt, D. Schroder, U. Krewer, I. Manke, *Phys. Chem. Chem. Phys.* **2014**, *16*, 22273.
- [23] R. Franke-Lang, T. Arlt, I. Manke, J. Kowal, *J. Power Sources* **2017**, *370*, 45.
- [24] V. Yufit, F. Tariq, S. Eastwood, M. Biton, P. D. Lee, P. Nigel, V. Yufit, F. Tariq, D. S. Eastwood, M. Biton, B. Wu, P. D. Lee, N. P. Brandon, *Joule* **2019**, *3*, 485.
- [25] Y. Song, J. Hu, J. Tang, W. Gu, L. He, X. Ji, **2016**, DOI 10.1021/acsami.6b11098.
- [26] E. Faegh, T. Omasta, M. Hull, S. Ferrin, S. Shrestha, J. Lechman, D. Bolintineanu, M. Zuraw, W. E. Mustain, *J. Electrochem. Soc.* **2018**, *165*, 2528.
- [27] F. Moser, F. Fourgeot, R. Rouget, O. Crosnier, T. Brousse, *Electrochim. Acta* **2013**, *109*, 110.

Chapter 5: Printed Battery Packaging and Integration for IoT Systems

5.1 Introduction

Broad distribution of wireless IoT networks depends not only on the miniaturization of energy storage but also the ability to seamlessly integrate IoT components into autonomous systems. Combining sensing, communication, and energy storage into millimeter-scale, single-chip nodes is necessary to achieve densely deployed arrays of IoT devices.^[1,2] Recent advances in process integration have enabled on-chip integration of sensing and communication components,^[3,4] but further work is needed to demonstrate energy storage integration that meets the design and performance requirements of a millimeter-scale node.^[5-8] This includes designing battery packaging and interconnects that are compatible with device architectures and processing techniques while ensuring energy storage can sustain IoT operation modes and performance benchmarks (as discussed in Section 1.1).

Printing-based fabrication techniques offer several advantages towards on-chip integration and are capable of simplifying system-level design. These methods utilize high-throughput processing methods that can additively integrate battery packaging and interconnects, eliminating the need for traditional battery packaging strategies such as coin or pouch cells.^[9,10] Furthermore, printing-based techniques are compatible with emerging microelectronics processing techniques such as wafer-level and chip-scale packaging and can complement integration strategies for sensing and communication components.

This chapter addresses several challenges related to system-level integration of printed batteries for IoT devices. First, printable millimeter-scale packaging and interconnect designs are explored using both 3D and inkjet printing. Each design is evaluated based on minimum feature size resolution and via resistivity to guide compatibility with various chip architectures. Second, printed Zn-Ag₂O batteries are simulated under IoT operation modes to determine performance benchmarks for an integrated system. Pulsed charge and discharge conditions are used to approximate energy harvesting from solar cells given various sampling intervals. Finally, printed Zn-Ag₂O battery arrays are demonstrated using screen printing for high-voltage and high-power applications. Screen printable ink design is discussed and compared to stencil printed cells shown in Chapter 2 and printed array reliability and performance are examined.

5.2 Printed Packaging and Interconnects

Integrating multiple devices on a single, millimeter-scale platform requires several processing, materials, and performance considerations. For example, packaging materials must be good electrical insulators to keep each device isolated. The packaging material must also maintain chemical compatibility with the battery electrolyte and provide a good physical barrier to avoid electrolyte leakage, which can damage electronic components in the system. Additionally, interconnects are required from the battery to the sensing and communication components to supply power during operation. Millimeter-scale nodes will likely utilize vertical integration in order to minimize system footprints, so vias can be used to form device interconnects. Via diameters will be dictated by the chip design and the size of relevant input and output pads but should be minimized to match device scaling demands. Finally, interconnects must be highly conductive to avoid significant current and power losses in the system. With these

requirements in mind, two printed packaging and interconnect designs are evaluated in this work. The first utilizes a 3D printed package and stencil printed interconnects, while the second incorporates inkjet printing for both packaging and interconnects. Each design has advantages and drawbacks, with both methods compared below. Specifically, we aim to identify minimum via feature sizes and interconnect resistances for each method.

5.2.1 3D Printed Packaging and Stencil Printed Interconnects

3D printing offers a fully additive approach towards integrating components in an IoT system. Fused deposition modeling (FDM) can be used to extrude polymer materials at relatively low temperatures with feature sizes on the order of 10s of μm . In this work, packages were constructed using a Monoprice MP Select 3D Printer with polyethylene terephthalate (PET) and polylactic acid (PLA) filaments using a 250 μm nozzle. PET filament can be extruded at 230 $^{\circ}\text{C}$ and PLA filament at 185 $^{\circ}\text{C}$ (based on their respective melting temperatures) and are compatible with semiconductor packaging flows. A proof of concept package design is illustrated in Figure 5.1, where a printed Zn-Ag₂O battery is connected to an SL900A RFID tag with data logging capabilities. In this design, the 3D-printed package is printed in sections based on device and architecture requirements and can achieve vertical stack integration to minimize the package footprint. Non-printed components such as the SL900A can be added using pick and place tools while printed batteries and interconnects are added sequentially in between 3D printing steps.

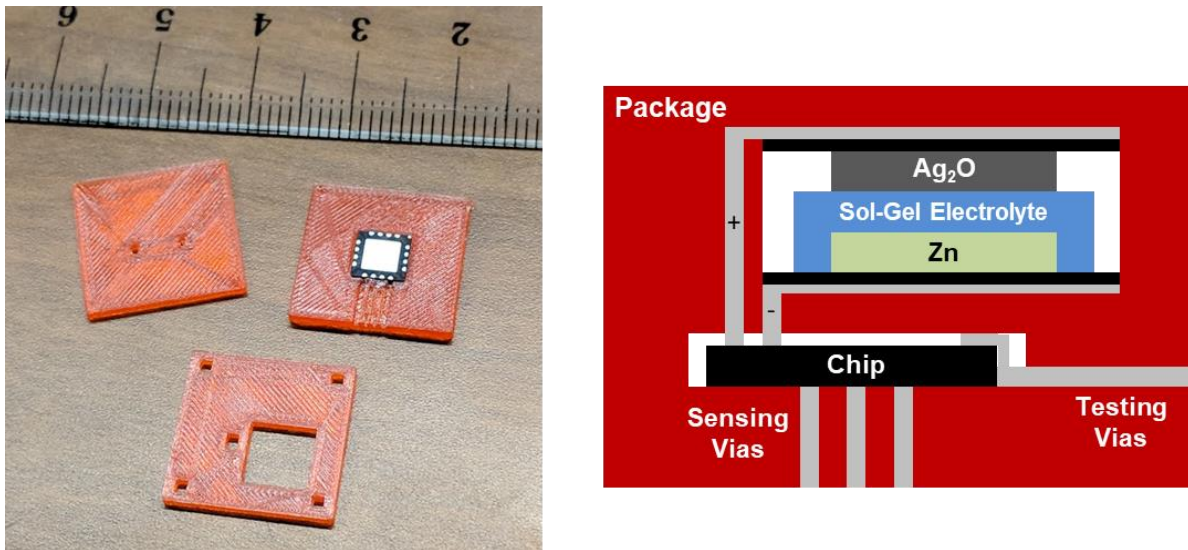


Figure 5.1: Image and schematic of a 3D printed package with stencil printed Ag interconnects.

In order to optimize the 3D-printed package for minimum via size, several fabrication parameters were evaluated. Among them, print speed and layer thickness were found to be important in determining print quality and via dimensions. Arrays of vias were printed with different print speeds (10 – 40 mm s^{-1}) and layer thicknesses (0.05 – 0.20 mm). Printing defects were commonly observed at higher print speeds ($\geq 30 \text{ mm s}^{-1}$), where portions of the printed filament delaminated from adjacent traces. This left unintended gaps in the printed package, which were often found next to printed vias, as shown in Figure 5.2. At lower print speeds ($< 20 \text{ mm s}^{-1}$), no printing defects were observed at the via sites. Lower print speeds increase the amount of

time the melted filament is in contact with the previous layer, which likely improves fusion between the individual polymer layers. Additionally, via diameter and film roughness were found to decrease at smaller layer thickness. Table 5.1 shows this dependence, with a 0.05 mm layer thickness having the smallest via diameter with an average of 0.189 mm. This via size is suitable for integration with the SL900A (0.4 x 0.3 mm pads) but is not sufficient for all devices, with smaller chip designs typically utilizing external Al pads with 50 to 200 μm diameters. Here, via diameters were limited by the resolution of the nozzle (250 μm), which was the smallest nozzle available for this 3D printer. Future studies should investigate the use of smaller nozzle sizes to further miniaturize 3D printed via dimensions.

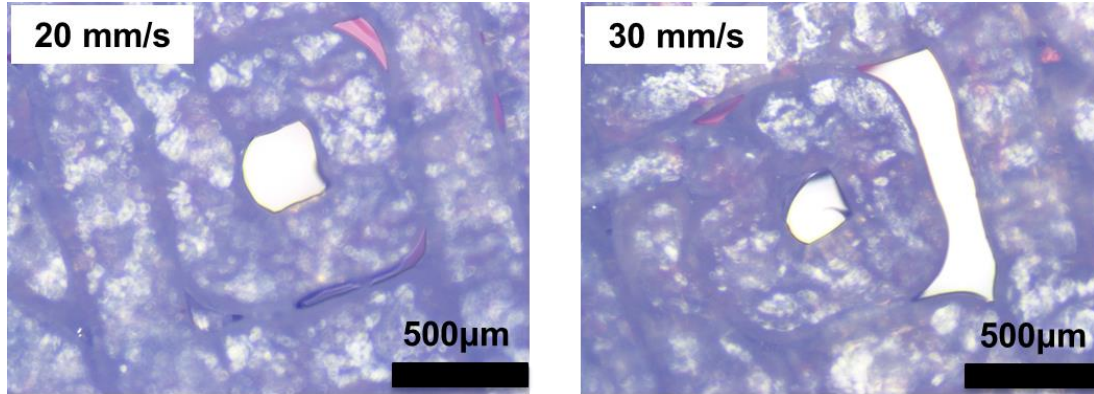


Figure 5.2: Example of printed via defects as a result of print speed.

Table 5.1: 3D printing design guidelines for the effect of layer thickness on average via area and film roughness with an expected via diameter of 0.25 mm.

Layer Thickness (mm)	Average Via Area (mm ²)	Average Via Diameter (mm)	Average Film Roughness (μm)
0.05	0.0281	0.189	78
0.10	0.0556	0.266	111
0.20	0.0762	0.311	147

Stencil printing was chosen to demonstrate metal-interconnect deposition in the 3D-printed vias. For the 3D-printed package, the minimum layer thickness and roughness are 0.05 mm and 78 μm respectively, so other digital printing techniques such as inkjet or spray would not be able to print feature sizes large enough to accommodate the package dimensions. Future package designs may be able to implement a fully 3D-printed structure that include 3D-printed metal interconnects, but would require a multi-nozzle FDM printer with higher extrusion temperature capabilities and is beyond the scope of this work. A commercially available Ag ink (Creative Materials #120-07) was used in order to achieve highly conductive traces at low processing temperatures. Printed vias were annealed at 110 $^{\circ}\text{C}$ on a hot plate for 15 min, which is below the thermal budget for both PET and PLA packages. However, chemical compatibility tests under an 8M KOH electrolyte showed Ag delamination from printed PLA substrates and PLA etching after 24 hours of exposure. PET substrates showed no apparent change after KOH exposure, so PET packages were used for further studies. Printed via resistance was determined for a variety of geometries, as highlighted in Figure

5.3. The via resistance was measured at or below $30\text{ m}\Omega$ for all configurations, which ensures that power losses from the battery to the other device components are minimal.

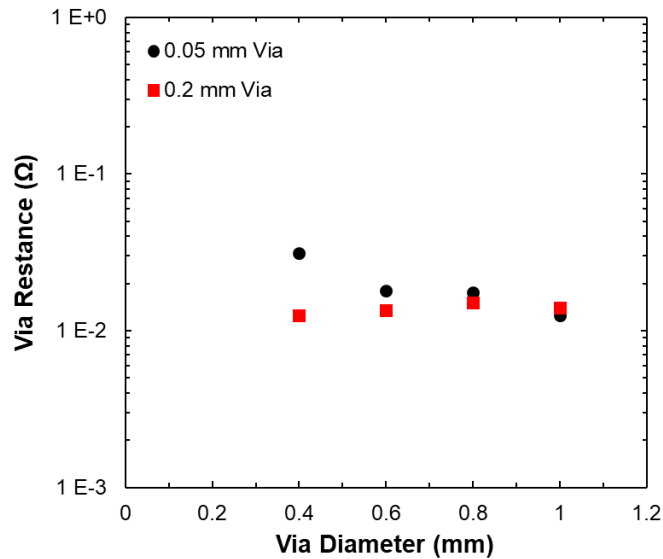


Figure 5.3: Ag interconnect performance with varying via geometry (diameter and length) in a 3D-printed PET package.

5.2.2 Inkjet Printed Packaging and Interconnects

While 3D printing may support a fully integrated package for IoT systems, inkjet printing can achieve much finer patterning resolution ($10\ \mu\text{m}$ linewidths) and enable printed interconnects for millimeter-scale nodes. Inkjet printing of nanoparticle-based inks has been previously demonstrated for a wide variety of materials and applications, including three-dimensional metallic interconnects.^[11,12] A proof of concept process flow for an inkjet printed system is shown in Figure 5.4, with this process tailored specifically for an emerging single-chip mote design from Prof. Kris Pister’s group. This process is adapted from previous work in our group pertaining to the development of inkjet-printed microelectromechanical relays.^[13–16] Inkjet-printed encapsulation and interconnects are deposited using a Fujifilm Dimatix materials printer (DMP-2831) with a Fujifilm Dimatix cartridge delivering a 1 pL droplet volume. Metallic interconnects were printed using a nanoparticle-based Ag ink (Advanced Nano Products). The insulating encapsulation layer was spin coated on the chip using a poly(4-vinylphenol) (PVP) solution composed of 10 wt% PVP and 2 wt% poly(melamine-co-formaldehyde) as a crosslinking agent dissolved in propylene glycol methyl ether acetate (PGMEA). PVP spin coating can be replaced by inkjet printing in future design iterations, but is used here to establish proof of concept of the method. Thickness dependence of the PVP layer on a 3 x 4 mm Si substrate is shown in Figure 5.5 after crosslinking for 30 min on a 200 °C hot plate. Film thicknesses of about 300 nm were achieved at 6000 RPM, which was used for all subsequent experiments.

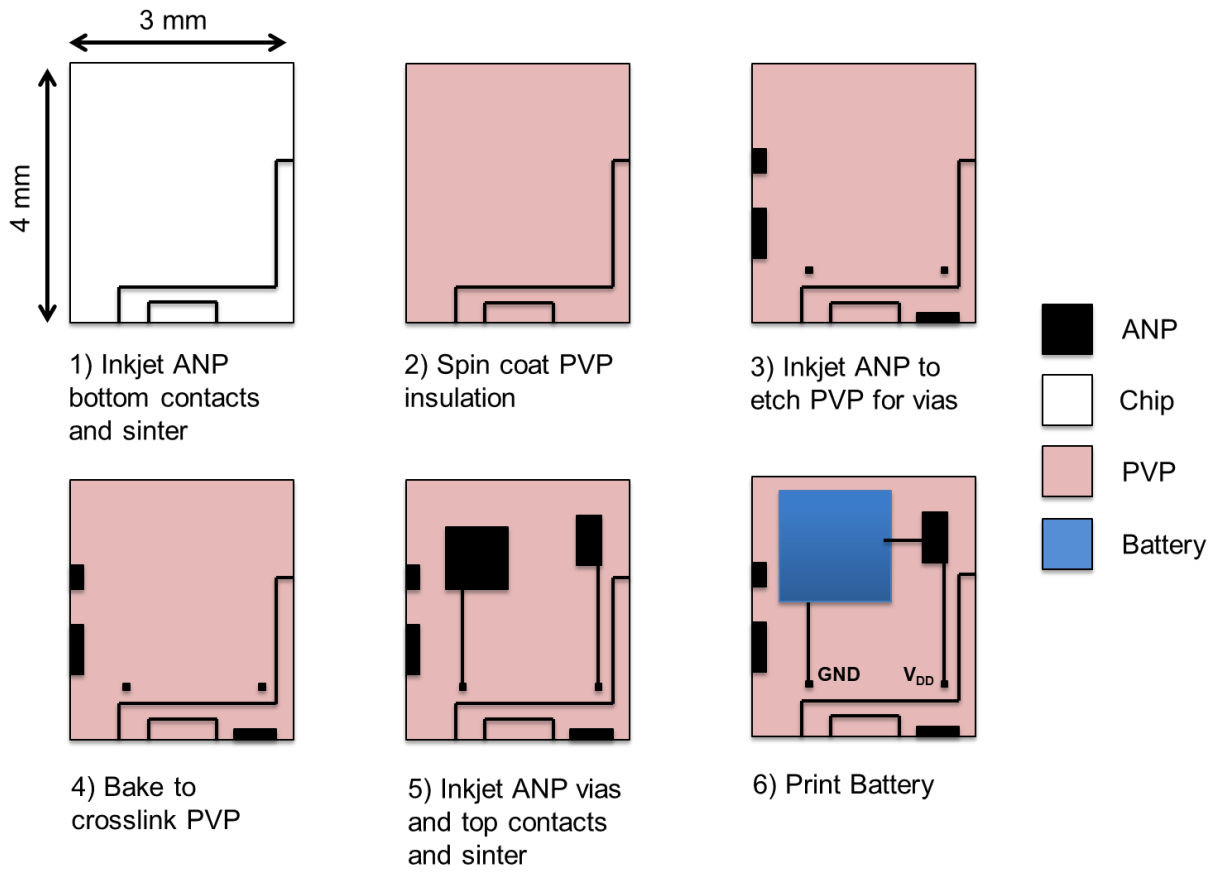


Figure 5.4: Process diagram for inkjet printed package for an integrated device.

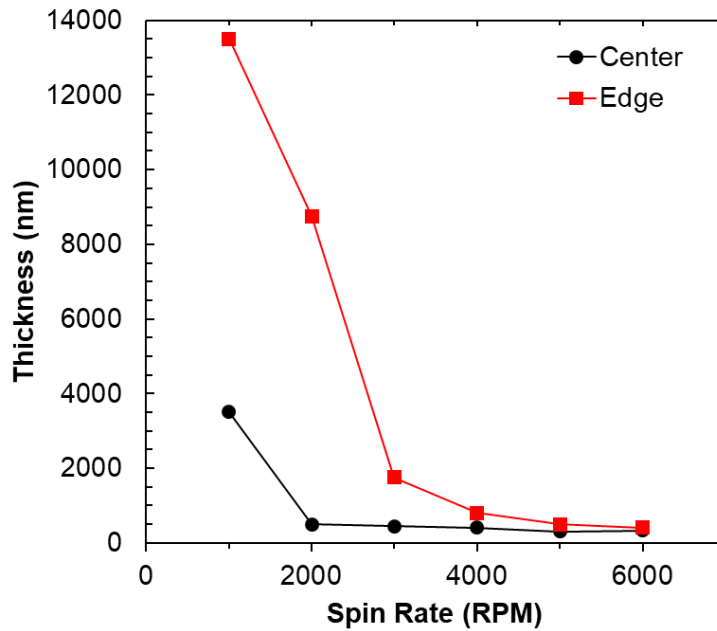


Figure 5.5: Thickness dependence on spin rate for spin coated PVP on a 3 x 4 mm Si substrate, including center and edge PVP thickness.

As detailed in Figure 5.4, Ag bottom contacts were used to connect contacts on the chip for device operation. Without any surface treatment to the chip, Ag linewidths were optimized to achieve a 38 μm linewidth using a 25 μm drop spacing, 14 V applied cartridge potential, and a 60 $^{\circ}\text{C}$ printer platen temperature. This was compatible with our chip design, which had 110 μm diameter Al contacts along the edge of the chip. After spin coating the PVP layer, vias were formed by printing the ANP ink directly on top of the uncrosslinked PVP as the ANP ink solvent etched through the spin-coated PVP layer. In the remaining vias, Ag interconnects were inkjet printed after PVP crosslinking. In future designs, inkjet printed acetone can also be used to define the vias in the PVP layer and may offer lower overall resistance in the interconnect design. Via conductivity was then examined using a four point probe setup and a test configuration illustrated in Figure 5.6. This test configuration matches the procedure shown in Figure 5.4, where PVP is spin coated on top of a Ag bottom contact. Using a 100 μm diameter via size (as defined by the sacrificial ANP print area) and a 200 x 200 μm ANP top contact, an average total resistance of 80 Ω was measured across the testing feature. This corresponds to a via resistivity of about 300 $\Omega\text{-cm}$, which is much higher than the 3D printed package architecture. This high resistivity is likely limited by the ANP etching procedure, which will leave uncured ANP mixed with PVP at the via junctions. Future designs will switch to defining vias through a printed acetone etching step, which should help reduce via resistivity in the inkjet printed design.

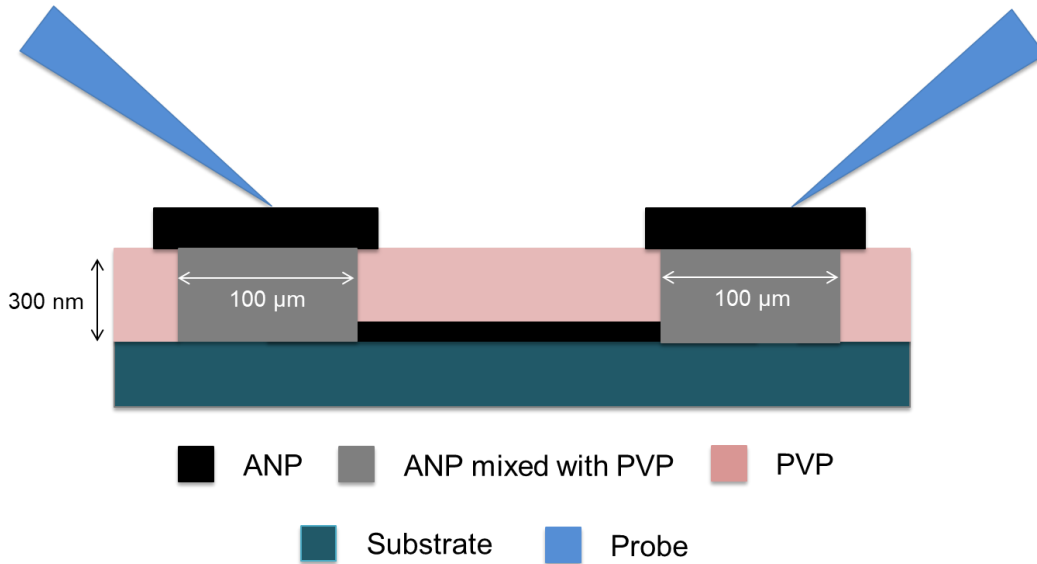


Figure 5.6: Schematic of performance measurement setup for inkjet printed interconnects.

5.3 Integrating Printed Batteries with Energy Harvesting for IoT Device Operation

Packaged energy storage for IoT applications will help enable wireless systems, but printed energy storage must also meet device lifetime requirements and minimum performance thresholds. IoT components are designed at the extreme low-power limits, with peak power consumption on the order of 1 mW and energy consumption less than 1 J per day.^[17] However, on-chip energy storage will be inherently limited since integrated batteries must scale to mm^2 active areas. Figure 5.7 shows the theoretical capacity and lifetime for a Zn- Ag_2O battery, where 1 J of energy stored corresponds to about 0.2 mAh at an operating potential of 1.5 V. At electrode areas approaching 1

mm², a printed Zn-Ag₂O battery could support device functionality for ~10 days for devices with very low sleep state power requirements (~1 μA current draw) and very low sampling rates. While this may suffice for some IoT applications, most will require additional lifetime to maintain device viability.

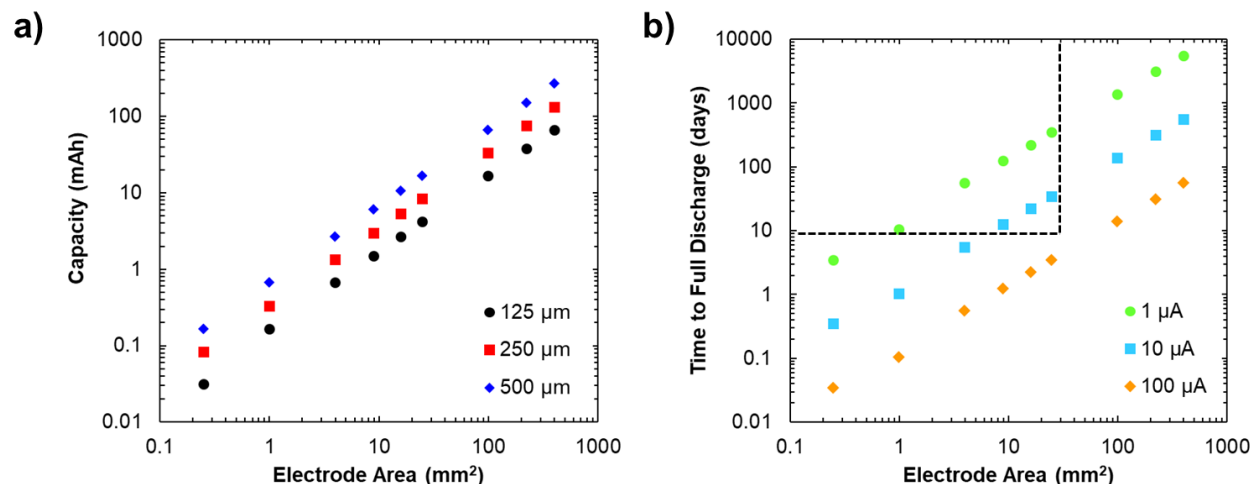


Figure 5.7: a) Theoretical capacity for a printed Zn-Ag₂O battery with different electrode geometries. b) Lifetime for a printed Zn-Ag₂O battery at different average discharge currents (assuming a 250 μm electrode thickness).

Improving device lifetimes can be accomplished by combining energy storage with on-chip energy harvesting as a means to recapture energy from external sources and store it for later use. Various forms of energy can be harvested, but photovoltaics are the most promising route for IoT applications. Compared to other sources such as thermal and piezoelectric harvesting, photovoltaics can be easily integrated at millimeter-scale active areas and provide higher power densities (mW cm⁻² versus μW cm⁻²).^[5,18,19] Previous studies have focused on optimizing photovoltaics, but additional work is needed to examine the performance of tandem energy storage and harvesting systems and the performance limitations of integrated batteries. In this section, we aim to explore the pulse discharge and trickle charge capabilities of a printed Zn-Ag₂O battery in order to demonstrate its efficacy in an integrated IoT system. To our knowledge, this is the first investigation of printed battery performance under realistic IoT conditions; so an explanation of the experimental methodology and testing procedure will first be given to highlight key device criteria.

Stencil printed Zn-Ag₂O batteries were fabricated using the same procedure outlined in Chapter 2. Electrodes were printed using a 2 x 2 mm stencil with a thickness of 125 μm. Pulse discharge and trickle charge conditions were simulated using a BST8-MA potentiostat from MTI Corp and a Bio-Logic BCS-805 battery cycling system. Several conditions were examined under simulated charge/discharge experiments to determine their impact on battery lifetime, including pulse frequency, pulse current, and battery depth of discharge. Each factor is application specific with depth of discharge dependent on the pulse frequency and current. As the sampling rate of the device increases, the battery must be discharged more frequently, which consumes a larger fraction of the available battery capacity.

Figure 5.8 shows the expected relationship between pulse frequency and daily capacity draw for a typical printed Zn-Ag₂O battery with a total capacity of 0.2 mAh. Assuming typical low-power device requirements (one second pulse at currents ranging from 0.25 to 1 mA with a 2 μ A off-state current), sampling intervals of at least one hour require only 4% of the total battery capacity per day and can easily be recaptured through energy harvesting. At high sampling intervals and pulse currents, the other extreme end of device operation, about 35% of the battery capacity is required per day. Thus, we set out to examine a range of pulse discharge conditions that consume between 0 and 35% of the battery capacity.

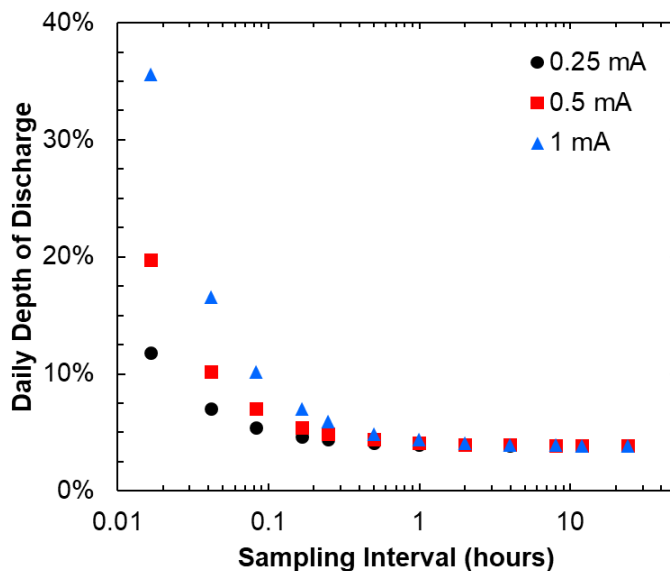


Figure 5.8: Daily capacity draw under pulse discharge conditions for a printed Zn-Ag₂O battery at varying pulse frequencies and currents. Data assumes a 2 μ A off-state current, 1 sec pulse duration, and a 4 mm² electrode area and 125 μ m thickness.

Experiments simulating an IoT system were conducted using a charge/discharge cycling profile controlled by a potentiostat, with the results summarized in Figure 5.9. Intermittent sensing and communication pulses were represented by short periods of constant current discharge and energy harvesting represented by periods of constant current charge. An example of a cycling profile used for one of the printed batteries is included in Figure 5.9c. Large overpotentials during charging were observed in the first few cycles of this cell, but decreased after the sixth cycle. While a few of the other testing conditions also showed a similar initialization phase for the first few cycles, all charge/discharge conditions maintained fairly stable voltaic efficiencies (~90%) throughout cell cycling, as shown in Figure 5.10. Future experiments may benefit from tighter voltage cutoffs to avoid such overcharging in the cells.

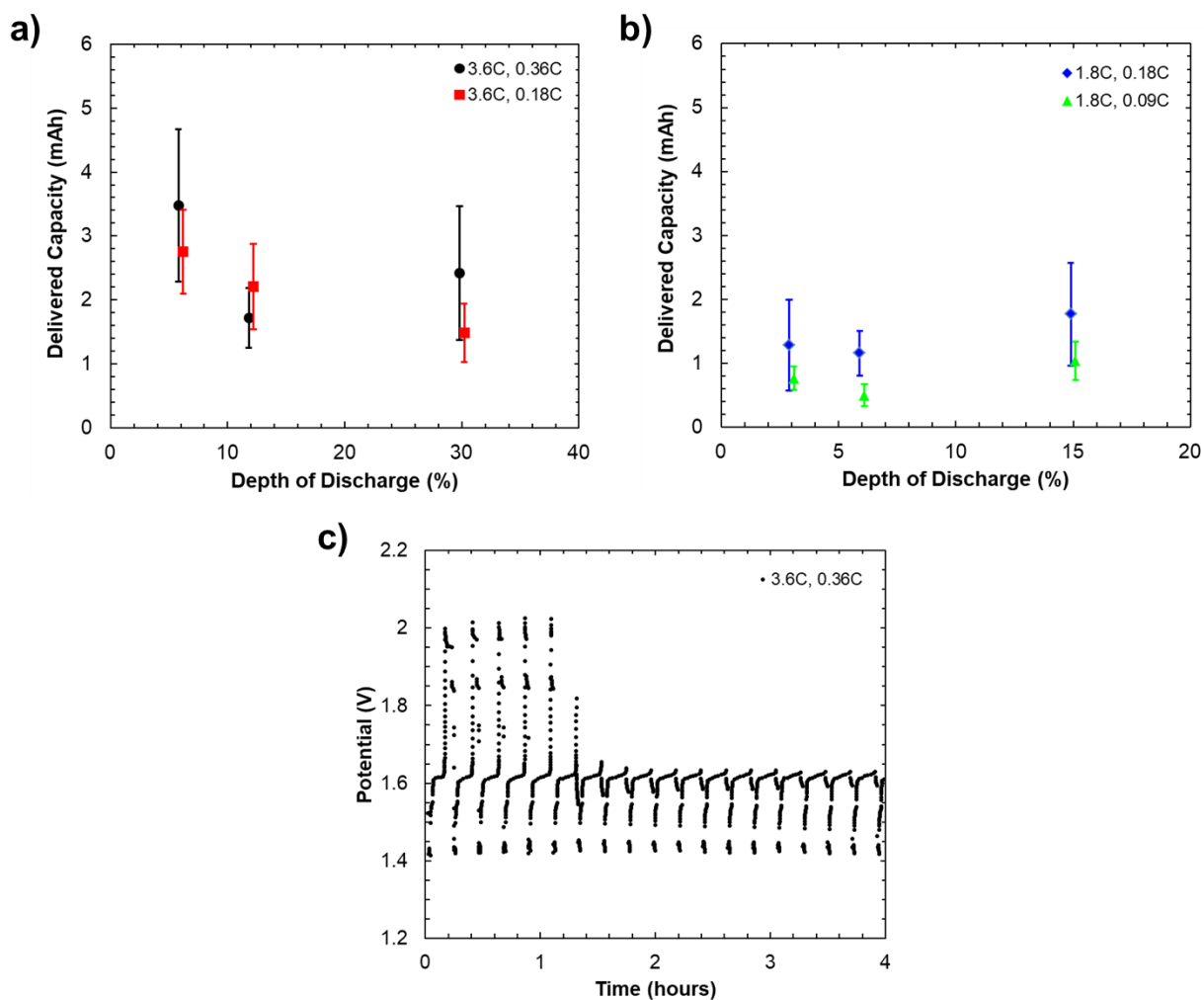


Figure 5.9: Simulated pulse discharge performance for printed Zn-Ag₂O batteries at a) 3.6C and b) 1.8C discharge rates, with c) a sample charge/discharge cycling profile.

In an effort to accelerate the testing procedure, discharge periods were chosen on the order of minutes to increase the total capacity consumption for a single pulse. Tests at two relatively high discharge rates (1.8 C and 3.6 C) were performed at pulse durations of 1, 2, and 5 min to achieve depths of discharge between 0 and 35%. Total capacity for each battery was about 0.2 mAh; so 1.8 C and 3.6 C discharge rates corresponded to 0.36 and 0.72 mA respectively (~0.5 and 1 mW). After each pulse, the printed battery was charged to recover the total capacity used during discharge. To simulate different pulse frequencies, charging rates of 5 and 10% of the discharge rate were used, which corresponds to duty cycles of 4.8 and 9.1% and charging currents of 9, 18, 36, or 72 μ A. These charging currents were selected to match a typical output power range from a CMOS solar cell. High variance in delivered capacity was observed for most of the testing conditions; so additional experiments are needed to elucidate trends related to depth of discharge and pulse characteristics. However, the 3.6C/0.36C condition (Fig 5.9a) had an average delivered capacity of 3.5 mAh, which is nearly 18 times the printed battery capacity on a single discharge (0.2 mAh) and would support device functionality for over a month. This proves that printed millimeter-scale Zn-Ag₂O batteries are certainly viable in IoT system architectures when

combined with energy harvesting, but additional testing and optimization is needed. Particularly, future experiments should expand the parameter space to include shorter pulse durations that match the millisecond to second timescales used in sensing applications.

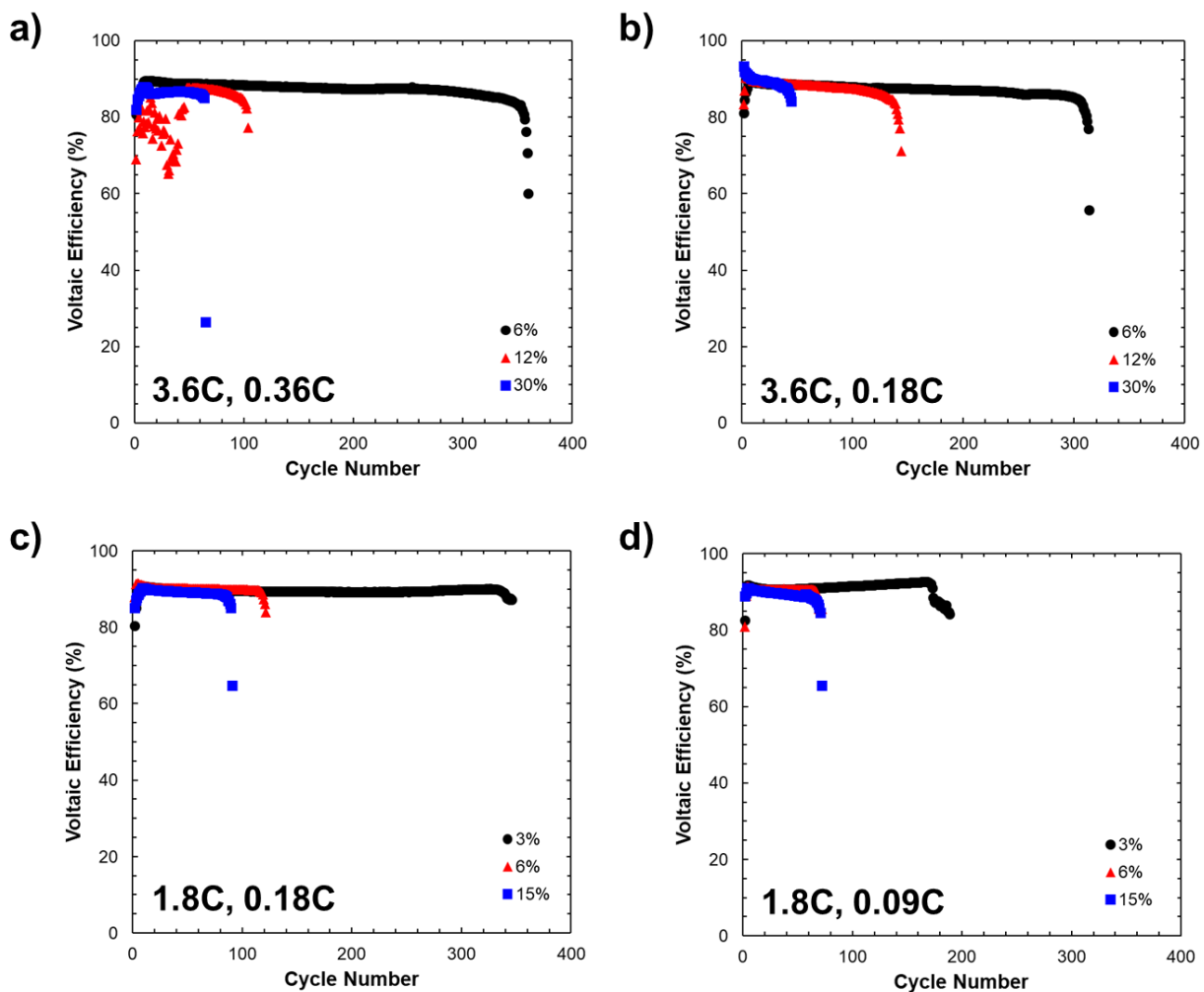


Figure 5.10: Printed cell voltaic efficiency as a function of discharge/charge conditions and the resulting depth of discharge in the printed Zn-Ag₂O battery.

5.4 Screen Printed Zn-Ag₂O Arrays

In addition to IoT device lifetime, integrated energy storage must also support a wide range of performance benchmarks for sensing, computing, and communication functionalities. While IoT drivers are typically geared towards low-power requirements, tailoring energy storage to support higher voltage and power requirements can enhance IoT capabilities. For example, millimeter scale single chip nodes will likely rely on microelectromechanical system (MEMS) components, which typically require relatively high pull-in voltages (5–30 V).^[20] While electrochemical cell potentials cannot meet these demands, battery arrays can provide sufficient energy and power to drive high voltage IoT components. By printing an array of cells, the power supply voltage can be modulated based on the required operation mode by connecting or isolating

cells within the array. Here, we aim to design printed battery arrays for integrated electronic systems and use the printed Zn-Ag₂O battery outlined in Chapter 2 as our cell chemistry to establish proof of concept of the printed array design. Screen printing is chosen to achieve thick electrode films and high-throughput manufacturing of cell arrays. While stencil printed battery arrays have been previously developed, screen printing is a more robust method to rapidly print large arrays of printed batteries. To our knowledge, this is the first demonstration of screen printed battery arrays; so we will first highlight the materials and processing requirements to achieve screen printable battery inks.

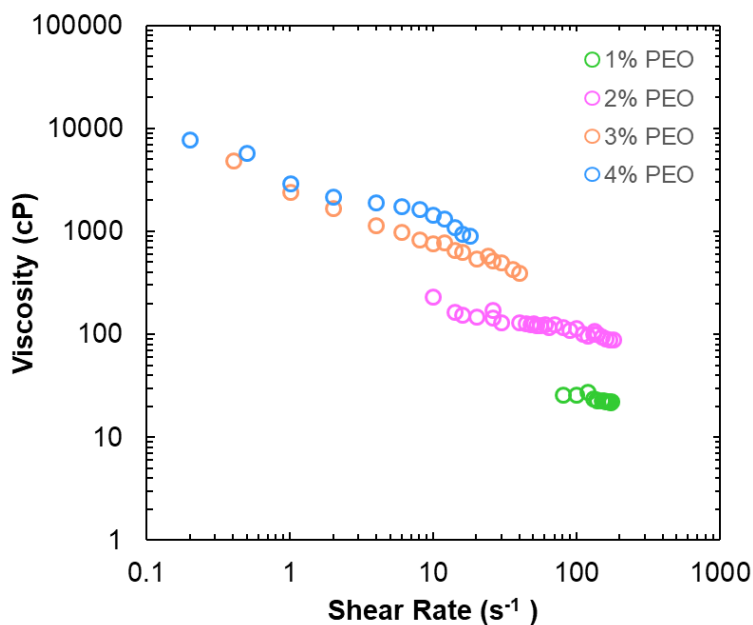


Figure 5.11: Viscosity tuning via polymer binder mass loading.

An industrial-grade screen printer (ASYS, ASP 01M) was used to deposit screen printed Zn-Ag₂O batteries. Compared to stencil printing, electrode inks must be less viscous to ensure suitable ink transfer onto the substrate. At higher viscosities, inks tend to clog the mesh and impede ink deposition, resulting in printing defects and thinner films that can impact battery capacity. To optimize the Zn and Ag₂O electrode formulations for screen printing, binder and active particle mass loading were closely examined. Figure 5.11 shows the dependence of polyethylene oxide (PEO) mass loading on ink viscosity. As expected, lowering the binder content in electrode inks leads to lower viscosities and improved ink transfer through the mesh. While stencil printed batteries used a 5 wt% PEO binder, 4 wt% PEO was found to be suitable for ink transfer via screen printing and was used for all subsequent experiments. Additionally, Ag₂O mass loading was found to impact electrode thickness, as shown in Figure 5.12. Using a 96 wt% Ag₂O ink, printed films achieved thicknesses near 50 μm on a single print and showed fewer pinholes and print defects compared to lower mass loadings. Similar tests were performed for the Zn electrodes, with a 99 wt% active component mass loading found to be optimal. Similar thickness for Zn electrodes were observed on both plastic and glass substrates, as shown in Figure 5.13, with a single pass also resulting in printed film thicknesses of about 50 μm.

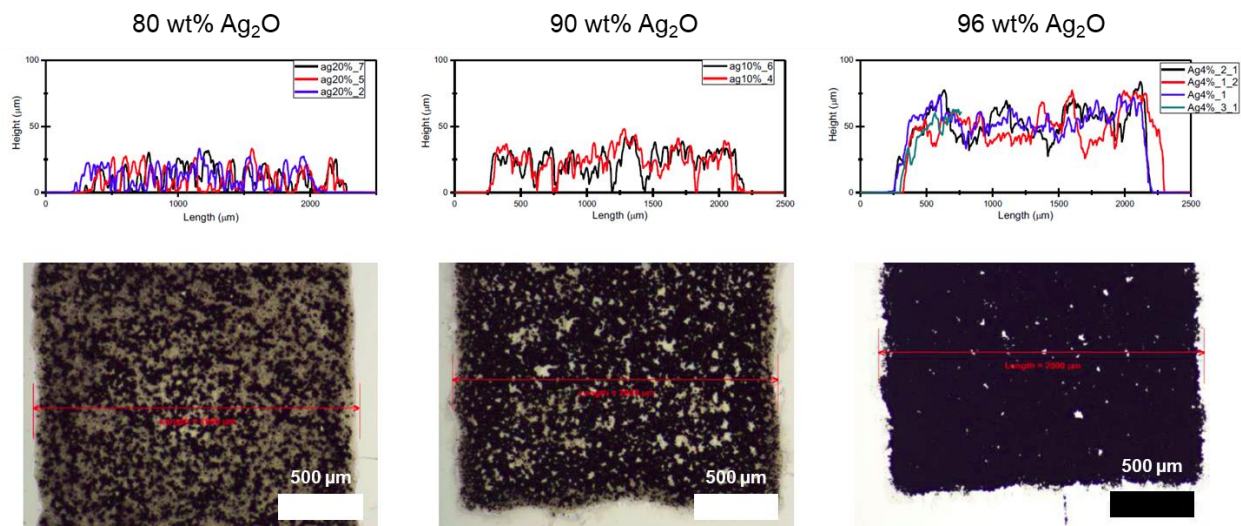


Figure 5.12: Screen printed Ag_2O electrode thickness tuning via active particle mass loading.

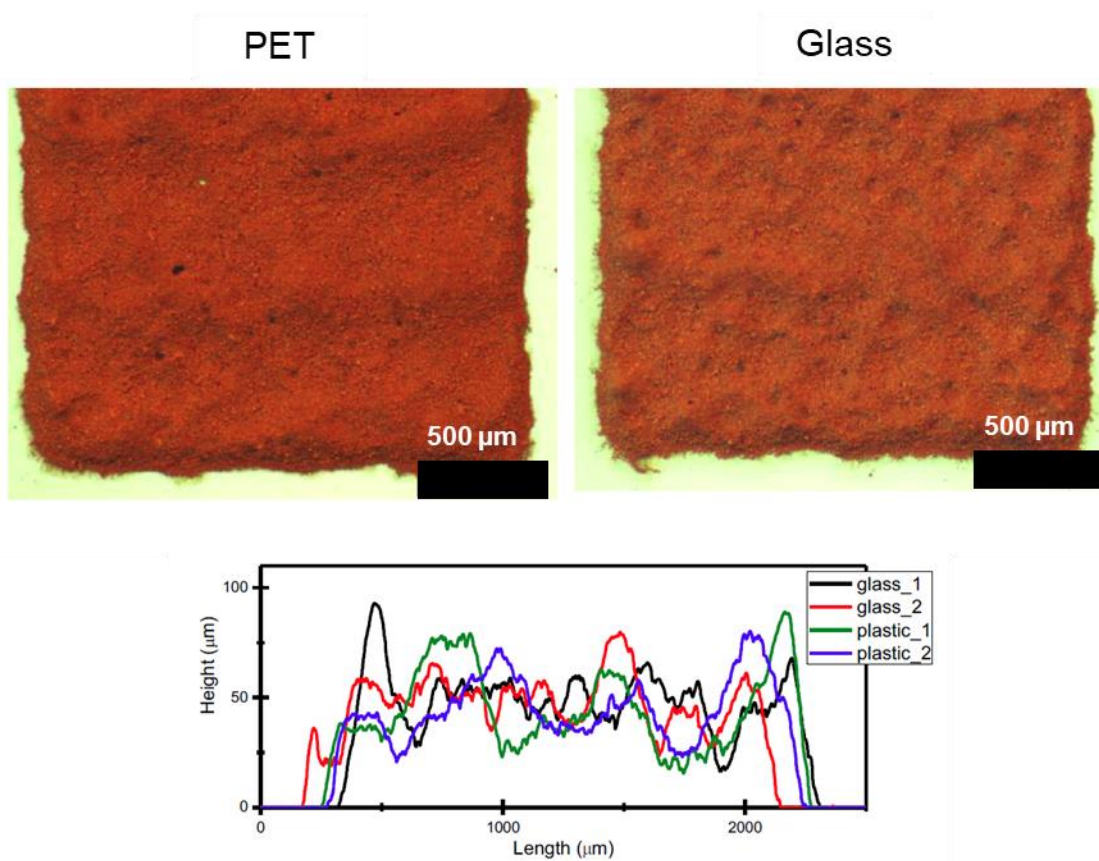


Figure 5.13: Screen printed Zn electrode thickness characterization.

Additionally, print uniformity was tested in a 4 x 4 cell array to ensure consistent electrode deposition within the cell array. Figure 5.14 illustrates this data for both printed Zn and printed

Ag₂O electrodes. Arrays printed on glass were measured using a Dektak stylus profilometer. Electrode thickness was shown to be independent of print direction and fairly uniform within the array, with an average thickness measured between 45 and 50 μm for each electrode position.

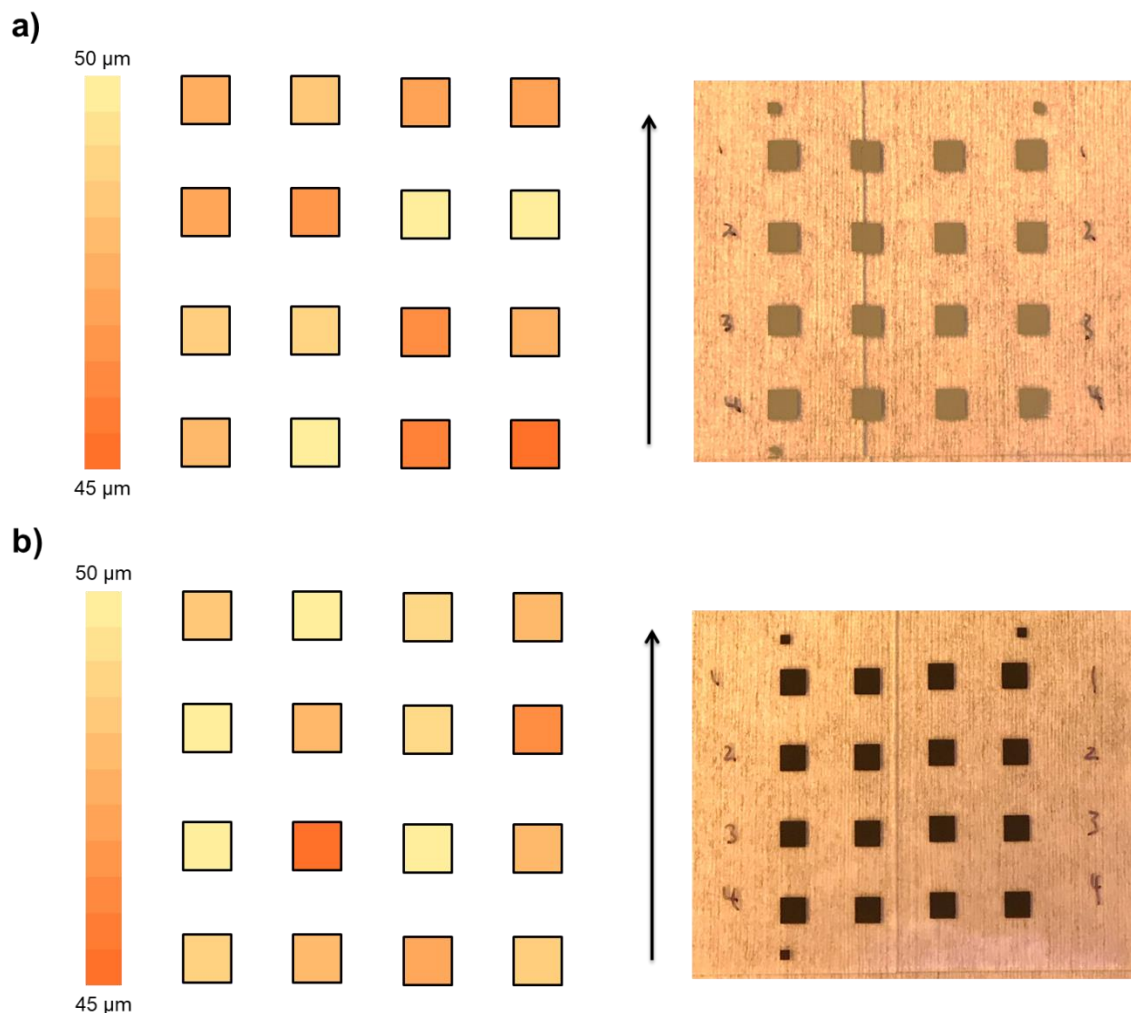


Figure 5.14: Thickness uniformity for printed arrays of a) Zn and b) Ag₂O electrodes. All electrodes are 5mm and arrow indicated printing direction.

Finally, screen printed battery performance was demonstrated through initial tests highlighted in Figures 5.15 and 5.16. Screen printed silver current collectors (Creative Materials #120-07) were used for both the anode and cathode and a sol-gel separator was stencil printed as described in Chapter 2. Single cells were first evaluated at both 25 and 4 mm² electrode areas, with screen printed cells achieving areal capacities of about 1.2 mAh cm⁻². Areal capacities were expected to be lower for the screen printed cells compared to the optimized stencil printed cells shown in Chapter 2 due to their lower electrode thickness. Further studies should focus on multi-step printing of Ag₂O electrodes in order to increase screen printed battery capacities. Polarization data in Figure 5.15c shows that screen printed cells match the power density performance of stencil printed cells from Chapter 2 with cells maintaining an operating potential over 1.4 V at current

densities up to 12 mA cm^{-2} . A maximum power density of 17 mW cm^{-2} is shown here, which matches our previous results for stencil printed cells. After screen printed cell performance was established, a 2×1 screen printed array was demonstrated, as shown in Figure 5.16. Using printed Ag interconnects between cells, operating voltages were shown to scale to about 2.9 V at current densities up to 12 mA cm^{-2} . Power densities also scaled accordingly, with a maximum value of about 34 mW cm^{-2} observed at 12 mA cm^{-2} . Current research efforts are focused on demonstrating larger battery arrays for higher voltage applications, specifically targeting an 8 cell array that could provide up to 12 V for emerging IoT devices. Challenges related to printed interconnect design and printed battery yield must be further investigated in order to achieve high voltage arrays.

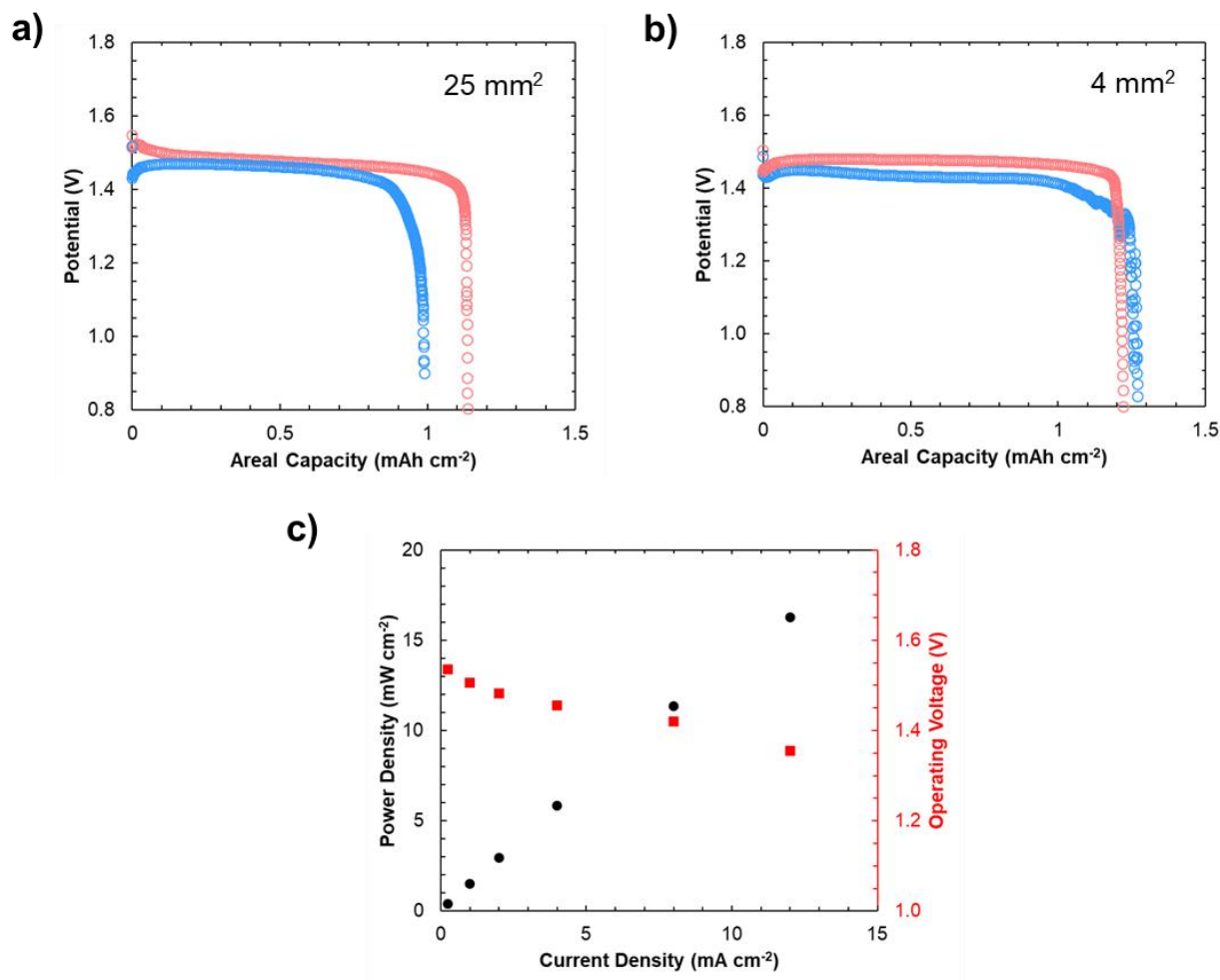


Figure 5.15: Screen printed Zn-Ag₂O battery performance for a single cell, including discharge characteristics at 2 mA cm^{-2} for a) 25 mm^2 and b) 4 mm^2 electrode areas and c) polarization data up to 12 mA cm^{-2} .

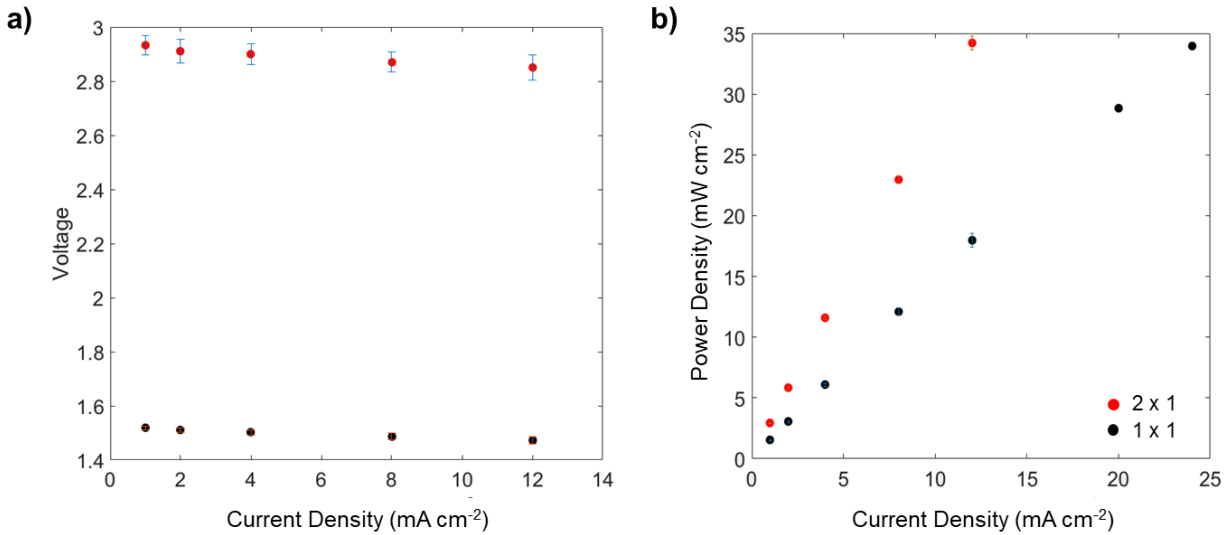


Figure 5.16: Screen printed battery performance for Zn-Ag₂O arrays, including a) voltage and b) power density characteristics. All cells 25 mm².

5.5 Summary

In summary, this chapter explored system-level integration of printed batteries for IoT applications. Using 3D and inkjet printing, millimeter-scale packaging and interconnect designs were demonstrated. Our 3D-printed design achieved low via resistivity with a fully integrated packaging strategy, but via feature resolution was limited, with a minimum via diameter of 189 μm observed. In contrast, our inkjet-printed design featured via sizes as low as 40 μm , but was more limited in via resistivity. Additionally, printed Zn-Ag₂O batteries were tested under realistic IoT device conditions with simulated recharge from energy harvesting. With pulses up to 1 mW, printed batteries were tested up to 35% depth of discharge and showed total capacities between 1 and 3.5 mAh (5–17.5 J), or up to 18 times the original battery capacity. This demonstrates that a millimeter-scale printed battery is capable of powering IoT devices under pulsed sensing and communication conditions. Finally, screen printed Zn-Ag₂O battery arrays were designed, achieving 50 μm thick electrodes on a single pass. This translated to battery capacities of about 1.2 mAh cm⁻² per cell and a maximum power density of 17 mW cm⁻². Initial tests of 2 cell arrays showed ideal voltage and power scaling, with operating potentials near 3 V and a maximum power density of 34 mW cm⁻². Overall, this work highlights many system-level challenges related to powering wireless sensor networks and should provide an outline for future investigation of packaging and integration of printed millimeter-scale energy storage.

5.6 References

- [1] B. Warneke, M. Last, B. Liebowitz, K. S. J. Pister, *Computer (Long Beach, Calif)*. **2001**, 34, 44.
- [2] J. M. Kahn, R. H. Katz, K. S. J. Pister, *J. Commun. Networks* **2000**, 2, 188.
- [3] M. D. Scott, B. E. Boser, K. S. J. Pister, *IEEE J. Solid-State Circuits* **2003**, 38, 1123.
- [4] B. W. Cook, S. Lanzisera, K. S. J. Pister, *Proc. IEEE* **2006**, 94, 1177.
- [5] A. Raj, D. Steingart, *J. Electrochem. Soc.* **2018**, 165, B3130.
- [6] D. Steingart, in *Energy Harvest. Technol.*, **2009**, pp. 267–286.
- [7] D. Steingart, S. Roundy, P. K. Wright, J. W. Evans, *MRS Bull.* **2008**, 33, 408.
- [8] M. R. Lukatskaya, B. Dunn, Y. Gogotsi, *Nat. Commun.* **2016**, 7, 1.
- [9] J. Perelaer, P. J. Smith, D. Mager, D. Soltman, S. K. Volkman, V. Subramanian, J. G. Korvink, U. S. Schubert, *J. Mater. Chem.* **2010**, 20, 8446.
- [10] B. E. Kahn, *Proc. IEEE* **2015**, 103, 497.
- [11] H. C. Nallan, J. A. Sadie, R. Kitsomboonloha, S. K. Volkman, V. Subramanian, *Langmuir* **2014**, 30, 13470.
- [12] J. A. Sadie, V. Subramanian, *Adv. Funct. Mater.* **2014**, 24, 6834.
- [13] S. Chung, M. Ul Karim, M. Spencer, H. Kwon, C. P. Grigoropoulos, E. Alon, V. Subramanian, *Appl. Phys. Lett.* **2014**, 105, 261901.
- [14] S. Chung, M. Ul Karim, H. Kwon, V. Subramanian, *Nano Lett.* **2015**, 15, 3261.
- [15] M. Ul Karim, S. Chung, E. Alon, V. Subramanian, *Adv. Electron. Mater.* **2016**, 1.
- [16] S. Chung, M. Ul Karim, H. Kwon, W. Scheideler, V. Subramanian, *J. Microelectromechanical Syst.* **2017**, 26, 95.
- [17] J. Carballo, W. Chan, A. B. Kahng, M. Kakimoto, S. Nath, T. Saito, K. Seto, G. Smith, I. Yamamoto, in *Int. Technol. Roadmap Semicond. 2.0*, **2015**.
- [18] S. Kim, R. Vyas, J. Bito, K. Niotaki, A. Collado, A. Georgiadis, M. M. Tentzeris, *Proc. IEEE* **2014**, 102, DOI 10.1109/JPROC.2014.2357031.
- [19] S. Roundy, D. Steingart, L. Frechette, P. Wright, J. Rabaey, in *Wirel. Sens. Networks*, **2004**, pp. 1–17.
- [20] A. M. Gaikwad, D. A. Steingart, T. N. Ng, D. E. Schwartz, G. L. Whiting, *Appl. Phys. Lett.* **2013**, 102, 233302.

Chapter 6: Conclusions and Future Work

6.1 Summary of Contributions

Broad distribution of wireless electronic devices hinges on the development of integrated energy storage. This dissertation addresses several challenges associated with energy storage scalability and integration and realizes millimeter-scale printed batteries that meet IoT performance requirements. Guidelines related to printed battery processing, structure, properties, performance, and characterization are included and serve as a roadmap for future research on integrated energy storage, regardless of battery chemistry or device architecture. Methods and materials for printed Zn-Ag₂O and Zn-air batteries are presented in Chapters 2 and 3, implementing vertical cell designs to minimize battery footprints through careful consideration of materials and processing compatibility. As a result, this work establishes new performance benchmarks for printed batteries, achieving areal capacities above 10 mAh cm⁻² and power densities well above 10 mW cm⁻² at millimeter-scale areas.

New approaches to defining printed battery performance are also explored in Chapter 3, which highlight the dependence of battery performance on electrode materials design. *Operando* pressure decay and differential electrochemical mass spectrometry (DEMS) measurements enable direct observation of oxygen reduction efficiency in printed Zn-air batteries. By pairing *operando* experiments with ex-situ physical and chemical analysis, interactions between electrode ink components are investigated and guide the fabrication of low temperature processed metal-air cathodes (< 200 °C). This comprehensive approach is broadly applicable to future work on application driven electrode design, both for printed and non-printed battery architectures. Additionally, this work may be influential in the future development of other aqueous metal-air chemistries, where oxygen reduction performance is also a limiting factor.

Furthermore, battery degradation and failure mechanisms and their impact on battery performance and integration are investigated throughout this dissertation, culminating with a broad discussion of Zn corrosion in alkaline electrolytes in Chapter 4. *Operando* characterization techniques are utilized to directly observe corrosion reactions at the anode-electrolyte interface in the printed Zn-air battery. Overall, this methodology aims to improve the design of corrosion resistant anode materials and increase the viability of printed batteries for integrated electronic applications. First, pressure decay and DEMS analysis are used to rapidly screen materials parameters and operating conditions to identify significant factors that influence anodic corrosion. Second, *operando* X-ray diffraction (XRD) is incorporated to verify the significance of these factors by examining the formation and evolution of solid corrosion products at the anode-electrolyte interface. Here, anode current collector material, electrolyte concentration, and Zn particle size are shown to predominantly impact anodic corrosion. However, this approach is transferable to other battery chemistries and may be particularly useful for other aqueous battery systems in order to mitigate anodic corrosion and improve battery lifetime.

Finally, Chapter 5 summarizes system level integration strategies for printed Zn batteries and IoT devices. Proof of concept packaging and interconnect designs are demonstrated using printing techniques for millimeter-scale and commercially available sensor nodes. Advantages and limitations of 3D printed versus inkjet printed architectures are discussed with regards to feature resolution and via resistivity. Moreover, printed Zn-Ag₂O batteries are simulated under realistic IoT operation modes to examine battery performance in an integrated system with energy

harvesting. Pulse discharge and trickle charge testing suggest that printed Zn-Ag₂O batteries are viable in real IoT systems, sustaining device performance for hundreds of cycles at modest depth of discharge (0 – 35%). Printed Zn-Ag₂O battery arrays are also demonstrated using screen printing to support high voltage device applications, with initial tests showing potential and power scaling in series arrays.

6.2 Recommendations for Future Work

Further development of integrated energy storage will accelerate the realization of ubiquitous electronics for IoT networks. While several issues must be addressed in order to implement millimeter-scale energy storage, battery design first requires an *application driven approach and appreciation for all imposed requirements*. For example, a wireless electronic device will always dictate the power and energy requirements for energy storage. Specifically, a battery must be smaller than the other system components to match device scaling and must use low-cost materials to ensure the entire system is affordable. At the same time, this battery must support high discharge currents and power requirements, have a high capacity to sustain a long system lifetime, use materials and packaging compatible with system level processing, and maintain suitable performance without significant degradation. No current battery chemistry can support all of these requirements, a subtle point that electronics engineers should recognize when developing integrated devices. However, electrochemical engineers must conduct energy research in service of these goals and realize that all of these requirements must be simultaneously attained. Radical technological changes require interdisciplinary efforts, so future work must prioritize co-design of electronic and electrochemical components.

Among the challenges facing millimeter-scale energy storage, battery stability and degradation remains paramount. Battery lifetime is the limiting factor in nearly all electronics applications and battery or device replacement will be extremely difficult for densely deployed device networks. Extending battery lifetime and performance relies on the investigation of *electrode-electrolyte interfaces*. In nearly all electrochemical reactions, surfaces dictate the transfer of charge and ionic species and local changes in chemical and morphological states can have a huge impact on battery state of health. However, electrode-electrolyte interfaces are still poorly understood in nearly all battery chemistries and require further investigation. The most prominent exception are Li-ion batteries, where significant advances have been made to understand how interfacial changes impact battery stability and performance. For example, dendrite growth and solid-electrolyte interphase formation have been studied thanks in part to novel characterization techniques including *operando* methods.

Moving forward, *operando* techniques must also be applied to alternative cell chemistries in order to study limiting degradation processes and guide future materials development. Although they are unlikely to replace Li-ion, aqueous battery chemistries such as Zn, Mg, and Al offer several advantages for emerging electronics applications. This includes critical factors such as materials handling and packaging, availability and cost of materials, and safety and toxicity concerns, indicating they should be further explored to complement Li-ion batteries in electronic applications. As shown in this dissertation, aqueous batteries are promising for millimeter-scale energy storage, but also will be influential in other applications including energy storage for wearable and implantable devices or for larger platforms such as renewable energy generation. However, issues related to cycle life, corrosion, low capacity, and charge retention must first be

resolved in order for these batteries to be viable for broader electronics applications. *Operando* characterization can help identify how physical and chemical changes to aqueous battery interfaces influence these performance benchmarks and may enable broader implementation of emerging cell chemistries. For example, aqueous flow batteries offer significant promise towards eliminating electrode passivation due to corrosion. Since the electrode and electrolyte are mixed together and constantly cycled via pumps, the electrode-electrolyte interface remains in a dynamic state throughout battery operation. Here, *operando* characterization techniques could be particularly useful towards identifying the evolution of the reaction surface and monitoring how charge and ion transfer are affected by materials design and processing parameters.